RATIONAL SYNTHESIS OF NOVEL REFORMING CATALYSTS

A Dissertation
Presented to
The Academic Faculty

by

Jessica L. Ewbank

In Partial Fulfillment
of the Requirements for the Degree
Doctor in Philosophy in the
School of Chemical Engineering

Georgia Institute of Technology
May 2015

RATIONAL SYNTHESIS OF NOVEL REFORMING CATALYSTS

Approved by:

Dr. Carsten Sievers, Advisor
School of Chemical Engineering & Biomolecular Engineering
Georgia Institute of Technology

Dr. Yulin Deng
School of Chemical Engineering & Biomolecular Engineering
Georgia Institute of Technology

Dr. Christopher Jones
School of Chemical & Biomolecular Engineering
Georgia Institute of Technology

Dr. Preet Singh
School of Materials Science and Engineering
Georgia Institute of Technology

Dr. Pradeep Agrawal
School of Chemical Engineering & Biomolecular Engineering
Georgia Institute of Technology

Date Approved: December 01, 2014

To my husband, Michael and our fur baby, Powder. None of this would have been possible without you two.

ACKNOWLEDGEMENTS

I would like to thank my advisor, Dr. Carsten Sievers, for accepting me into his research group and for providing me with the resources I needed to learn and grow in graduate school. Your advice, patience, and fostering of independent research are truly appreciated. You have also afforded me many opportunities to conduct research with many external collaborators throughout my time in graduate school which provides me with a great platform for the next phase of my career. I would like to thank my thesis committee, Dr. Pradeep Agrawal, Dr. Christopher Jones, Dr. Yulin Deng, and Dr. Preet Singh for their support, guidance, and encouragement. Thank you to Billy Bardin, Brien Stears, Derrick Flick, Mark Siddoway, John Hennely, and Mark Stewart from The Dow Chemical Company for providing technical input on my project and affording me the opportunity to conduct a very fruitful internship during graduate school. Financial support and project guidance from the Renewable Bioproducts Institute and the Dow Chemical Company is gratefully acknowledged.

I would like to thank Sievers' group members, especially, John Copeland, Adam Van Pelt, Sarah Schimming, Guo Shiou Foo, and Gautami Newalker. John and Adam provided guidance and support that was critical to my progression as a researcher. I feel extremely fortunate to have had the opportunity to work with such brilliant researchers and I am a better researcher (and person) for having known you both. Thanks to Sarah Schimming for taking on the task of learning how to build equipment alongside me in the lab. Because of you, I am not afraid to open up any piece of equipment and tinker.

Thank you to Sudhir Sharma and Michael Mangarella of the Georgia Tech Chemical Engineering department for always offering research assistance and outside perspectives.

Thank you to Dr. Jeff Miller at Argonne National Lab, who helped me to refine my XAS skills. Your patience and persistence helped to accomplish one of my ultimate goals in graduate school.

I would like to thank those who make the research progress behind the scenes: Leslie Schlag for helping me process countless expense and travel reports; Kevin Guger, Bradley Donovan, Samuel Skinner, and Charles Brookshire in the IT department for setting up and fixing multiple computers for me; Don Woodyard in the Chemistry and Biochemisty glass shop for helping me fabricate reactor tubes; Richard Bedell in the Chemistry and Biochemisty electrical shop for helping me fix furnaces; Jerry Nunn for helping me find the root cause of many lab issues; and Hank (Major) White for always checking in on me during late nights in the lab.

I would especially like to thank Dr. Don Soash from Hillsborough Community College. Prior to enrolling in your college algebra class, I had not stepped foot in a classroom in 4 years. If I had not had such a positive experience in my core math classes, I am certain I would not be an engineer today. Your passion, dedication, and enthusiasm in your teaching made me a confident student and prompted me to take my education to this level. You have impacted my life more than you can ever know, thank you.

To my parents-in-law, Betty & Michael Neimi, thank you for your support at every step through this journey. To my brother-in-law Mark Rogers, thank you for friendship, I miss you every day and wish you were here to be a part of the next chapter of our lives. To my aunt, Cindy Hudson, thank you for all of your kind words of encouragement throughout

my pursuit of education. Finally, to my extended family; Josh, Jami, and Gavin Moody; Bradley and Mandy Mills; and Briana Pogal-Tobin you can never know how much you've helped me through this process, thank you all for always being there, I love you all.

TABLE OF CONTENTS

LIST OF TABLES

LIST OF FIGURES

LIST OF SYMBOLS AND ABBREVIATIONS

TPR	Temperature Programmed Reduction
TPO	Temperature Programmed Oxidation
XRD	X-ray Diffraction
XAS	X-ray Absorption Spectroscopy
XPS	X-ray Photoelectron Spectroscopy
MS	Mass Spectrometry
BET	Brunauerer-Emmett-Teller
TEM	Transmission Electron Microscopy
HR-TEM	High Resolution Transmission Electron Microscopy
ICP	Inductively Coupled Plasma
GC	Gas Chromatograph
FID	Flame Ionization Detector
TCD	Thermal Conductivity Detector
SEA	Strong Electrostatic Adsorption
CA	Controlled Adsorption
DI	Dry Impregnation
PZC	Point of Zero Charge

SUMMARY

The majority of the world's fuels and chemicals come from resources such as coal, oil, and natural gas and their availability is finite. Gasification of alternative carbon sources, such as biomass, offers the potential to produce cost advantaged, carbon neutral, renewable fuels and chemicals. [1] However, biomass derived syngas contains a variety of wastes and contaminants that must be reformed so that of syngas of suitable composition can be further utilized in the production of chemicals and fuels. Methane and carbon dioxide are two such wastes that must be removed or converted prior to downstream utilization of biogas. Methane steam reforming offers the potential to convert methane and methane dry reforming offers the potential to convert both methane and carbon dioxide contained in biomass derived syngas into more useful syngas. Currently, methane steam reforming is the most common way to commercially produce syngas. Production of syngas by methane dry reforming is also attracting much attention due to the effective utilization of the greenhouse gases methane and carbon dioxide and syngas production with hydrogen to carbon monoxide ratio near one.[2, 3] Catalytic reforming is a promising technology for the abatement of wastes and contaminants in biomass derived syngas.

Nickel and cobalt catalysts with γ-Al_2O_3 supports have been shown to be effective for reforming reactions necessary to produce a syngas of suitable quality for downstream processing. [4] Impregnation methods are the primary synthesis technique for catalysts used for reforming reactions. However, impregnation methods often lead to poor metal dispersion and are un-reproducible from batch to batch. In an effort to prepare

reproducible catalysts and promote the use of a simple, rational synthesis method, a controlled synthesis technique, controlled adsorption (CA), was used and compared against catalysts that have been prepared by a more traditional method, dry impregnation (DI). A systematic synthesis study was conducted to apply CA to Ni/Al_2O_3 and Co/Al_2O_3 catalysts. Point of zero charge (PZC) measurements, pH-precipitation studies, and adsorption isotherms were used in tandem to find optimal synthesis conditions for strong electrostatic adsorption of nickel or cobalt on γ-Al_2O_3. In CA, the pH of the impregnating solution is selected such that metal precursor – support interactions are maximized. At a pH above the PZC, the surface is deprotonated and cations can be adsorbed. Thus, supports with "high" PZC (such as γ-Al_2O_3) introduce special challenges for the adsorption of cationic complexes. $Ni(NO_3)_2$ and $Co(NO_3)_2$ precursors have low solubility at alkaline pH. Therefore, precipitation of catalyst precursors was investigated and considered. Adsorption isotherms were obtained to identify the pH where maximum uptake of the precursor on to the support occurred and also allowed for identification of the adsorption phenomena associated with Ni/Al_2O_3 and Co/Al_2O_3 systems.

In Chapter 2, adsorption of Co^{2+} on γ-Al_2O_3 under alkaline conditions was found to be severely limited due to bulk precipitation of the cobalt complex. Thus, to control the adsorption of the metal precursor, it was necessary to monitor cobalt deposition as a function of time at a constant pH. Due to the significant deposition of the complex near the PZC of the support, it was found that primarily chemical interactions were involved in the adsorption process. It has been inferred from adsorption isotherms that cobalt specifically adsorbed on the alumina surface, primarily through metal Co^{2+} dimerization and subsequent H_2O ligand exchange with surface oxygen atoms. Physiochemical

characterization methods clearly demonstrated the effect of preparation on the types of active sites formed on the catalyst surface. Methane dry reforming reactions were used to probe the effect of preparation on reactivity. It was found that catalysts prepared by controlled adsorption preformed better than their dry impregnation counterparts. Further, the types of carbonaceous deposits formed on the catalyst surface during reactivity studies were found to be a strong function of preparation method.

In Chapter 3, nickel catalysts prepared by CA and DI were investigated for methane dry reforming reactivity. Ni^{2+} deposition on γ-Al_2O_3 by controlled adsorption was found to proceed by both electrostatic and chemical interactions, which were indicated by non-negligible deposition of the metal complex that occurred at or below the PZC of the support. Thus, a model that described adsorption using only electrostatic terms was not appropriate.[3] Physiochemical characterization methods highlighted the significant differences between nickel catalysts prepared by CA and DI. Environmental TEM imaging clearly distinguished the effects of synthesis and reduction on nickel speciation. A high level of insight was gained to the types of nickel species that exist on low weight loading nickel alumina catalysts that has been a topic widely investigated since the 1950s. Reactivity studies clearly demonstrated that the nature of active sites drastically affects activity and selectivity for methane dry reforming reactivity.

The goal in Chapters 2 and 3 was two-fold: to promote the use of rational catalyst synthesis and study reforming reactions with well-defined surfaces. Use of catalysts with uniform, well-defined structures aided in understanding of major catalyst deactivation modes that result from the harsh conditions associated with reforming reactions. Using

the obtained knowledge, the next generation of materials studied for reforming reactions was a bulk material known as nickel aluminate.

In Chapter 4, nickel aluminates of three nickel-aluminum-oxygen compositions were prepared by the Pechini synthesis: Stoichiometric ($NiAl_2O_4$), Nickel Excess ($NiAlO_{2.5}$), Nickel Deficient ($NiAl_4O_7$). $NiAl_4O_7$, $NiAl_2O_4$, and $NiAlO_{2.5}$ were characterized by temperature programmed reduction (TPR), temperature programmed oxidation (TPO), H_2 chemisorption, X-ray diffraction (XRD), ammonia TPD (NH_3 TPD), N_2 physisorption, and X-ray absorption spectroscopy (XAS). The samples were active for methane steam reforming and methane dry reforming with and without conventional catalyst pre-treatment, e.g. reduction. Nickel aluminates were found to have stable conversion and low carbonaceous deposits making them promising candidates for commercial application in methane reforming reactions. Activity, selectivity, and stability for the methane steam reforming and methane dry reforming was found to be a due to different types of active sites present in the nickel aluminates which was dependent on the pretreatment step, i.e. reduction.

CHAPTER 1

INTRODUCTION

1.1 Catalytic Conditioning of Biogas Derived from Biomass Gasification for Production of Fuels and Chemicals

Biomass gasification is a way to provide a renewable, carbon neutral source of syngas which can be used to produce fuels and chemicals. Figure 1.1 shows the various uses of pure syngas (H_2 + CO) in the chemical industry and the H_2/CO ratio required for each application. [5] However, gasification of biomass results in a syngas that not only contains carbon monoxide and hydrogen but also contaminants such as carbon dioxide, methane, tars (condensable aromatics), inorganic species (mainly Si, Al, Ti, Fe, Ca, Mg, Na, K, P, S, and Cl), sulfur, and ammonia. The presence of high quantities of methane and carbon dioxide in syngas that results from biomass gasification limits applications of biogas for fuel, chemicals, and energy production because of the problems they cause in further syngas upgrading. [6-10]

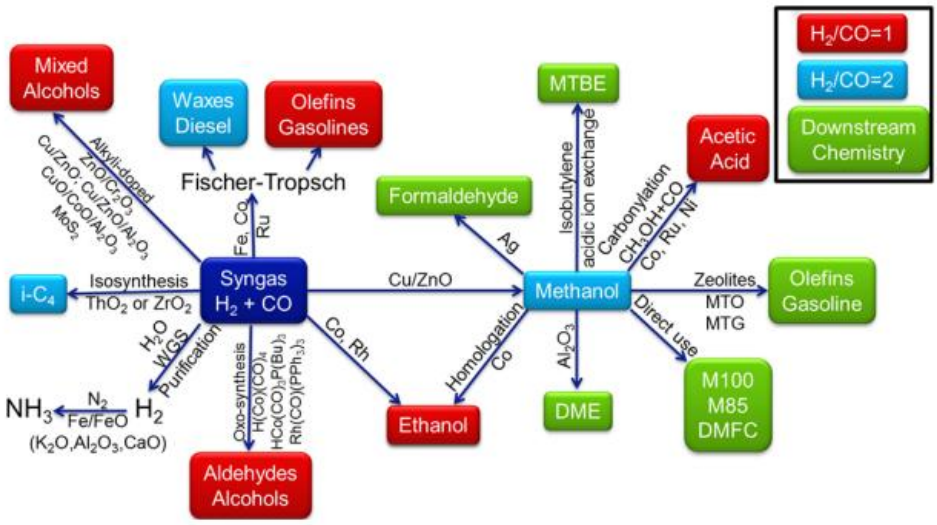

Figure 1.1 – Use of syngas in the chemical industry.[5]

The three main methods used for the abatement of contaminants in biomass derived syngas are catalytic conversion, thermal conversion, or selective sorbents.[4, 10] Thermal conversion could reduce quantities of methane and selective sorbents could be used to target removal of carbon dioxide but catalytic conversion has the potential to remove methane and carbon dioxide simultaneously. The syngas clean-up technology that offers the most advantages is catalytic conditioning downstream from the gasification reactor.[6] Catalytic conversion of biogas contaminants shows promising industrial application of biogas upgrading as it can be operated at the same temperature of the gasifier, it does not create waste water, and improves carbon efficiency by creation of additional syngas.[4]

Methane dry reforming (Equation 1) and methane steam reforming (Equation 2), are syngas upgrading reactions that can reduce methane and carbon dioxide and produce a syngas of suitable H_2/CO ratio for the desired downstream processes.

$$CH_4 + CO_2 \leftrightarrow 2CO + 2H_2 \quad \Delta H^0_{298K} = -247 \text{ kJ/mol} \quad (1)$$

$$CH_4 + H_2O \leftrightarrow CO + 3H_2 \quad \Delta H^0_{298K} = 206 \text{ kJ/mol} \quad (2)$$

Methane steam reforming has been practiced commercially since the 1930s. Recently, catalytic reforming of methane with carbon dioxide (methane dry reforming) to produce syngas has been cited as one of the most promising technologies for utilization of these greenhouse gases.[11] A commercial reforming catalyst should be capable of reforming methane, easily regenerated, and able to provide a suitable syngas ratio for intended use. Further, reduction of methane and carbon dioxide by a suitably cheap technology drastically enhances the economic viability of biomass gasification. [4, 7]

1.2 Catalysts for Conditioning of Biomass Derived Syngas

The most significant body of literature concerning catalytic conditioning of biomass derived syngas focuses on nickel catalysts.[7] Commercial nickel catalysts are commonly used for steam reforming of methane, dry reforming of methane, partial oxidation of methane, steam reforming of naptha, and hydrogenation reactions.[6] They have been widely tested and are known for their high rate of tar destruction, hydrocarbon reforming, water gas shift promotion, ammonia decomposition, and ability to provide a gas composition of syngas quality.[4, 7] A major drawback of the use of nickel catalysts for reforming reactions is deactivation due to repeated high temperature exposure that leads to sintering and phase transformation.[9] A variety of supports have been investigated for dispersing the nickel active phase for reforming reactions: CaO, CeO_2, TiO_2, MgO, ZrO_2, SiO_2, Al_2O_3. If a low surface area support is used (such as CaO, CeO_2, TiO_2, MgO, ZrO_2) then phase transformation of the support can be avoided, but sintering of the active metal will be increased [12] requiring high metal concentrations for sufficient reforming activity. If a high surface area support (such as SiO_2, Al_2O_3) is used

for reforming catalysts, effective utilization of the active metal can be achieved but volatilization of support species (SiO_2) [13], increased acid sites (SiO_2, Al_2O_3), and phase transformation (Al_2O_3) [14] of the support are of concern. It has been frequently found that supporting nickel on γ-Al_2O_3 offers superior properties for nickel reforming catalysts.[4, 12, 15-17] The advantages of using γ-Al_2O_3 have been attributed to the strong metal support interactions, resistance to sintering, and effective utilization of metal allowing for lower metal concentrations.[15, 18, 19] The importance of optimal metal-support interactions to increase dispersion and prevent sintering have been previously demonstrated,[12, 20] and sintering/oxidation behavior of Ni/Al_2O_3 catalysts crucially influences the catalytic performance in various applications.[18] Strong metal support interactions can reduce sintering and coke formation which are the major modes of deactivation in reforming reactions.[19] However, a unified view of the exact nature of active sites for nickel as a function of metal support interactions has yet to be developed. Cobalt alumina catalysts have been less studied for reforming reactions than nickel catalysts, but several studies have indicated they may have increased activity and stability.[3, 16, 21-23]

1.3 Rational Catalyst Synthesis

The majority of catalysts studied for reforming reactions are prepared by impregnation methods. This method of catalyst preparation is often un-reproducible from lab to lab and results in poor metal dispersion. A common fault in catalytic studies is to prepare catalysts by uncontrolled methods and spend weeks, if not months, characterizing them.[24] The advancement of the art of catalyst synthesis to a science has taken great strides in recent years. Rational synthesis methods such as chemical vapor deposition,

deposition precipitation, ion exchange, and strong electrostatic adsorption are being widely used for preparation of heterogeneous catalysts.[25-27] Strong electrostatic adsorption has been repeatedly proven to be reproducible and results in catalysts with higher dispersions and smaller metal particles than catalysts prepared by impregnation methods.[28-37] In strong electrostatic adsorption the metal complex is adsorbed onto the support through electrostatic interactions by adjusting the pH of the impregnating mixture to maximize metal support interactions.

Bulk materials that are of interest for reforming reactions, such as nickel aluminates, can be synthesized by many rational synthesis methods such as Pechini,[38-41] sol-sol,[42] sol-gel, [43] copreciptation,[44] combustion,[45] or alkoxide.[46] Pechini synthesis creates a polymeric resin by use of metal ions complexed by citric acid and ethylene glycol.[47] The resin is subsequently calcined to produce the desired mixed metal oxide. Synthesis using this method reduces the individuality of the metal ions and results in a very uniform mixed metal oxide. Further, nickel aluminate offers the potential of superior robustness compared to supported metal catalysts and have been widely examined for reforming reactions.[19, 39, 48, 49]

1.4 Objectives and Organization

The overall objective of this work is to investigate the effect of rational synthesis methods on activity and selectivity of reforming catalysts for upgrading of biomass derived syngas. This knowledge will help to further the use of rational synthesis methods by demonstration of the resultant superior properties of the prepared catalyst relative to catalysts prepared in less controlled manners. In the second chapter, the effect of preparation methods for cobalt on alumina catalysts for methane dry reforming was

examined. In attempting to synthesize cobalt catalysts by controlling adsorption it was found that cobalt chemically interacts with the surface hydroxyls of γ-Al_2O_3 surface rather than adsorbing through electrostatic interactions. Preparation of Co/Al_2O_3 catalysts by controlled adsorption resulted in a catalyst with small metal particles and a high dispersion and thus high activity and selectivity for the methane dry reforming reaction. In the third chapter, the effect of preparation methods on alumina supported nickel catalysts with low weight loading for methane dry reforming was studied. In the case of nickel deposition on γ-Al_2O_3, it was found that both electrostatic and specific interactions are involved in the adsorption phenomena. Controlling the adsorption of nickel onto the γ-Al_2O_3 support again resulted in a catalyst with a high dispersion, and thus, high activity for methane dry reforming. Further, significant insight was gained on the active sites on nickel catalysts which have been widely studied for many reactions since the 1950s. In the fourth chapter nickel aluminates prepared by Pechini synthesis were studied for methane dry reforming and methane steam reforming. Nickel aluminates were found to be stable, robust candidates for reforming reactions with very unique structural properties. Activity and selectivity for the studied reactions are found to be a due to different types of active sites present in the nickel aluminates under reduced or oxidized conditions.

CHAPTER 2

Effect of Preparation Methods on the Performance of Co/Al_2O_3 Catalysts for Dry Reforming of Methane

2.1 Background

Renewable energy sources are of growing importance and gasification of second generation biomass feedstocks is an attractive route for production of green fuels and chemicals. However, efficient cleaning and conditioning of biomass derived syngas is still a major technical barrier. [7] Biomass derived syngas generally has a high content of carbon dioxide and methane that must be either separated or reformed to CO and H_2 before the syngas is suitable for downstream processing to fuels or chemicals. Carbon dioxide separation is known to be expensive and thus, methane dry reforming is a desired step in upgrading of biomass derived syngas. [3] Dry reforming of methane has also attracted much attention due to increased interest in the effective utilization of these greenhouse gases. [2, 3]

Cobalt catalysts supported on γ-Al_2O_3 are commonly used for hydrogenation reactions, Fischer-Tropsch synthesis, [50] and hydrotreating of crude oil. [51] Cobalt catalysts have also found application as sulfur resistant catalysts and have been used for the WGS reaction. [33] However, few studies have focused on the use of cobalt catalysts for methane steam and dry reforming reactions. [11, 23]

Catalysts used in the investigation of methane dry reforming are commonly prepared using impregnation methods. Impregnation methods are routinely implemented

to synthesize catalysts on an industrial scale. In dry impregnation (DI), a solution of metal salt is prepared in a volume of water sufficient to fill the pore volume of the support [27] Often, in this method of preparation, only low weight loadings can be achieved because the concentration of the metal salt is beyond the solubility limit and successive impregnations must be carried out to achieve the desired weight loading. [26] One advantage of this method is that no filtration is necessary, and no metal is lost. However, the deposition of the metal precursor occurs through precipitation during drying.[52] Thus, the resulting metal support interactions are very weak, and there is little control over the deposition of the metal often resulting in low dispersion.[27, 37]

In many studies, different results are obtained for similar catalytic systems because synthetic methods do not commonly exercise control of active site formation.[24] There has been much effort devoted to the fundamentals of catalyst synthesis so that the deposition of the metal precursor is controlled and catalysts can be synthesized in a reproducible manner. Strong electrostatic adsorption (SEA) is one such rational synthesis method that has been proven to be reproducible and results in catalysts with higher dispersions and smaller metal particles than catalysts prepared by impregnation methods. [28-37] Deposition of metal particles by SEA involves only electrostatic (non-specific) interactions between the metal precursor and the support. Some metal-support systems exhibit chemical (specific) interactions with the support in addition to electrostatic ones. Another rational synthesis method where the adsorption of the metal is controlled is equilibrium deposition filtration (EDF). Extensive work has been conducted on EDF preparation of catalysts where deposition of metal particles occurs through specific (in addition to non-specific) interactions such as adsorption

through hydrogen bonds, formation of innersphere complexes, or interfacial precipitation.[52-59] The extent to which any of the aforementioned types of specific interactions occurs depends on the nature of the complex, the ionic strength, and the impregnating temperature and time used during synthesis.[59]

The details of adsorption phenomena of metal precursors at the solid aqueous interface have long been, and are still, a source of disagreement.[53, 54, 56, 60-63] A non-specific interacting complex is weakly linked through electrostatic forces, van der Waals forces, or hydrogen bonding (e.g. SEA). Non-specific complexes can be accurately described using a double layer model in which only the outer Helmholtz plane (OHP) is considered (Figure 2.1a).[56] Specific interactions of a metal complex with an oxide support can be described in terms of hydrogen bonds, ion pairing, or ligand exchange (e.g. EDF). To describe specifically interacting complexes a complex triple layer model is implemented where the OHP and inner Helmholtz plane (IHP) are considered (Figure 2.1b – 2.1d). The word "specific" indicates that adsorption constants differ within a group of cations of the same valence, an implication of this specificity is that not only electrostatic but also chemical interactions are involved in the adsorption process.[64] As noted by Haworth in his review of modeling sorption from aqueous solution it is difficult to distinguish between the effects of electrostatic and chemical interactions with oxide supports.[65]

In this study, the possible adsorption phenomena that occur during catalyst preparation, the effect of preparation method on types of active sites formed, and catalytic activity of 2 wt% Co/Al_2O_3 in methane dry reforming reactions are explored.

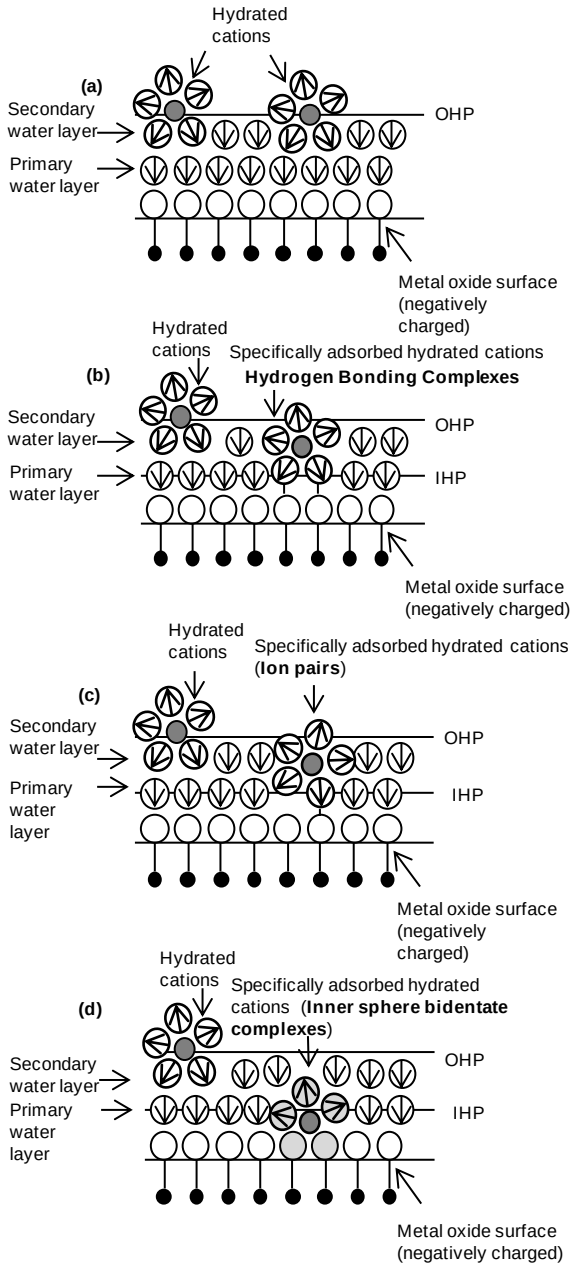

Figure 2.1 - (a) Non-specific (electrostatic) adsorption. Double layer description of the metal oxide-water interface where OHP is the outer Helmholtz plane. Specific adsorption of metal complexes at the oxide-water interface, best described using triple layer model where IHP is the inner Helmholtz plane. Complexes can specifically interact with the surface in several ways, such as, (b) hydrogen bonding complexes (c) ion pairing (d) inner-sphere complexes. Based on [56].

2.2 Materials and Methods

2.2.1 Materials

Aluminum oxide, γ-phase, 99.97% metals basis (Alpha Aesar, surface area 80 – 120m^2/g) was used as received. $Co(NO_3)_2$ (99.999% trace metals basis) from Aldrich was used as the metal precursor for catalyst synthesis. HCl and NaOH (A.C.S. reagent grade) from Sigma were used as pH adjustors in pH precipitation studies, adsorption isotherms, and catalyst synthesis as discussed below. Deionized water was used throughout this study.

2.2.2 Controlled Adsorption (CA) Synthesis Optimization

2.2.2.1 Point of Zero Charge

To determine the point of zero charge (PZC) of the γ–Al_2O_3 support, pH solutions ranging from 0.5 to 13 were prepared using HCl or NaOH. The mass of alumina used corresponded to a surface loading (S.L.) of alumina of 1000 m^2/L. The support was contacted with the solutions, shaken for one hour, and the final pH was then measured. A glass bodied Thermo Scientific Orion pH probe (9102BNWP) was employed for all pH measurements. The pH meter was calibrated using standard buffer solutions at the start of every experiment. The experiments were conducted using 50 mL polypropylene bottles at room temperature

2.2.2.2 pH Precipitation Studies

Solutions with pH values ranging from 5.5 to 13 were prepared using NaOH at room temperature. 200 ppm cobalt (as cobalt nitrate hexahydrate) was added to the solutions. The solutions were shaken for one hour, and the final pH was determined. Any sign of precipitation (and its color) at a given pH value was noted. Solutions were then filtered using 0.2 μm nylon membrane filters.

2.2.2.4 Precursor Adsorption as a Function of Time (Constant pH)

200 ppm of cobalt (as $Co(NO_3)_2$) was added to an aqueous solution adjusted to a pH of 8.5 using NaOH at room temperature. Samples of the impregnating solution were taken at 30 minute intervals, and the pH re-adjusted to 8.5 for a total time of 2.5 hours. The liquid samples were filtered using 45μm nylon syringe filters and analyzed by ICP-OES using a Perkin Elmer Optima 3000 DV.

2.2.3 Catalyst Preparation

2.2.3.1 Controlled Adsorption (CA)

Cobalt was deposited using a cyclic procedure as described above. Specifically, 200 ppm of cobalt (as $Co(NO_3)_2$) was added to an aqueous solution adjusted to a pH of 8.5 using NaOH at room temperature. The pH of the impregnating solution was re-adjusted to 8.5 every 30 minutes using NaOH over a period of 2 hours at which time deposition of all cobalt in solution had occurred. The catalyst was then filtered and washed twice with deionized water. The 2 wt% Co/Al_2O_3 catalysts prepared in this cyclic manner will henceforth be designated 2CoCA (controlled adsorption).

2.2.3.2 Dry Impregnation (DI)

The weight loading for catalysts prepared by dry impregnation was chosen to be the same as the 2CoCA catalyst. The desired amount of complex was dissolved in a volume of water that corresponded to the pore volume of the support as determined by nitrogen physisorption. The precursor solution was added to the support and allowed to stir for 1 h at room temperature. The 2 wt% Co/Al_2O_3 catalysts prepared in this manner will henceforth be designated 2CoDI.

2.2.2.3 Calcination

Prepared catalysts were dried in an oven at 110 ℃ for 10 minutes prior to calcination. Samples prepared by different methods were heated to 500 °C. Zero air generated using a zero air generator (VWR, 26000-020) at a flowrate of 150 mL/min and a heating rate of 5 ℃/min. The zero air generator produces UHP zero air with a purity level below 0.05 ppm total hydrocarbon content from the compressed air supply. Samples were calcined for 3 h.

2.2.4 Characterization

2.2.4.1 Nitrogen Physisorption

N_2 adsorption/desorption isotherms at -196 ℃ were measured for calcined catalysts using Micromeritics ASAP 2020. Approximately 0.5 g of sample was used in all experiments to minimize instrument error. The samples were outgassed for 3 h under vacuum at 300 ℃. The specific surface area was calculated using the BET equation.

2.2.4.2 Elemental Analysis

To determine the cobalt content, the 2CoDI and 2CoCA catalysts were externally analyzed for cobalt and aluminum concentration by Gailbraith laboratories. HF digestion was used to dissolve the alumina support so that the cobalt content could be accurately determined by ICP-OES.

2.2.4.3 Temperature-Programmed Reduction

Temperature programmed reduction was carried out using Micromeritics ASAP 2920 equipped with a TCD detector, a reference chamber, and a cold trap. The cold trap contained a mixture of dry ice and isopropyl alcohol. The reducing gas was a 10% H_2/Ar mixture at a gas flowrate of 50 mL/min, and approximately 40 mg of catalyst was used in all experiments. The temperature was ramped from 25 ℃ to 1000 ℃ at 5 ℃/min.

Obtained traces were normalized with respect to the amount of sample used during the experiment.

2.2.4.4 H_2 Chemisorption

Metal dispersion was analyzed using a Micromeritics Chemisorb 2750 using hydrogen. The sample was evacuated at 110 °C for 60 min to remove ambient gases. The temperature was ramped from 110 °C to 600 °C at 2 °C/min and held at 600 °C for 8 h. The sample was then evacuated and cooled to 550 °C and held there for 16 h to remove residual hydrogen. Finally, the sample was cooled to 25 °C at which time H_2 gas was dosed and the analysis was performed. Two isotherm measurements were performed and the metal surface area was calculated using H/M ratio of 1.[66] Approximately 40 mg of catalyst was used in all experiments.

2.2.4.5 Transmission Electron Microscopy

Transmission electron microscopy (TEM) observations were performed with a FEI Titan 80-300 operated at 300 kV. The instrument is equipped with CEOS GmbH double-hexapole aberration corrector for image-forming lens, which allows imaging with sub angstrom resolution. Compositional analysis was performed with EDAX Si(Li) EDS detector, and the analysis of the obtained spectra was performed with FEI TIA software. The samples for TEM observations were prepared by dispersing a dry powder on a lacey-carbon coated 200 mesh Cu TEM grids. The as prepared grids were then immediately loaded into the TEM airlock to minimize an exposure to atmospheric O_2.

2.2.4.6 X-ray Photoelectron Spectroscopy

XPS was performed on post reaction catalysts using a Thermo K-Alpa instrument equipped with a monochromatic small-spot X-ray source and a 180° double focusing

hemispherical analyzer with a 128-channel detector. Spectra were obtained using an aluminum anode Al Kα ($h\nu$ = 1486.6 eV). The background pressure was 4.9×10^{-8} bar and 4×10^{-7} bar argon during measurement because of the charge compensation dual beam source which was used to prevent sample charging. The binding energies were referenced to the sample stage which contains built in calibration standards of copper, silver, and gold.

2.2.5 Reactivity studies

Methane dry reforming reactions were performed in a quartz reactor using a stoichiometric mixture of methane and carbon dioxide. Reactivity studies were conducted using 200 mg of catalyst. Catalyst samples were reduced in-situ at 600 °C in a 20% H_2/N_2 mixture for two hours prior to reactivity studies. A space velocity of 22,000 h^{-1} of reactant gas was employed. The temperature was 700 °C and pressure was atmospheric. Product gas was sampled at 20 minute intervals using an online Bruker 450-GC refinery gas analyzer (RGA). The RGA is equipped with two TCD detectors and a FID. One TCD is used for analysis of hydrogen and the second for analysis of permanent gas mixtures (including methane). The FID channel allows for identification of methane and higher hydrocarbons (and confirmation of methane concentration from the middle TCD). Spent catalysts were externally analyzed for C, H, N concentrations by Gailbraith laboratories to determine the amount of carbonaceous material deposited on used catalysts.

2.3 Results and Discussion

2.3.1 2CoCA synthesis optimization

<u>2.3.1.1 Point of Zero Charge</u>

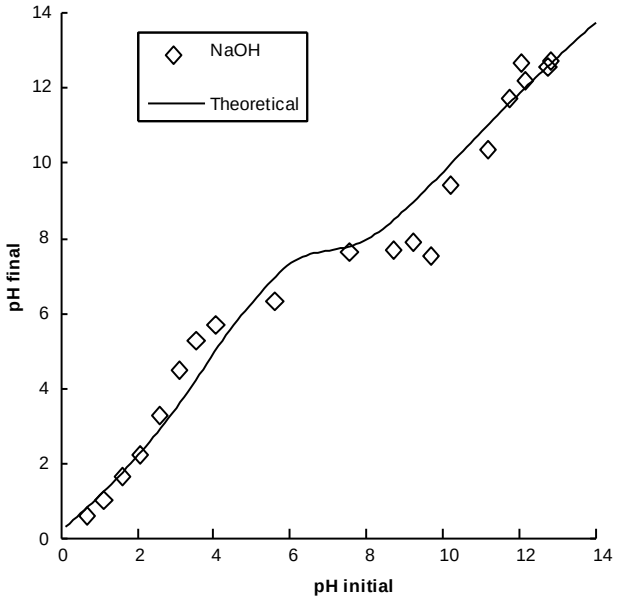

Figure 2.2 - Experimental PZC data fit with theoretical model. Adjustable parameters, PZC = 7.7. Adjustable theoretical model parameters; difference between pK_1 and pK_2 (ΔpK) = 5.0, Number of charged sites (N_S) = 8 OH/nm^2,[67] 25 °C.

The point of zero charge (PZC) of a metal oxide support is the point at which the support surface is neutrally charged. At pH values above the PZC of the metal oxide the surface is deprotonated (negatively charged) and cationic species can be electrostatically adsorbed. At pH values below the PZC the surface is protonated (positively charged) and anionic species can be adsorbed. The metal precursor used in this study ($Co(NO_3)_2$) is cationic. To define appropriate conditions for Co^{2+} deposition, it was necessary to determine the point of zero charge (PZC) of the alumina support. The plateau (Figure 2.2) represents the PZC and exists because the number of surface OH groups far outnumbers the quantity of OH^- ions initially present in solution[37] Consequently, alumina buffers the solution at its PZC. The PZC of alumina used in our study was found to be at a pH of 7.7. The value of the PZC was determined by averaging the data points that comprise the plateau in Figure 2.2. Details of the theoretical model applied to the PZC data can be

found in [67]. Briefly, two parameters of the model are adjustable; the total number of charged sites N_s and the difference between pK_1 and pK_2 (ΔpK). For alumina, these values can be readily found in literature; N_s = 8 OH/nm^2 and ΔpK = 5.[60, 68] It should be noted here that, ideally, to adsorb cations by a purely electrostatic mechanism a support with a lower PZC is selected.[37] However, for reforming applications, low PZC materials such as silica or most amorphous silica alumina are not viable. Specifically, the high acidity of typical amorphous silica-alumina increases coking during catalytic reactions at high temperature. Coking is one of the main deactivation mechanism of methane dry reforming catalysts reported in literature.[11] Additionally, the high reaction temperature required for reforming reactions may cause vaporization of silica.[69] Therefore, alumina is a much more suitable support for the reaction conditions studied herein.

2.3.1.2 pH-Precipitation Studies of Co^{2+}

The PZC of the alumina used in this study is relatively high for adsorption of cationic complexes. Because the PZC of alumina is at a pH of 7.7, one must be concerned about partial dissolution of the support at high pH and also precipitation of cationic complexes in highly alkaline solutions. The use of cationic precursors of cobalt was desired to avoid the use of anionic cobalt complexes, which are often toxic, water insoluble, or large organic molecules [70] and thus undesirable for industrial application. To investigate cobalt cation complex stability in alkaline solutions, the desired concentration of $Co(NO_3)_2$ was added to solutions with pH values between 5.5 and 13. The first point at pH of 5.5 corresponds to pure deionized water with no base added. Initial pH refers to the pH of the solution without $Co(NO_3)_2$ and the final pH refers to the

pH of the solution after contact with 200 ppm Co^{2+} for one hour. The resultant metal solutions were subsequently filtered and the color of precipitate was noted. The point of bulk precipitation observed upon filtering of the solutions is indicated by the line in Figure 2.3.

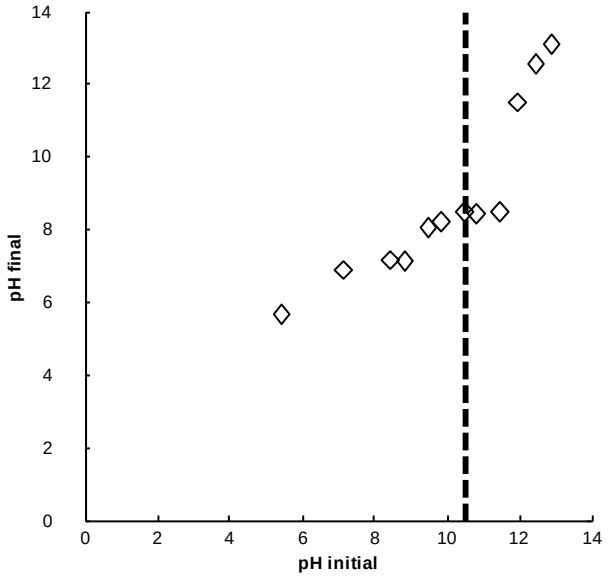

Figure 2.3- pH shift of Co^{2+} (as cobalt nitrate) in NaOH and point of observed precipitation (- - -), 25 °C.

The metal precursor solution shifted the pH of the mixture due to equilibration of the various types of ionic species in solution. As expected, Co^{2+} was found to have low solubility at alkaline conditions. The color of the precipitate was observed to change from blue to green to brown with increasing pH. The blue precipitate is indicative of unstable $Co(OH)_2$.[70] The green precipitate is thought to be formed by oxidation or mixing of various types of cobalt hydroxide (e.g. unstable/stable $Co(OH)_2$). The brown precipitate results from pale pink $Co(OH)_2$ that has been freshly precipitated with NaOH and oxidized to brown CoO(OH).[70] The various amounts and types of precipitation that

occur at each pH point examined indicate complex solution chemistry. Several important synthesis considerations are revealed in light of this study: pH ranges where bulk precipitation occurs are identified and thus can be differentiated from adsorption during adsorption isotherm measurements (vide infra); the metal precursor should be allowed to equilibrate followed by re-adjustment of the mixture to the desired pH value before contact with the support; the types of cobalt species that exist in solution are dependent on the pH value being examined. It should be noted that once alumina is added to the alkaline cobalt solution additional species could be formed in solution, however, valuable insight has been obtained regarding bulk solution behavior.

2.3.1.3 CA Adsorption Studies

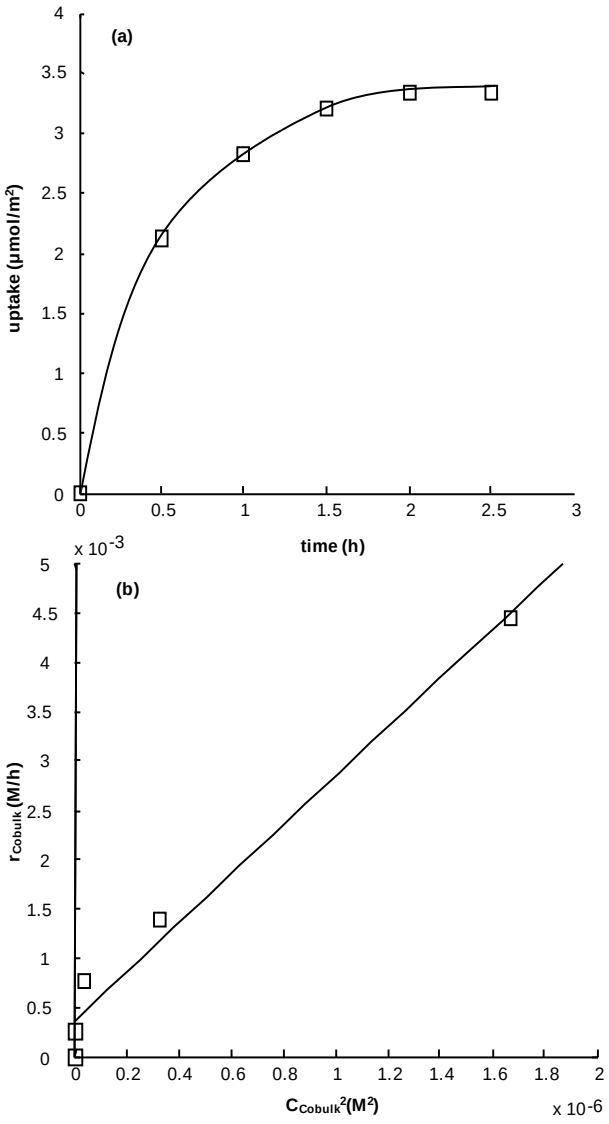

Figure 2.4 – (a) Experimental data for cyclic Co deposition at 25 °C (b) kinetic expression for $Co(II)(NO_3)_2$ deposition at C_{Cosurf} = 4.2 µmolm^{-2} (1 theoretical surface layer of $Co(H_2O)_6^{2+}$) [62, 67] , k' = 2573.5 (L mol^{-1} h^{-1}), R^2 = 0.978.

Figure 2.4a shows the experimental data for Co^{2+} uptake as a function of contact time with the support at a constant pH of 8.5. This pH was selected so that the pH of the impregnating mixture was above the PZC of the support and below pH values where bulk precipitation was observed. The pH of the impregnating solution was adjusted to a value

of 8.5 every 30 minutes, similar to the approach of Lycourghiotis et al.,[58] and a sample was taken to monitor the removal of cobalt from the impregnant solution. Deposition of all cobalt in solution was completed by 2 hours as shown in Figure 2.4a. In Figure 2.4b the rate of disappearance of cobalt from the bulk solution is plotted versus the square of the concentration of Co^{2+}. Following Lycourghiotis et. al.,[58] cobalt deposition can be described by the kinetic equation,

$$r_{Co,bulk} = k'C^2_{Co,bulk} \quad (1)$$

The above kinetic expression was derived assuming the following deposition scheme,

$$nS + 2[Co(H_2O)_6]^{2+} \rightarrow S_n - [Co(H_2O)_{x,x<6}{}^{2+}]_2 \quad (2)$$

Where, S is a surface receptor site on the metal oxide support and n is the number of surface sites. This mechanism implies that two $Co(H_2O)_6{}^{2+}$ ions are adsorbed on a surface site, possibly due to simultaneous adsorption and dimerization of two interfacial cobalt ions through (hydr)oxo-bridges, and is depicted in Figure 2.5. However, such a synchronized event is rather unlikely to occur. We alternatively suggest that the rate of cobalt deposition is controlled by the dimerization of $[Co(H_2O)_6]^{2+}$. Once this has occurred adsorption of the dimer appears to be fast.

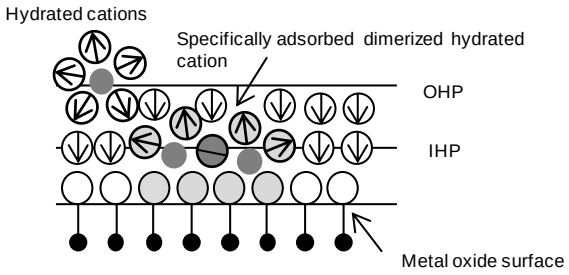

Figure 2.5 - Kinetic deposition of cobalt dimers at the alumina interface. $[Co(H_2O)_6]^{2+}$ dimerizes in solution and then is rapidly adsorbed onto the surface.

The kinetic equation (Equation 1) derived from a specific interaction deposition scheme suggested by Lycourghiotis et al. is sufficient to describe the adsorption phenomena in this study.[55] Since the pH used during adsorption isotherms (pH = 8.5) is close to the PZC of the support, it is likely that there is a low concentration of deprotonated surface hydroxyls. Thus, it is favorable for cobalt ions that are close to the surface dimerize because this reaction allows the cobalt species to bridge between two separated surface hydroxyls without increasing its charge. Once the dimers have formed, they rapidly adsorb. Additionally, non-negligible deposition near the PZC of the support is indicative of specific interactions. Co^{2+} deposition on alumina has been reported to exhibit mostly specific interactions and the nature of the metallic complex and its interaction(s) with the solid surface seem to play an important role.[55, 56, 63, 71] Extensive work has been conducted at the University of Patras on the application of equilibrium adsorption filtration (EDF) of Ni and Co on Al_2O_3.[52-58] Lycourghiotis found that for Co(II) adsorption on alumina, above 0.33 theoretical $[Co(H_2O)_6]^{2+}$ layers the Co(II) speciation changes from binuclear, oligonuclear, and multinuclear inner-sphere surface complexes to $Co(OH)_2$ like precipitate at relative high Co(II) surface concentrations. It was found that these $Co(OH)_2$ precipitates formed at lower pHs than

those required for bulk precipitation.[55] In this study, one theoretical $[Co(H_2O)_6]^{2+}$ surface layer was used to minimize the amount of $Co(OH)_2$ precipitation while still preparing a catalyst with a reasonable cobalt content, e.g. 2 wt% cobalt-alumina. Another important implication of utilizing low weight loading cobalt on alumina catalysts is the idea that the dispersion can be increased thus decreasing coke formation since large particles stimulate coke formation.[72]

2.3.2 Characterization of 2wt% Co/Al_2O_3 Catalysts Prepared by CA and DI

2.3.2.1 N_2 physisorption, Elemental Analysis, H_2 chemisorption, and TEM

Table 2.1 shows the results from N_2 physisorption, elemental analysis, and H_2 chemisorption measurements. Elemental analysis confirmed that 2CoCA and 2CoDI had the desired amount of cobalt. The surface area was similar for catalysts prepared by both methods. The supported Co catalysts had slightly lower surface area and larger pore volume and pore diameter than that of the fresh alumina support presumably, due to phase transformation of the alumina support and precipitation of the metal precursors upon calcination. H_2 chemisorption measurements show that 2CoCA catalysts have a higher dispersion and smaller metal particle size than the 2CoDI sample. The reported values of dispersion are within the range of those reported for cobalt alumina catalysts in literature.[73-75]

Table 2.1 - N_2 physisorption, elemental analysis, and H_2 chemisorption of prepared catalysts.

Sample	**Surface Area (m^2/g)[a]**	**Pore Volume (cm^3/g)[b]**	**Average Pore Diameter (nm)[c]**	**Elemental Analysis (wt% Co)[d]**	**Average Metal Particle Diameter (nm)[e]**	**Dispersion (%)[f]**
2CoCA	88	0.35	14.7	2.01	19.4	5.1
2CoDI	84	0.31	16.0	2.02	28.0	3.5
Fresh Alumina	91	0.24	10.8	-	-	-

[a] **Calculated from N_2 physisorption data using the BET equation**
[b] **Calculated from N_2 physisorption data using single point adsorption at $P/P_0 = 0.99$**
[c] **Calculated from N_2 physisorption data using 4V/A from BET**
[d] **Elemental analysis determined using ICP**
[e] **Average cobalt crystallite size calculated using H_2 chemisorption data**
[f] **Cobalt dispersion calculated using H_2 chemisorption data**

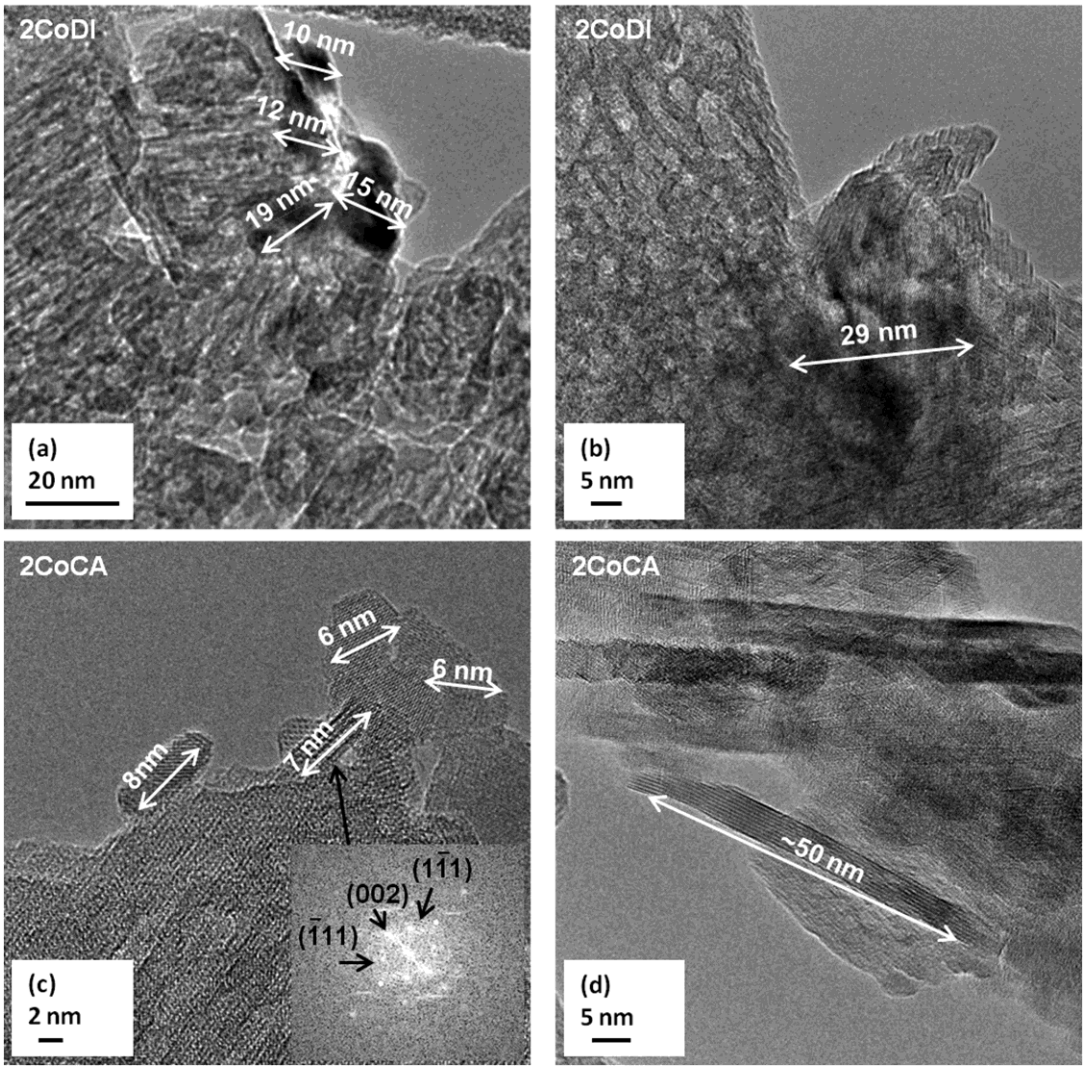

Figure 2.6 – Top: 2wt% Co/Al_2O_3 prepared by DI. Bottom: 2wt% Co/Al_2O_3 prepared by CA.

TEM images show that Co/Al_2O_3 prepared by DI contained Co particles that range from 10 to 40 nm in size (Figure 2.6a and 2.b). In contrast, most Co particles on Co/Al_2O_3 prepared by CA were significantly smaller (*i.e.* 6-8 nm) as shown in Figure 2.6c and 2.6d. However, large particles are also present on the CA samples, which contribute to the average reported particle size by chemisorption (Figure 2.6d). As mentioned in the discussion of the synthesis of cobalt-alumina catalysts by CA, the

deposition of Co^{2+} likely takes place through dimerization of cobalt ions and specific interactions with the alumina surface. Based on TEM images, it is speculated that in some instances, large oligomers are formed in solution and adsorbed on the surface or interfacial precipitation occurs leading to the observed large particles. Careful control of the mode of interfacial deposition could allow for a much finer tuning of the size of supported metal particles.[59] It is suggested that the formation of oligomers and the occurrence of surface precipitation could be avoided by reducing the initial concentration of cobalt in the impregnating mixture and performing successive impregnation steps with intermittent mild calcination treatments. This successive type impregnation to control the mode of deposition was successfully demonstrated for Pt/C catalysts prepared by strong electrostatic adsorption.[76] In the case of cobalt-alumina catalysts by DI, deposition of the Co^{2+} takes place during drying/calcination. Since this deposition method lacks the strong interaction with well-dispersed surface sites, the large average size of the particles is not surprising.

2.3.2.2 Temperature Programmed Reduction

Figure 2.7 shows the hydrogen concentration measured using a TCD detector during temperature programmed reduction (TPR) experiments for prepared catalysts, and Table 2.2 shows the hydrogen consumption normalized by the catalyst weight used in the experiment.

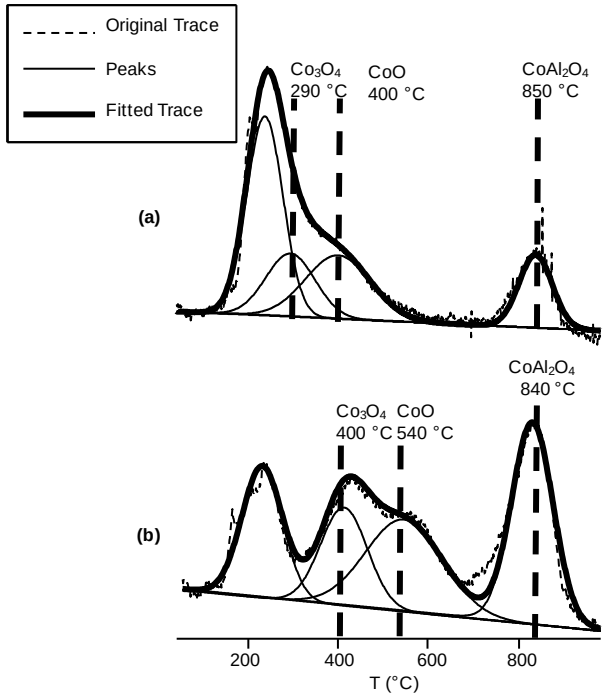

Figure 2.7 – TPR profiles (a) 2CoDI (b) 2CoCA.

Table 2.2 – Hydrogen consumption per gram of sample for different TPR peaks based on TCD signal.

Peak Assignment	**-NO_3** [a]	**Co_3O_4 → CoO**	**CoO→ Co^0**	**$CoAl_2O_4$**
2CoDI μmolH_2/ g_{cat}	-	79	105	61
2CoCA μmolH_2/ g_{cat}	-	93	141	168

[a] Hydrogen consumption omitted due to volatilization of nitrate species that affect TCD response

Four distinct peaks were observed during TPR experiments. The first peak at approximately 200 °C for both samples is attributed to decomposition of residual nitrate.[77, 78] The 2CoDI catalyst desorbs more residual components than the 2CoCA sample. This is expected because the 2CoCA sample was washed twice with de-ionized water prior to calcination. Due to the expected desorption of species other than H_2 (e.g.

NO_2, NO, N_2O_5, NH_3, etc.) and their contribution to the TCD signal, the exact values of H_2 consumption for the first peak are omitted. Peaks in the region of 300 °C and 600 °C are usually assigned to reduction of Co_3O_4 to CoO followed by CoO reduction to metallic Co.[79-81] In most TPR studies on supported Co catalysts, it is concluded that two phases exist on the support: a crystalline phase as Co_3O_4 and stoichiometric and non-stoichiometric cobalt aluminate. [75, 82, 83] Following literature assignments, the fourth peak in the TPR spectra is attributed to reduction of surface $CoAl_2O_4$.

For the reduction of Co_3O_4 to Co^0, the two reduction steps are not always observed as separate TPR peaks,[23, 75] as can be seen in Figure 2.7a. It has been found that strong interactions between the support and Co_3O_4 crystallites can manifest separation of the two reduction peaks,[75] as can be observed in Figure 2.7b. This is expected as the CA preparation method should cause stronger metal support interactions than DI. 2CoDI samples have peaks at 290 °C and 400 °C, whereas the corresponding CA prepared samples exhibit two very distinct peaks at 400 °C and 540 °C. The 100 °C separation between the two reduction peaks is commonly noted.[80] Additionally, 2CoCA samples have higher reduction temperatures than the corresponding DI sample, again, due to stronger metal support interactions induced by preparation method. It is possible that an additional peak exists at approximately 600 °C for the 2CoDI sample. This peak could be assigned to reduction of Co^{2+} to Co^0 where the Co^{2+} is surrounded by more Al^{3+}.[84] This would create a polarization of CoO bonds, and thus these cobalt particles would be more difficult to reduce (and appear at a higher temperature) than the large peak at 410 °C attributed to reduction of Co^{2+}. However, due to the small quantity

of H_2 consumption it is assumed that this species, if it exists, is a minor component in the overall catalyst structure.

The areas of the two main peaks in the region of 300-700 °C are of great interest. From reduction stoichiometry, the ratio of the two peaks should be 1:3 for complete reduction. However, we see that for the 2CoDI sample a 1:1.3 ratio is obtained and for the 2CoCA sample a 1:1.5 ratio is obtained. Thus, the amount of cobalt reduced to its metallic state during TPR is greater in the 2CoCA sample than in the 2CoDI samples. Further, the obtained ratios indicate that neither of the samples is fully reduced to metallic state. Incomplete reduction of Co/Al_2O_3 catalysts is commonly cited in literature.[75, 85, 86] Guczi et al. reported a similar finding in his study of Pt-Co bimetallic catalysts. They concluded that the ratio of TPR peaks corresponding to Co_3O_4 to CoO and CoO to Co^0 was not 1:3 due to redisperison of the Co^{2+} ions spreading over the alumina, increasing the amount of Co surface spinel phase.[81, 84]

The fourth TPR peak, which is attributed to $CoAl_2O_4$ species, is much more pronounced in 2CoCA than 2CoDI samples. It seems reasonable that 2CoCA contains a greater amount of spinel phase because the preparation of this catalyst should cause strong metal support interaction and thus, surface spinel formation may be easier due to the intimate contact between the metal and support. It is currently not clear whether the cobalt spinel phase occurs during preparation, calcination, or reduction. However, from TPR, it can be observed that more reducible spinel species exist in the CA prepared catalysts and this catalyst visibly changes from dark green to light blue (indicative of $CoAl_2O_4$) after reduction/reaction, which could point to spinel formation during reduction.[87] Yan et al. found that the formation of $CoAl_2O_4$ occurred only after

treatment at 800 °C.[85] This high temperature treatment was said to promote the dispersion of Co_3O_4 clusters and resulted in the formation of $CoAl_2O_4$. As discussed in the preceding paragraph, the redispersion of the cobalt during TPR might explain the observed non-stoichiometric reduction.

2.3.3 Catalytic Tests

Few studies have compared the activities of catalysts for carbon dioxide reforming of methane prepared by different methods and those only focused on different impregnation methods. [2, 3, 11, 88, 89] To test the activity of catalysts prepared by DI and CA, methane dry reforming experiments were conducted for 8 hours at 700 °C using a stoichiometric feed of carbon dioxide and methane. The desired reaction is,[74]

$$CH_4 + CO_2 \leftrightarrow 2CO + 2H_2 \quad \Delta H^0_{298K} = -247 \text{ kJ/mol}$$

The inverse water-gas shift reaction may impact the target reaction,

$$CO_2 + H_2 \leftrightarrow 2CO + H_2O \quad \Delta H^0_{298K} = 41 \text{ kJ/mol}$$

Steam generation from the above reaction could promote the methane steam reforming reaction,

$$CH_4 + H_2O \leftrightarrow CO + 3H_2 \quad \Delta H^0_{298K} = 206 \text{ kJ/mol}$$

However, one of the major drawbacks of methane dry reforming catalysts is their deactivation due to carbonaceous deposits,

$$CH_4 \rightarrow C + 2H_2 \quad \Delta H^0_{298K} = 75 \text{ kJ/mol}$$

$$2CO \rightarrow C + CO_2 \quad \Delta H^0_{298K} = -171 \text{ kJ/mol}$$

San Jose et al. found an initial conversion of methane of 75% for a 9 wt% Co/Al_2O_3 catalyst at 700 °C, SV 20,000 h^{-1}, and stoichiometric CH_4:CO_2.[3] Remarkably, this catalyst was also found to have the highest amount of carbon deposited. It was concluded that the large Co particles (~14 nm) produced non-deactivating carbon deposits and were involved in long term conversion. In a subsequent work, San Jose et al. studied Co/Al_2O_3 catalysts with low metal loading. Under similar conditions to those utilized in this work (2.5 wt% Co/Al_2O_3, 700 °C, SV= 20,000 h^{-1}, CH_4:CO_2 ratio 1:1), they found that the initial conversion of methane was about 35% and decreased by 12% over 6 h.[89] Zhang et al. studied methane dry reforming activity of bimetallic Ni-Co-Mg-Al-O co-precipitated catalysts.[74] Conversion of methane was about 90%, the catalyst was stable over 28 h reactivity tests, and H_2/CO yields of unity were reported. In many studies, the H_2/CO ratio is found to be less than unity due to the reverse water gas shift reaction.[11] Zhang et. al also found higher methane conversion activity for lower metal loadings of Ni-Co when compared to catalysts that had higher loadings.[74] The methane conversion, carbon dioxide conversion, and H_2/CO molar ratio achieved for prepared catalysts are illustrated in Figure 2.8.

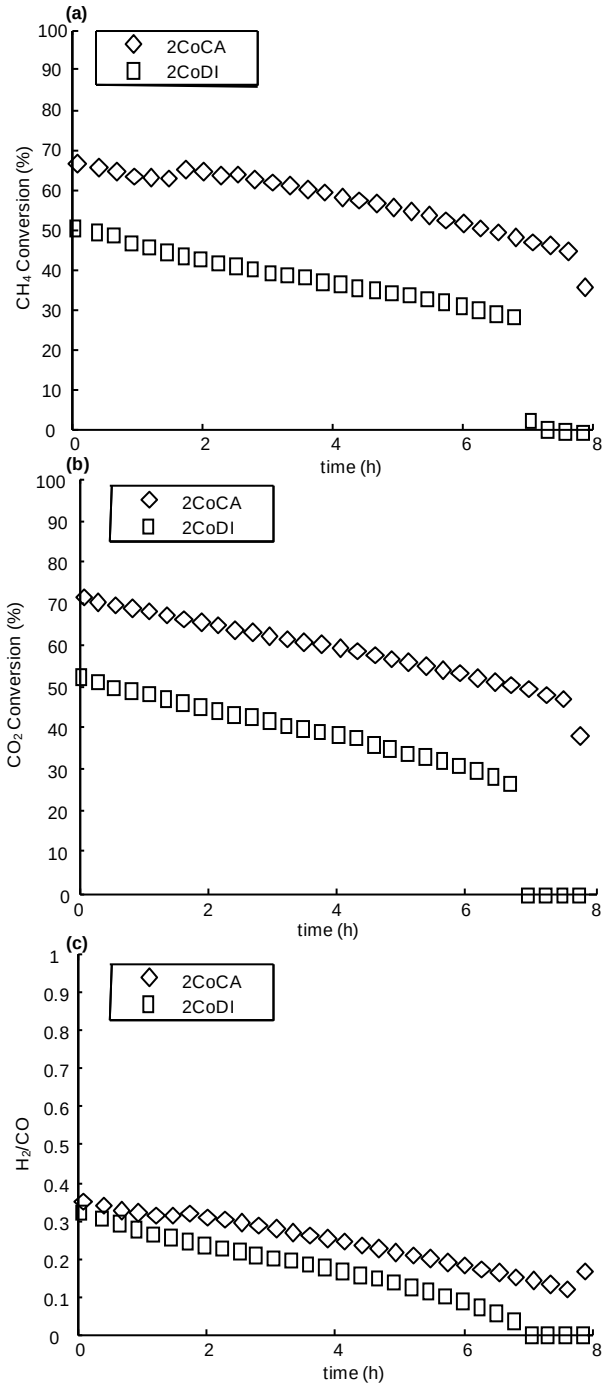

Figure 2.8 – (a) Methane conversion (b) Carbon Dioxide conversion (c) H_2/CO ratio for 2CoCA and 2CoDI.

2CoCA initially converted 68% of the methane and 71% of the carbon dioxide fed while 2CoDI catalysts initially converted 52% of each of the reactants fed. The H_2/CO

ratio is initially 0.35 for 2CoCA and 0.33 for 2CoDI. The high initial conversion indicates 2CoCA catalysts uses the Co present very effectively as these conversions are comparable to Co/Al_2O_3 catalysts with much higher weight loadings.[3] The difference appears to be due to the higher dispersion of Co in the 2CoCA sample. As noted earlier, the stability of cobalt alumina catalyst is of major concern. In this study, catalysts were only stable for the first two hours of reaction followed by slow but steady deactivation. In the context of methane dry reforming, there are three major possibilities for catalyst deactivation: sintering, metal oxidation and/or coking. Metal sintering might cause catalyst deactivation, however, the catalyst reduction temperature utilized prior to reactivity studies was quite high (600 °C, 2h). In a comparable study, Ferreira-Aparicio et al. showed that 5 wt% Co/Al_2O_3 did not deactivate due to sintering during methane dry reforming over a wide range of temperatures after calcination at 500 °C (3h) and reduction at 400 °C (4h).[90] Moreover, it is unlikely that the rapid deactivation after 7 hours on stream is caused by sintering, since sintering should deactivate the catalyst more steadily. Metal oxidation has been reported as a deactivation mechanism of cobalt based catalysts.[16, 72, 74, 91] The presence of oxygen from the dissociation of carbon dioxide can be responsible for the oxidation of cobalt under experimental conditions,[16] and thus the atmosphere on the surface may be both reducing and oxidizing.[72] Extrapolation of thermodynamic data for cobalt oxidation [92] indicates that cobalt oxidation is unlikely from the reaction conditions used in this study (low $p(H_2O)/p(H_2)$ ratio, high temperature). Due to the pronounced differences in the analysis of post reaction catalysts by C,H,N and XPS, we suggest that coking is the dominant route of catalyst deactivation, in the present study.

The most common problem of methane dry reforming on a commercial scale is catalyst deactivation due to coking.[11] Catalysts were analyzed after reaction for formation of carbonaceous deposits by C,H,N analysis. The 2CoDI was found to have 0.58 wt% carbon, and 2CoCA had 4.26 wt% carbon. This is initially an unexpected result since CA prepared catalysts showed higher activity and were stable longer. Similarly, Joo et al. found higher activity for catalysts that exhibited increased coke deposits in their study on nickel aluminates in methane dry reforming. It was suggested that amorphous carbon could cover all the active sites, whereas filamentous carbon could be grown not covering the metal surface, thus, allowing catalysts with higher amounts of coke to be more active.[93] Note that that 2CoDI deactivates faster relative to its original activity. It has been shown that certain types of carbonaceous species are required intermediates in the reaction between carbon dioxide and methane [11] and that the types of carbonaceous deposits are a function of metal particle size.[94-97] The extent of coke formation is a great indicator of the different types of active sites formed due to preparation method, CA or DI.[96, 98] The catalytic sites present on 2CoCA samples must propagate formation of non-deactivating coke deposits, while 2CoDI samples produce smaller amounts of deactivating coke deposits. Coke accumulation is the result of formation and gasification of carbonaceous deposits, thus the amount of carbon deposited depends on the relative rates of these processes.[74] The 2CoCA catalysts deactivate less quickly due to the large number of well-dispersed small particles. In other words, the formation of deactivating coke appears to be favored by the larger particles in 2CoDI. We speculate that the rapid deactivation observed for both samples (earlier for DI samples) is due to accelerated coke formation. The accelerated rate of deactivation by carbonaceous deposits is believed to

occur at a critical point where the ensemble size on the surface of the Co particles is too small to promote the carbon gasification reaction effectively. To confirm different types of carbonaceous deposits, post reaction catalysts were analyzed by XPS (Figure 2.9). The C1s spectrum was deconvoluted to reveal the types of carbonaceous species.[99]

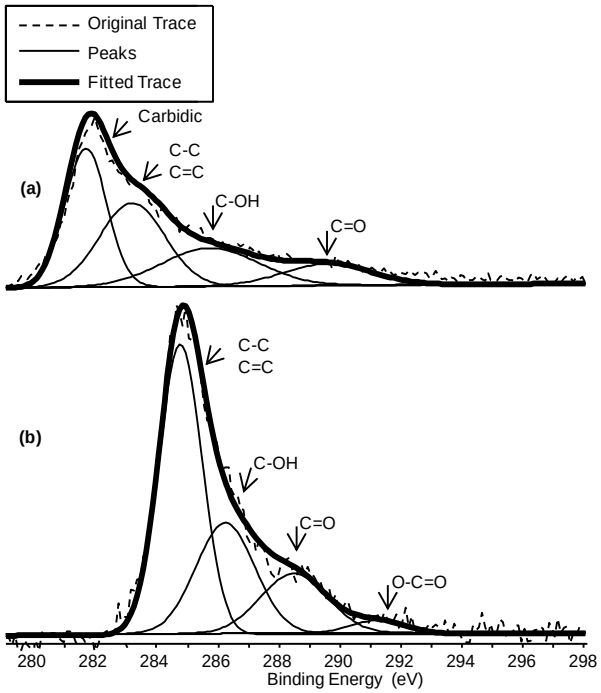

Figure 2.9 - X-ray photoelectron spectra in the C1s region of catalysts after 8 h methane dry reforming reaction (a) 2CoCA (b) 2CoDI.

For the 2CoCA sample a peak at 281.7 eV is attributed to the presence of carbidic carbon. Carbidic carbon has been shown to form on selective faces of cobalt particles.[100] Graphitic carbon can be clearly observed at 284.8 eV for 2CoDI. For 2CoCA graphitic carbon is attributed to the peak at 283.2 eV. Bulk cobalt carbide has been found to decompose to form graphitic carbon above 427 °C and is thought to cause the observed shift in binding energy for the 2CoCA.[100] In addition, peaks with higher

binding energies were observed, which are attributed to oxidized carbon species. The 2CoCA sample contained carbidic, graphitic, and oxidic carbon in a ratio of 1:1:1, while the 2CoDI sample contained graphitic, and oxidic carbon in a ratio of 1:1. The formation of different types of carbonaceous deposits is attributed to the presence of different sites that resulted from the different preparation methods.

As can be seen from this work, monometallic cobalt catalysts have decent activity but suffer from deactivation due to coking under the conditions examined. Coke deposition was significant and likely the major cause of catalyst deactivation. As many studies have indicated, Ni-Co bimetallic catalysts could be very promising for carbon dioxide reforming of methane.[3, 74] In the case of Ni-Co bimetallics coke formation was found to be lower than in either monometallic Ni or Co.[74] Ni-Co bimetallics can also provide an H_2/CO greater than unity which is desirable for many industrial processes. It will be a promising approach to optimize metal particle size, composition, and uniformity of Ni-Co bimetallic catalysts for methane dry reforming using rational synthesis methods. By preparing these catalysts using rational synthesis methods, e.g. SEA/EDF well defined materials could be prepared which would aid in understanding of the coking mechanism that is likely causing catalyst deactivation in methane dry reforming.

2.4 Conclusions

Cobalt catalysts supported on γ-Al_2O_3 were prepared by two methods, controlled adsorption and dry impregnation. Deposition of Co^{2+} can be described by the kinetic equation suggested by Lycourghitis et al. indicating that two cobalt ions (presumably as a cobalt dimer) are involved in adsorption.[58] Controlling adsorption results in catalysts

with smaller particle sizes and higher dispersion relative to the dry impregnation method studied. Adsorption of Co^{2+} on the Al_2O_3 surface likely involves mostly specific chemical interactions. Characterization results indicate that the types of active sites present on a catalyst surface strongly depend on preparation method. TPR results indicated that 2CoCA catalysts were reduced to metallic Co to a greater extent than the 2CoDI samples. Additionally, more $CoAl_2O_4$ spinel type species were found to have formed for 2CoCA catalysts. Methane dry reforming studies indicate that cobalt alumina catalysts deactivate over the 8 h reaction time studied. However, 2CoCA catalysts show higher methane and carbon dioxide conversion, which is attributed to the higher dispersion of Co. The 2CoCA catalyst was found to produce higher amounts of non-deactivating coke deposits while the 2CoDI sample formed small amounts of deactivating coke deposits that drastically hindered catalyst activity and led to faster deactivation. The presence of two types of carbon deposition dependent on preparation method was confirmed by the use of XPS.

CHAPTER 3

Effect of Metal Support Interactions in Ni/Al_2O_3 Catalysts with Low Metal Loading for Methane Dry Reforming

3.1 Background

Syngas is an extremely important commodity in the petroleum and chemical industry.[1] Methane steam reforming is the most common industrial route for the production of syngas. However, it provides limited yields of CO typically resulting in H_2/CO ratios between 3 - 16,[48] which are unsuitable for the production of fuels and chemicals by Fischer-Tropsch and methanol synthesis.[1] The production of syngas by methane dry reforming has attracted much attention for several reasons: the increased interest in the effective utilization of the greenhouse gas carbon dioxide, a possible way to utilize methane and carbon dioxide resulting from anaerobic digestion of biomass, and syngas production with a hydrogen to carbon monoxide ratio near one.[2, 3]

Nickel catalysts supported on γ-Al_2O_3 have been shown to be effective for methane dry reforming, steam reforming of methane and heavy hydrocarbons, hydrogenation reactions, hydrogenolysis, and amination reactions.[4, 7, 18] The exact nature of nickel species on the γ-Al_2O_3 surface affects the activity and selectivity during methane dry reforming, and identification of the different types of nickel species has been the focus of numerous studies.[48, 64, 66, 77, 78, 95, 101-116]

The nature of nickel species will depend on the preparation method,[78, 103, 106, 108, 111] the weight loading,[64, 77, 103, 108, 109, 111, 112] the morphology of the support,[101, 105, 107, 110, 111] and the calcination temperature.[66, 77, 78, 105, 107, 109] Additionally, the speciation of nickel can change during the reduction of the catalyst or upon exposure to reaction conditions.

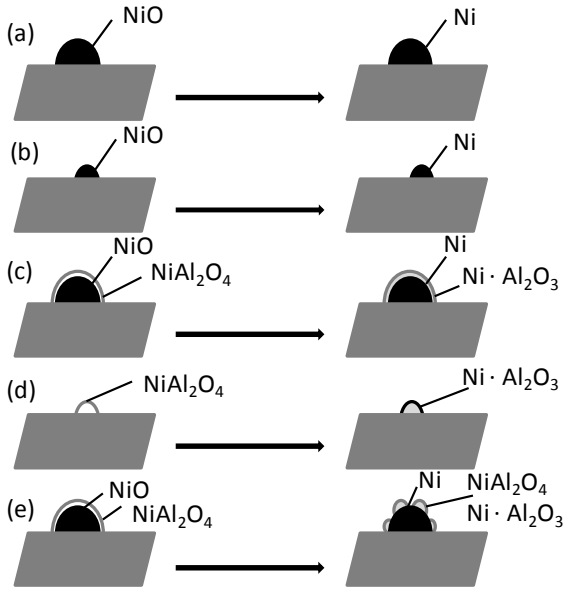

Figure 3.1 – Proposed models for the nickel-alumina structure after calcination (left) and after reduction (right). (a) large free NiO particles[111] (b) small free NiO particles[111] (c) large $NiAl_2O_4$ (fixed NiO) particles [111] (d) small $NiAl_2O_4$ (fixed NiO) particles[111] (e) alternative picture for the structure of large $NiAl_2O_4$ (fixed NiO) particles after reduction. [109]

Several of the commonly proposed nickel surface species are shown in Figure 3.1. Zielenski studied NiO/Al_2O_3 prepared by impregnation and found that NiO exists in two forms, free (Figure 3.1 a,b) and fixed (Figure 3.1 c,d).[111] Free refers to nickel that exists on the catalyst surface as nickel oxide. The occurrence of fixed nickel oxide is related to a chemical reaction between alumina and nickel oxide forming stoichiometric

and non-stoichiometric nickel aluminate ($NiAl_2O_4$). It was proposed that at oxidation above 500 °C NiO particles are covered by $NiAl_2O_4$ and in the case of small fixed NiO particles, nickel forms surface $NiAl_2O_4$ (Figure 3.1c,d respectively).[111] Lamber et al. studied nickel alumina catalysts prepared by impregnation and coprecipitation.[105, 117] TEM studies showed that after reduction in hydrogen, metallic nickel crystallites were covered by porous aluminate shells (Figure 3.1e). In the case of coprecipitated catalysts used in Lambers' study, it was said that the high stability to sintering was due to $NiAl_2O_4$ covering fixed NiO particles, in agreement with the results of Zielenski.[111, 117] Salgagre also found for nickel alumina catalysts prepared by impregnation that catalytically active nickel existed either as naked crystallites or as encapsulated nickel inside porous non-stoichiometric aluminate shells.[109]

Supported metal catalysts with low weight loading of the metal component have the desirable combination of effective metal utilization and reduced formation of carbonaceous deposits.[89] Nickel supported on alumina is reported to have higher activity than nickel supported on other oxides, and this is an indication that metal support interactions crucially influence the catalytic performance of nickel catalysts.[18] However, one of the main problems with Ni/Al_2O_3 catalysts with low nickel content is the formation of supposedly inactive nickel aluminate. In the literature, several common critical points with regards to the types of nickel species present on the alumina surface were identified: Oxidation at 500 °C was said to form stoichiometric and nonstoichiometric nickel aluminates,[105] and nickel loadings below 1 wt% were said to produce only surface $NiAl_2O_4$.[103, 112] In case of slightly higher weight loading (such as 2 wt%), different types of active sites ($NiAl_2O_4$ and NiO) are expected to be present.

To gain insight into the types and catalytic performance of nickel sites as a function of the preparation method, samples are prepared by two methods in this study: controlled adsorption and dry impregnation. Synthesis of a nickel catalyst by controlled adsorption of Ni^{2+} was inspired by the rational synthesis method strong electrostatic adsorption (SEA).[31, 32, 118] In SEA, the surface charge of the metal oxide support is exploited to maximize metal-support interactions. The point of zero charge (PZC) of a metal oxide support is the point at which the support surface is neutrally charged. At pH values above the PZC of the metal oxide, the surface is deprotonated (negatively charged), and cationic species can be electrostatically adsorbed. At pH values below the PZC, the surface is protonated (positively charged), and anionic species can be electrostatically adsorbed. In this study, nickel nitrate (Ni^{2+}) is used as metal precursor. Therefore, alkaline conditions are used to adsorb the metal cations on the support. In the case of dry impregnation, the pores of the support are filled with a volume of aqueous precursor solution that is equal to the pore volume, and deposition of Ni^{2+} on the surface occurs during drying and calcination.[26] Nickel catalysts of 2wt% Ni are prepared, and the samples are calcined at 500 °C to explore the possibility of the formation of nickel oxide and stoichiometric/non-stoichiometric nickel aluminates. By varying only the preparation method between the two samples, valuable insight is gained on the types of active nickel sites present on nickel catalysts as a function of metal support interactions during the synthesis. Calcined catalyst samples are characterized by N_2 physisorption, elemental analysis, H_2 chemisorption, TPR, TEM/ETEM, and methane dry reforming reactivity studies. Methane dry reforming is carried out at 700 °C using a stoichiometric

feed of methane and carbon dioxide for 9 h. Spent catalysts are characterized by combustion analysis and XPS.

3.2 Materials and Methods

3.2.1 Materials

Aluminum oxide, γ-phase, 99.97% metals basis from Alpha Aesar (surface area 80 – 120m^2/g) and $Ni(NO_3)_2$ (99.999% trace metals basis) from Aldrich were used as received. HCl and NH_4OH (A.C.S. reagent grade) from Sigma were used as pH adjustors in pH precipitation studies, adsorption isotherms, and catalyst synthesis. Deionized water was used throughout this study. Methane (U.H.P.) and Carbon Dioxide (Research Grade) utilized in reactivity studies were obtained from Airgas and used without further purification.

3.2.2 Controlled Adsorption (CA) Synthesis Optimization

3.2.2.1 Point of Zero Charge (PZC)

To determine the point of zero charge (PZC) of the γ–Al_2O_3 support, aqueous solutions with pH values ranging from 0.5 to 13 were prepared using HCl or NH_4OH. Alumina was contacted with the solutions using a mass of alumina that corresponded to a surface loading (S.L.) of 1000 m^2/L. The solutions were then shaken for one hour, and the final pH was then measured. A glass bodied Thermo Scientific Orion pH probe (9102BNWP) was employed for all pH measurements. The pH meter was calibrated using standard buffer solutions at the beginning of every experiment. The experiments were conducted using 50 mL polypropylene bottles at room temperature.

3.2.2.2 pH Precipitation Studies

Aqueous solutions with pH values ranging from 5.5 to 13 were prepared using NH_4OH at room temperature where 5.5 is the pH of laboratory deionized water. For each measurement, 200 ppm nickel (as nickel nitrate hexahydrate) was added to the solutions. The solutions were shaken for one hour, and the final pH was determined. Any sign of bulk precipitation (and its color) at a given pH value was noted.

3.2.2.3 Precursor Adsorption as a Function pH

Solutions with pH values ranging from 5.5 to 13 were prepared using NH_4OH. $Ni(NO_3)_2$ was dissolved in water to obtain a solution with a concentration of 200 ppm. The solution was allowed to equilibrate for one hour. The pH of the resulting solutions was then re-adjusted to its desired value, and the support was contacted at a surface loading of 1000 m^2/L for 40 mL of total solution. Before contact with the support, a 2 mL sample was taken and filtered using 0.45 μm nylon syringe filters. $Ni(NO_3)_2$ and the support were shaken for one hour. A 4 mL sample was taken and filtered. A sample was also taken after 24 hours of shaking. The filtered samples were diluted and analyzed for Ni^{2+} and Al^{3+} by ICP-OES (Perkin Elmer Optima 3000 DV). Negligible deposition occurred between the 1 and 24 h time points. The aluminum concentration was found to be lower than 10 ppm in all experiments.

3.2.3 Catalyst Preparation

3.2.2.4 Controlled Adsorption (CA)

For catalysts prepared by CA, the desired amount of precursor was added to a solution, allowed to age, and the pH was adjusted to the value that corresponds to maximum adsorption. From pH- precipitation and adsorption isotherm measurements

(*vide infra*) the optimum synthesis pH was found to be at a pH of 9.5 using NH_4OH. The metal solution was allowed to equilibrate for 1h at a pH of 9.5 and then re-adjusted to the desired value. The support was then contacted with the solution and shaken for 1 hour. The catalyst was filtered and washed twice with deionized water. Samples were taken and analyzed by ICP before and after contact with the support to ensure complete deposition had been attained. The 2 wt% Ni/Al_2O_3 catalyst prepared in this manner will henceforth be designated 2NiCA.

3.2.2.5 Dry Impregnation (DI)

The weight loading for catalysts prepared by dry impregnation was chosen to be the same as the 2NiCA catalyst. The desired amount of complex was dissolved in a volume of water that corresponded to the pore volume of the support as determined by nitrogen physisorption. The precursor solution was added to the support and stirred for 1 h at room temperature. The 2 wt% Ni/Al_2O_3 catalysts prepared in this manner will henceforth be designated 2NiDI.

3.2.2.6 Calcination

Precursor loaded supports were dried briefly in an oven at 110 °C prior to calcination. 2NiCA and 2NiDI samples were heated to 500 °C at a heating rate of 5 °C/min and held for 3 h. Zero air generated using a zero air generator (VWR, 26000-020) produced UHP air with a purity level below 0.05 ppm total hydrocarbon content from the compressed air supply.

3.2.4 Characterization

3.2.4.1 Nitrogen Physisorption

Prior to N_2 physisorption, the samples were outgassed for 3 h under vacuum at 300 °C. N_2 adsorption/desorption isotherms at -196 °C were measured for calcined catalysts using Micromeritics ASAP 2020 and approximately 0.5 g of sample. The surface area was calculated using the BET method.[119] Typically, application of the BET equation to the N_2 physisorption results produces surface area measurements within 3%.

3.2.4.2 Elemental Analysis

The nickel content was determined externally by Galbraith laboratories for the 2NiDI and 2NiCA samples. HF digestion was used to ensure the support was dissolved completely before analysis by ICP-OES.

3.2.4.2 Temperature Programmed Reduction

Temperature programmed reduction was carried out using Micromeritics ASAP 2920 equipped with a TCD detector, a reference chamber, and a cold trap. The cold trap contained a mixture of dry ice and isopropyl alcohol and ensured water did not affect the TCD signal. The concentration of the reducing gas was a 10% H_2/Ar. A flowrate of 50 mL/min and approximately 45 mg of catalyst was used in all experiments. The temperature was ramped from 25 °C to 1000 °C at 5 °C/min. In a modified TPR experiment the 2NiCA sample was pretreated at 700 °C (with a heating rate of 5 °C/min) in helium for 30 minutes. The sample was then cooled to 40 °C, and the TPR experiment was performed as described above.

3.2.4.3 H_2 Chemisorption

Metal dispersion was analyzed by hydrogen chemisorption using a Micromeritics Chemisorb 2750. Each experiment was performed with approximately 0.4 g of catalyst. The sample was first evacuated at 110 °C for 60 min to remove ambient gases. The temperature was ramped from 110 °C to 600 °C at 2 °C/min and held at 600 °C for 8 h. The sample was then cooled to 550 °C and evacuated for 16 h to remove residual hydrogen. Finally, the sample was cooled to 25 °C, and H_2 gas was dosed in order to perform the chemisorptions analysis. Two isotherm measurements were performed and the metal surface area was calculated using H/M ratio of 1.[66]

3.2.4.4 Scanning Transmission Electron Microscopy

Scanning Transmission electron microscopy (STEM) was performed with a FEI Titan 80-300 operated at 300 kV and equipped with CEOS GmbH double-hexapole aberration corrector for the probe forming lens, allowing formation of sub Ångstrom probe. The images were recorded on a High Angle Annular Dark Field detector with a detection angle that is 3 times higher than the convergence angle. The samples for TEM observations were prepared by dispersing a dry powder on a lacey-carbon coated 200 mesh Cu TEM grids, and the as prepared grids were immediately loaded into the TEM airlock to minimize exposure to atmospheric O_2.

3.2.4.5 Environmental Transmission Electron Microscopy

The in-situ microscopic observations were performed with an aberration corrected Environmental Titan 80-300. The microscope is equipped with CEOS aberration corrector for the image-forming lens, which allows imaging with sub-Ångstrom resolution. The images presented in this work were acquired with Gatan's Ultra-Scan 1000S CCD camera (2048x2048), and the acquisition was performed in Digital

Micrograph (DM). The gas flow entering the ETEM was controlled with a custom-built gas control unit, which utilizes Alicat^{R} Mass Flow Controllers (MFC) to control the composition of the gasses. Heating of the TEM samples was done with MEMS (micro-electro-mechanical systems) Aduro Protochips heating holder. Each heating chip consists of thin SiN membrane that is resistively heated based on factory calibrations. The heating currents were calibrated for vacuum conditions, and it should be noted that in the ETEM due to presence of gasses, the actual temperature is expected to be lower than the set point due to the cooling capacity of the gases.

3.2.4.6 X-ray Photoelectron Spectroscopy

XPS was performed on spent catalysts using a Thermo K-Alpa instrument. The instrument is equipped with a monochromatic small-spot X-ray source and a 180° double focusing hemispherical analyzer with a 128-channel detector. Spectra were obtained using an aluminum anode Al Kα ($h\nu$ = 1486.6 eV). The background pressure was 4.9×10^{-8} bar and 4×10^{-7} bar argon during measurement because of the charge compensation dual beam source, which was used to prevent sample charging. Binding energies were referenced to the sample stage, which contains built in calibration standards of copper, silver, and gold.

3.2.4.7 Combustion Analysis

The C, H, and N content of spent catalysts was analyzed externally by combustion analysis at Gailbraith laboratories.

3.2.5 Reactivity Studies

Methane dry reforming reactions were performed in a quartz reactor that contained a 75 – 90 μm frit using 200 mg of catalyst. A stoichiometric mixture of

methane and carbon dioxide was employed at a space velocity of 22,000 h^{-1}. Catalyst samples were pre-reduced in-situ at 600 °C for two hours in 20% H_2/N_2. The reaction temperature was 700 °C, and the pressure was approximately 1.5 atm. Product gas was sampled at 20 minute intervals using an online Bruker 450-GC refinery gas analyzer (RGA) that is equipped with two TCD detectors and a FID. One TCD was used for analysis of permanent gas mixtures, including methane, and the FID channel was used in this study to confirm of methane concentration from the first TCD. The second TCD is used for analysis of hydrogen.

3.3 Results

3.3.1 Synthesis of 2 wt% Ni/Al_2O_3 by Controlled Adsorption (2NiCA)

Controlling the adsorption of nickel on γ-Al_2O_3 will allow for direct comparison of the effect of metal support interactions on low weight loading nickel alumina catalysts. Three experiments were performed to optimize the adsorption of nickel on γ-Al_2O_3: a point of zero charge (PZC) measurement, a pH precipitation study, and an adsorption isotherm. The PZC of the batch of alumina used in our experiments was previously found to be at a pH of approximately 7.7.[120] This means to adsorb cationic complexes the pH of the impregnating solution should be sufficiently above PZC, so that the surface can be deprotonated (negatively charged). This is problematic for adsorption of Ni^{2+}, which precipitates in alkaline solutions. To investigate the stability of the cationic complex in aqueous alkaline solutions, pH precipitation studies were conducted. It was found that the metal precursor solution shifted the pH of the mixture due to equilibration of the various types of ionic species in solution (e.g. $Ni(H_2O)_6^{2+}$, $Ni(OH)_2(s)$, and $Ni(H_2O)_{6-n}(NH_3)_n^{2+}$). This shift must be corrected before the adsorption steps of the synthesis procedure.

Additionally, in the presence of NH_4OH, Ni^{2+} was found to precipitate between initial pH values of 10 and 11. Above a pH of 11, $Ni(NO_3)_2$ reacts to soluble hexamminenickel, which is identified by its clear blue color.[70, 121] Thus, an aging step is required to equilibrate at the pH of maximum uptake before the support is added and the adsorption step is performed. Figure 3.2 shows the results of monitoring Ni^{2+} deposition as a function of pH (adsorption isotherm).

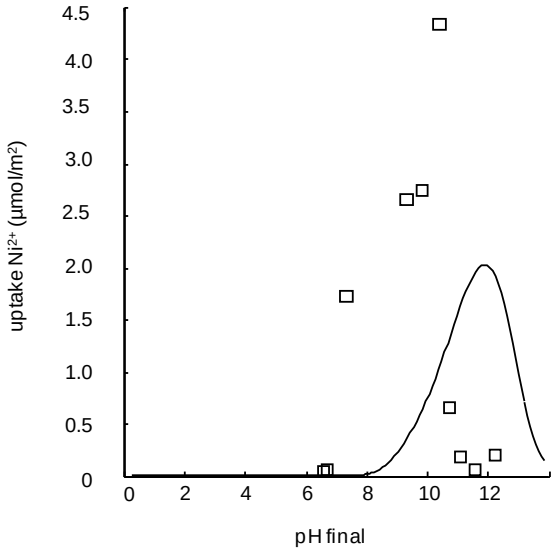

Figure 3.2 – Nickel nitrate adsorption isotherm and projected uptake based on the revised physical adsorption model. [29] Adjustable theoretical model parameters: Ns = 8 OH/nm^2, difference between pK_1 and pK_2, $\Delta pK = 5$, $r_{ion} = 0.79$ Å, one hydration sheath.[60, 68]

It was attempted to interpret the obtained data using the revised physical adsorption (RPA) model, which is well-established for SEA. [28, 29, 31-37] Briefly, the model considers only electrostatic (non-specific) interactions between the metal complex and the support to describe adsorption. Two parameters of the model are adjustable: the total number of charged sites N_s and the difference between pK_1 and pK_2 (ΔpK). For

alumina, these values can be readily found in literature: N_s = 8 OH/nm^2 and ΔpK = 5.[60, 68] The RPA model predicts maximum adsorption to occur in the final pH range of 11.5 to 12.5. However, as previously mentioned, above pH 11, Ni^{2+} forms $Ni(NH_3)_6^{2+}$ which is not accounted for by the RPA model. In addition, it is likely that multiple species in various concentrations exist at the different pH values examined (in an aqueous NH_4OH solution): $Ni(H_2O)_6^{2+}$, $Ni(OH)_2$(s), and $Ni(H_2O)_{6-n}(NH_3)_n^{2+}$. [122] It has been proposed that certain aquo metal ions (e.g. Pb^{2+}, Co^{2+}, Ni^{2+}) can efficiently penetrate the structured water layers adjacent to the surface and specifically interact with the support surface,[71] while ammine complexes were found to not specifically adsorb.[61] From Figure 3.2, it was also observed that non-negligible deposition of nickel occurs near the PZC of γ-Al_2O_3, which also indicates that chemical interactions as well as electrostatic interactions are responsible for the adsorption.[56] The failure of the RPA model to describe adsorption data and the existence of multiple types of nickel species in solution in the presence of NH_4OH indicates that chemical and electrostatic interactions are involved in adsorption of Ni^{2+} on alumina. As a result of the PZC measurements, determination of ranges of bulk precipitation, known solubility limits of alumina,[123] and adsorption isotherm measurements the optimal starting point for the synthesis of 2NiCA was determined to be at an initial pH of 9.5. This value is sufficiently above the PZC of alumina while avoiding bulk precipitation and maximizing adsorption.

3.3.2 Characterization of 2wt% Ni/Al_2O_3 catalysts prepared by CA and DI

3.3.2.1 N_2 physisorption, Elemental Analysis, H_2 chemisorption, TEM, ETEM, and TPR

Table 3.1 shows the results from elemental analysis, N_2 physisorption, and H_2 chemisorption measurements. From elemental analysis, it was found that 2NiCA

contained 1.90 wt% nickel and 2NiDI contained 1.98 wt% nickel, respectively. N_2 physisorption was performed on uncalcined, calcined, and reduced samples as well as catalysts after reaction. A small decrease in surface area (relative to fresh alumina) was observed for the uncalcined samples due to the addition of nickel nitrate. Upon calcination, 2NiCA loses 9% of its surface area while 2NiDI loses 30% of its surface area. Catalysts that were reduced at 600 °C for 2 h and subsequently utilized in methane dry reforming at 700 °C for 9 h (post reaction catalysts) both lost an additional 20% of their surface area. Samples that were utilized in TPR experiments were also analyzed by N_2 physisorption. Upon reduction at 1000 °C both samples had a surface area of 55 m^2/g, regardless of the preparation method. Further, the pore volume and the average diameter increased upon precursor deposition and calcination and then decreased when exposed to temperatures greater than 500 °C. H_2 chemisorption measurements found dispersions of 12.07% for 2NiCA and 0.26% for 2NiDI.

Table 3.1 – Results from N_2 physisorption, elemental analysis, and H_2 chemisorption of catalysts in different stages of synthesis and after reaction.

Sample	**Surface Area (m^2/g)[a]**	**Pore Volume (cm^3/g)[b]**	**Average Pore Diameter (nm)[c]**	**Elemental Analysis (wt% Ni)[d]**	**Dispersion (%)[f]**
Fresh Alumina	102	0.30	12.1	-	-
Uncalcined 2NiCA	92	0.34	15.0	-	-
Uncalcined 2NiDI	96	0.33	14.0	-	-
Calcined 2NiCA	84	0.37	17.4	1.90	12.07
Calcined 2NiDI	74	0.36	19.6	1.98	0.26
Reacted 2NiCA*	68	0.36	20.9	-	-
Reacted 2NiDI*	60	0.28	18.6	-	-
Reduced 2NiCA**	55	0.29	20.7	-	-
Reduced 2NiDI**	55	0.35	24.9	-	-

[a] Calculated from N_2 physisorption data using the BET equation
[b] Calculated from N_2 physisorption data using single point adsorption at $P/P_0 = 0.99$
[c] Calculated from N_2 physisorption data using 4V/A from BET
[d] Elemental analysis determined using ICP
[e] Average nickel crystallite size calculated using H_2 chemisorption data
[f] Nickel dispersion calculated using H_2 chemisorption data
[*] Samples reduced at 600 °C for 2 hours prior to 6 h methane dry reforming experiment at 700 °C, 9.5h
[**] Samples from TPR, reduced at 5 °C/min to 1000 °C

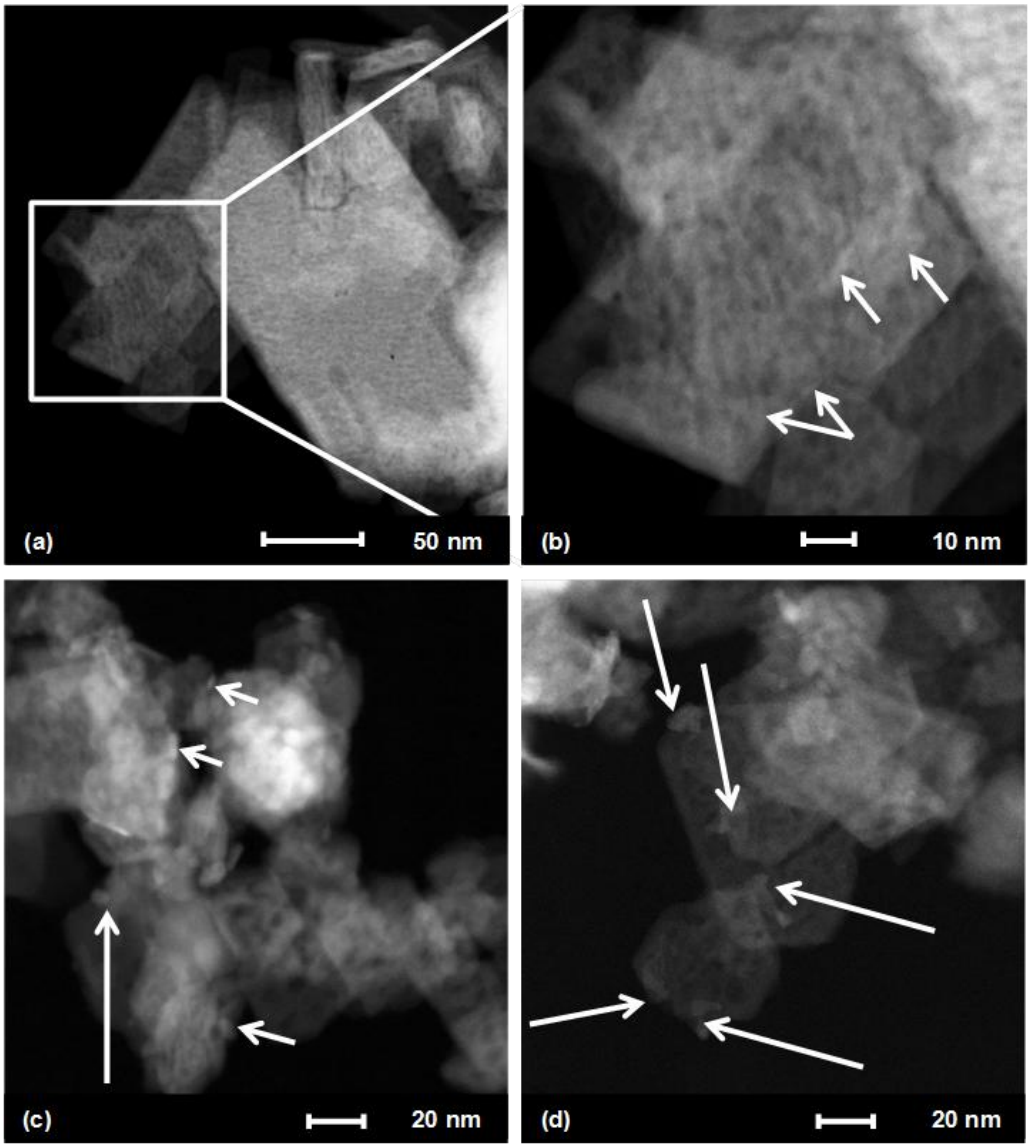

Figure 3.3 - TEM images (a,b) 2NiDI (c,d) 2NiCA. Arrows point at Ni particles as confirmed by EDS.

TEM images were collected for calcined samples (Figure 3.3). For 2NiDI, the majority of the TEM images do not clearly reveal any distinguishable particles of Ni containing phases (Figure 3.3a), and nickel is present on the surface as a very thin layer as indicated by the arrows in Figure 3.3b. In only one of many collected images for 2NiDI, a NiO particle was observed. The nickel atoms in 2NiDI are suggested to be

present close to the surface in the form of a surface nickel aluminate phase, which has been shown to exhibit weaker contrast as compared to nickel or nickel oxide.[105] For 2NiCA, distinguishable nanoparticles present on the surfaces of γ-Al_2O_3 were identified (Figure 3.3c,d). Based on high resolution imaging, several of these nanoparticles could be unambiguously identified as $NiAl_2O_4$, while in some other cases lattice spacing analysis points towards NiO. In addition to the presence of NiO and $NiAl_2O_4$ nanoparticles, highly dispersed surface nickel aluminate is present on the surface of γ-Al_2O_3. For 2NiCA, an average particle size roughly corresponding to that estimated from H_2 chemisorption measurements (~8 nm) and nickel oxide particles of very similar size and shape were observed in TEM.

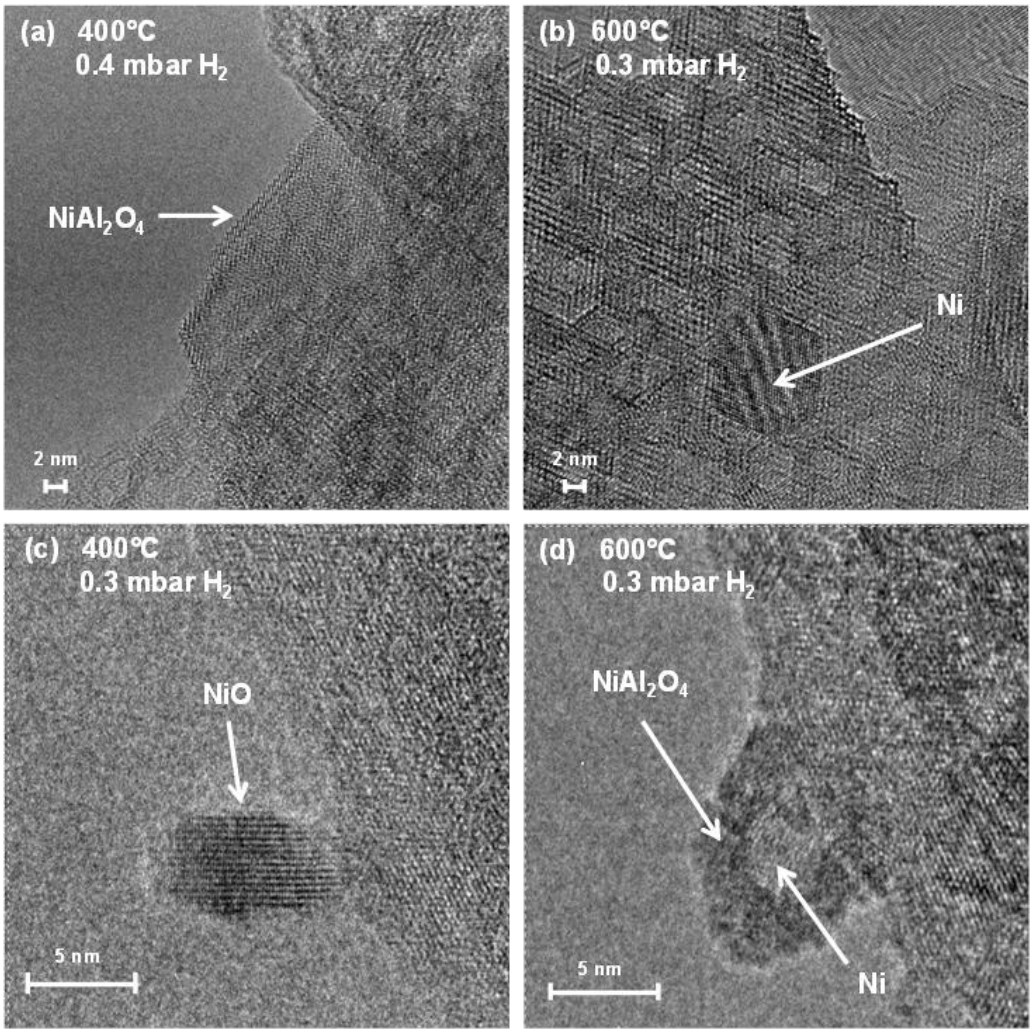

Figure 3.4 – HRTEM after exposure to the noted temperature and P(H_2) for 30 minutes of 2NiDI (a,b) and 2NiCA (c,d).

Environmental TEM images were obtained for samples exposed to hydrogen at approximate temperatures of 400 and 600 °C to probe the evolution of nickel species during the transition from an oxidized to a reduced state. As with the TEM images obtained after treatment under standard conditions, imaging the 2NiDI sample was extremely difficult due to the weak contrast between $NiAl_2O_4$ and Al_2O_3. However, a $NiAl_2O_4$ phase was observed at a temperature of 400 °C in the presence of hydrogen (Figure 3.4a). Upon exposure to H_2 at 600°C for 30 minutes, a few moderately sized Ni

crystallites (8-10 nm) were observed in 2NiDI (Figure 3.4b). The particle is likely located on one of the facets of Al_2O_3. Based on the analysis of the lattice fringes, we find that it is epitaxially attached. There is no contrast, which would indicate a presence of encapsulating shell.

In the case of 2NiCA, it was possible to track a single nickel/nickel oxide particle as it was exposed to increasing temperature in the presence of hydrogen. At room temperature and after exposure to H_2 at 400 °C for 30 minutes, the NiO particle had a lamellar structure (Figure 3.4c). However, once the temperature was increased to 600 °C for 30 minutes, a core shell structure was formed (Figure 3.4d). Lattice measurements indicate the formation of metallic nickel within a porous $NiO/NiAl_2O_4$ shell. Upon exposure to 0.3 mbar H_2 for 30 minutes at 700 °C, all particles imaged had this core shell structure (Figure 3.5 a,b). The $NiO/NiAl_2O_4$ overlayer was approximately 2 nm thick in all imaged particles. After exposure to oxygen at 700 °C and prolonged exposure to air at room temperature a hollow core-shell particle was formed (Figure 3.5 c,d).

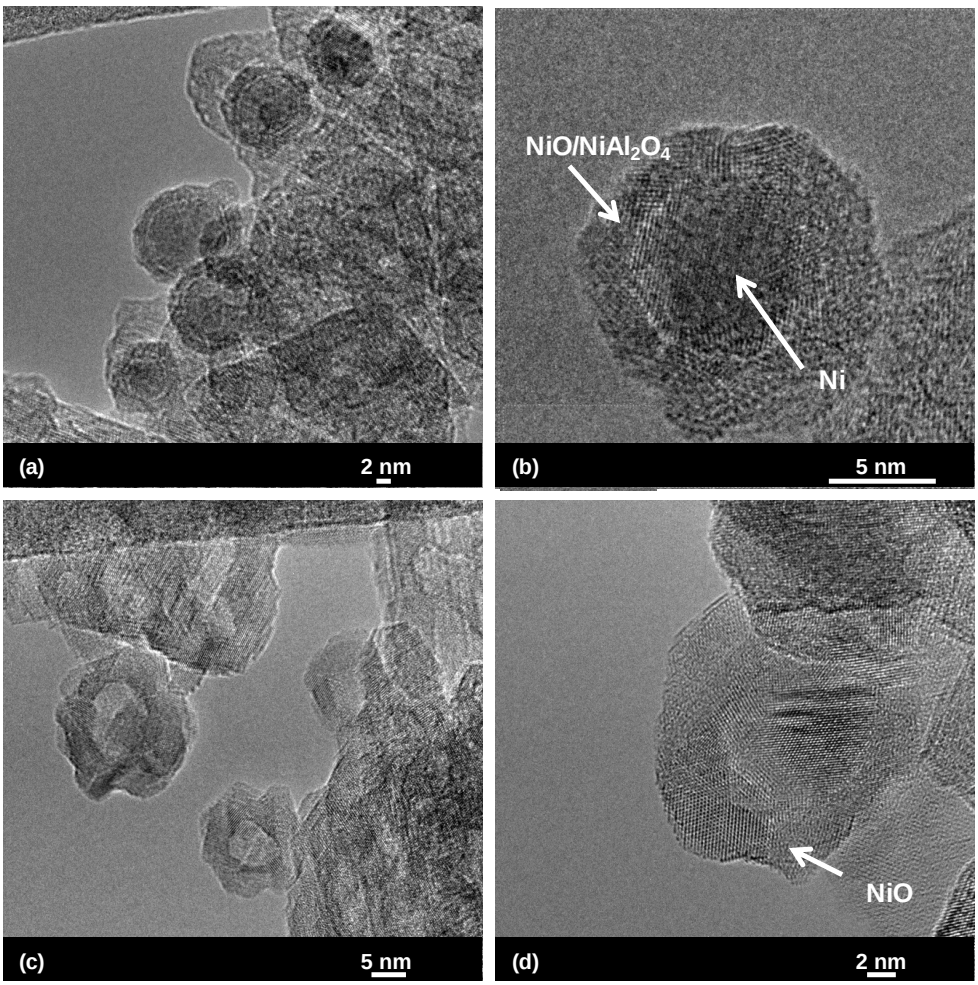

Figure 3.5 – ETEM of 2NiCA (a,b) after exposure to 0.3 mbar H_2 for 30 minutes at 700 °C (c, d) after previous exposure to H_2 at 700 °C and extend exposure to air at room temperature.

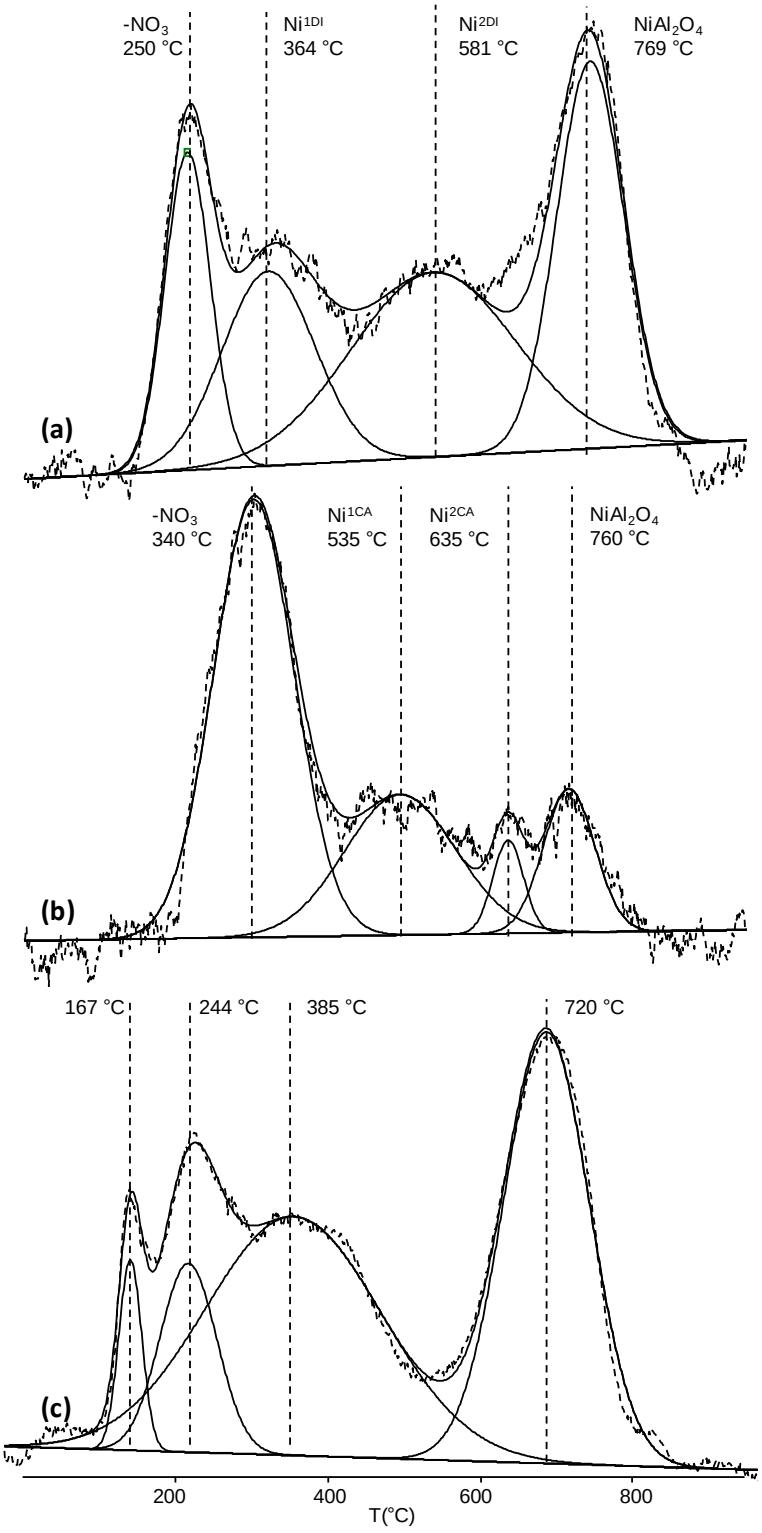

Figure 3.6 - TPR profiles of (a) 2NiDI and (b) 2NiCA (c) NiCA pretreated in He at 700 °C.

Table 3.2 – Hydrogen consumption per gram of sample for different TPR peaks based on TCD signal.

Peak Assignment	**-NO_3** [a]	**Ni^1**	**Ni^2**	**$NiAl_2O_4$**	**Fraction Reduced (%)**
2NiDI μmolH_2/ g_{cat}	N/D	124	208	179	75
2NiCA μmolH_2/ g_{cat}	N/D	78	14	36	19
2NiCA μmolH_2/ g_{cat} pretreated in He at 700 °C	N/D	N/D	254	224	70

[a] Hydrogen consumption omitted due to volatilization of nitrate species that affect TCD response

Figure 3.6 shows the temperature programmed reduction (TPR) profiles obtained for the calcined catalysts, and Table 3.2 shows the hydrogen consumption of each of the peaks normalized by the mass of catalyst used in the experiment. For the typical TPR experiments (Figure 3.6a,b), four peaks were deconvoluted from the traces obtained from TPR experiments. The first peak for both samples was attributed to decomposition of residual nitrate.[77, 78] Unsupported $Ni(NO_3)_2 \cdot 6H_2O$ is said to decompose at temperatures lower than 250 °C under flowing air pointing towards a stabilization of the nitrates by the support. [77, 120, 124] This was especially notable in the case of the 2NiCA sample, where the peak was shifted to a higher temperature than the 2NiDI sample. For the first peak, desorption of species other than H_2 is expected (e.g. NO_2, NO, N_2O_5, NH_3, etc.), and, thus, the values of H_2 consumption are omitted because their contribution to the TCD signal cannot be quantified. Additionally, comparison of the relative quantities desorbed between 2NiCA and 2NiDI is not valid because the combination of NO_x gases evolved may be different and cannot be determined with the

current experimental set-up. The total hydrogen consumption (excluding the first peak) from TPR corresponds to a total extent of reduction of 75% for 2NiDI and 19% for 2NiCA. For both samples, three distinct peaks were observed between 300 and 800 °C, which are attributed to different types of nickel species on the alumina surface. The first peak in this region will be designated as Ni^{1*} and the second as Ni^{2*} where the * will designate the preparation method, CA or DI. For 2NiDI prepared samples, Ni^{1DI} and Ni^{2DI} appeared at 364 and 581 °C, respectively. For 2NiCA prepared samples, Ni^{1CA} and Ni^{2CA} appear at 535 and 635 °C, respectively. The 4^{th} peak was observed at 769 °C and 760 °C for 2NiDI and 2NiCA, respectively.

To determine if the extent of reduction could be increased for the 2NiCA sample, the sample was pretreated at 700 °C in helium and cooled prior to the TPR experiment (Figure 3.6c). Four peaks were observed. Due to the low temperature of the first two peaks (167 °C and 244 °C) it is likely that both of these peaks are due to decomposition of residual nitrates as observed in the case of the other samples. The pretreatment could change the interaction of the nitrates with the support changing the types of nitrate species desorbed and resulting in the appearance of two peaks rather than one. Regardless, the contribution of the first two peaks to the total hydrogen consumption is small. Two peaks attributed to the reduction of nickel type species are observed at 385 °C and 720 °C and the pretreatment results in an increase of the total extent of reduction of 2NiCA to 70%. The exact assignment of these peaks requires careful consideration of different experiments reported in this study (vide infra). The final peak in the TPR profiles of all samples appeared at 720-770 °C and was assigned to the reduction of nickel present in a spinel phase.[77]

3.3.3 Reactivity Studies

The initial methane conversion was 83% for 2NiDI and 91% for 2NiCA, respectively (Figure 3.7). For 2NiCA, the methane conversion increased to 98%, while 2NiDI deactivated slightly to 80% over the 9 hours examined (Figure 3.7a). Both samples initially converted 70% of the carbon dioxide (Figure 3.7b). Over the time examined, 2NiDI deactivated to 60% carbon dioxide conversion and 2NiCA to 49%. For both catalysts, the H_2/CO ratio was less than unity indicating that the inverse water gas shift reaction contributed to the product mixture (Figure 3.7c).[125] The conversion relative to the moles of nickel present in each sample is termed specific activity (Figure 3.7d).

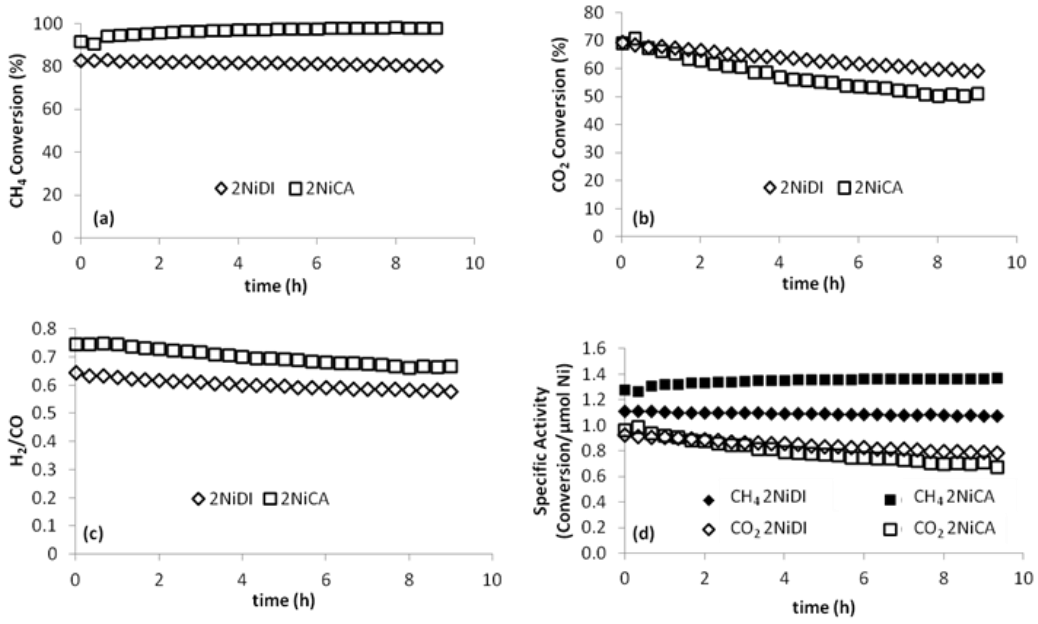

Figure 3.7 – Methane dry reforming studies using CH_4:CO_2 = 1, 700 °C, and 1.5 atm over 9.0 h. Catalysts pre-reduced at 600 °C for 2 h. (a) Conversion of methane (b) Conversion of carbon dioxide (c) Hydrogen to carbon monoxide ratio (d) Specific activity (Conversion/µmol Ni).

Combustion analysis of spent catalysts showed that 2NiCA contained 16.7 wt% carbon, whereas 3.6 wt% of carbon were found on 2NiDI. Both samples were found to have less than 0.05 wt% hydrogen and nitrogen, respectively. XPS was used to probe the different types of carbonaceous deposits (Figure 3.8). The C1s scan was performed on two different spots for each sample and the results were averaged.

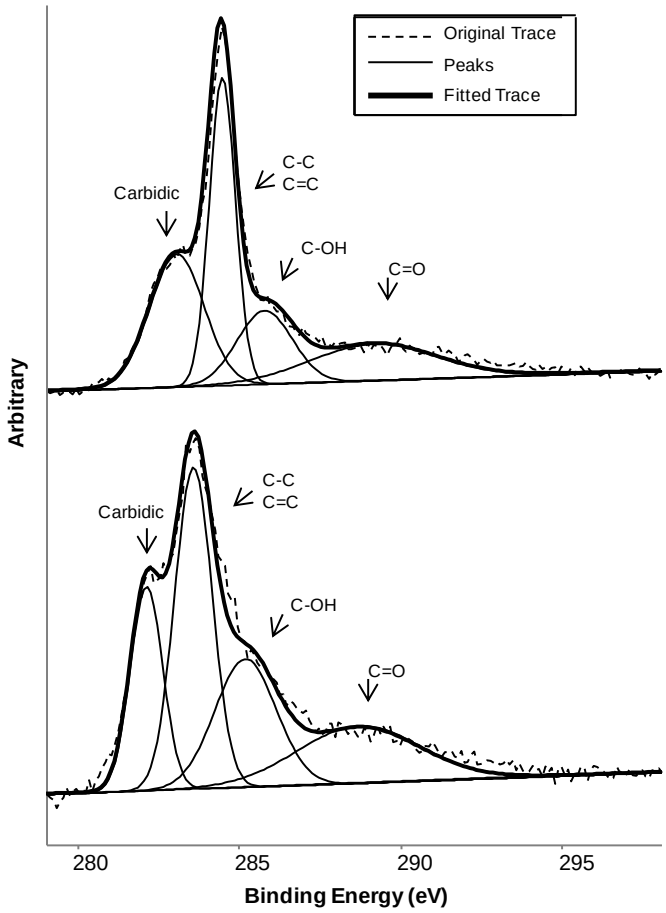

Figure 3.8 - X-ray photoelectron spectra in the C1s region of catalysts after 9 h methane dry reforming reaction (a) 2NiDI (b) 2NiCA.

The C1s spectrum was deconvoluted to reveal the types of carbonaceous species.[99] The peaks are assigned to carbidic carbon (BE 282.1 – 283.1 eV), graphitic

carbon (BE 283.6-284.5 eV), carbon present in alcohol or ether groups (285.2 – 285.8 eV), and carbon present in carbonyl groups (BE 288.7 – 289.2 eV), respectively. Carbon present as alcohol, ether, or carbonyl groups are referred to as oxidic carbon and the species were present in the same proportion in each sample. The ratios of the types of carbidic: graphitic: oxidic carbon were 0.8: 0.9: 1 for 2NiDI and 0.5: 0.8: 1 for 2NiCA.

3.4 Discussion

3.4.1 Nickel Speciation

NiO is generally considered to exist in two forms, free (Figure 3.1 a,b) and fixed (Figure 3.1 c,d).[111] Free refers to nickel that exists on the catalyst surface as nickel oxide, while fixed nickel oxide originates from a chemical reaction between alumina and nickel oxide forming stoichiometric and non-stoichiometric nickel aluminate ($NiAl_2O_4$). The assignment of nickel species present on an alumina surface derived from TPR has been discussed extensively in the literature. Scheffer et al. investigated the effect of the calcination temperature on nickel catalysts with metal contents prepared by dry impregnation.[77] For a 1.6 wt% Ni/Al_2O_3 catalyst that was calcined at 400 °C, the TPR peaks were assigned as follows: 427 – 627 °C: reduction of disperse nickel oxide interacting with the support, and between 747 – 877 °C: reduction of "a surface nickel species". The general assignment of "a surface nickel species" was used because it was thought that a calcination temperature of 400 °C was too low to form spinel species. When the calcination temperature was increased to 650 °C, the peak in the region of 747 – 877 °C became sharper and was assigned to a diluted $NiAl_2O_4$ like phase formed by diffusion of nickel ions into the support. Zhang et al. investigated the effect of the calcination temperature on nickel species. [115] In their study, the alumina support was

calcined at 600 °C prior to impregnation with nickel. For a sample with 2 wt% nickel, only one peak, at 527 °C, was observed in the temperature range of interest (25 – 727 °C), and it was attributed to reduction of surface nickel aluminate. Rynkoswki et al. examined 5 wt% Ni/Al_2O_3 prepared by dry impregnation. They observed a peak at 500 °C, which they attributed to the reduction of an amorphous overlayer of NiO, and a shoulder at 750 °C was said to be connected with the reduction of non-stoichiometric, spinel type Ni-Al oxides.[78, 102] Zielinski investigated the effect of nickel loading in Ni/Al_2O_3 prepared by impregnation followed by calcination at 400 °C.[111] For the sample with 2 wt% nickel, only one reduction peak was observed at 500 °C, and it was attributed to $NiAl_2O_4$.

Due to the significant disparity of assignments of TPR traces for nickel catalysts in literature, a combination of results from literature and complimentary experiments from the present study must be used to adequately identify the types of nickel species as a function of deposition method and thermal treatment procedure. In this context, it is important to carefully consider experimental procedures utilized in each experiment. Prior to chemisorption, the samples were reduced at 600 °C for 8 h and evacuated at 550 °C for 16 h. Then, H_2 was dosed at 25 °C to determine dispersion. Using this method, the measured dispersion was 0.26% and 12.1% for 2NiDI and 2NiCA, respectively. The low value of dispersion reported for 2NiDI is not unusual.[83, 113, 115, 126] Huang and Schwarz reported that the suppression of hydrogen uptake after high temperature reduction was due to coverage of nickel crystallites by Al_xO_y moieties, which is facilitated when adsorbed surface species are removed from nickel particles in vacuum or under inert gas.[113] Zhang et al. proposed that poor reducibility was due to diffusion of Ni^{2+} ions into the alumina lattice near the surface during spreading of Al_xO_y moieties.

Al^{3+} ions counter diffuse to the surface of NiO crystallites producing covered NiO crystallites on the surface.[115]

In the case of 2NiDI, it is speculated that weak metal support interactions allow diffusion of Ni^{2+} ions into the alumina lattice during calcination resulting in the formation of $NiAl_2O_4$ [12] . The formation of this phase occurs when Al^{3+} cations migrate from octahedral to tetrahedral sites.[127] Nickel preferentially occupies newly vacant octahedral sites in the transient alumina phase.[128] In agreement with this interpretation, studies regarding the influence of cationic additives (e.g. $Mg^{2+,}$ $Ca^{2+,}$ Ni^{2+}, etc.) on the stability of alumina found that Ni^{2+} has little or no effect on impeding the phase transformation of gamma alumina.[129] N_2 physisorption measurements indicated that the phase transformations in 2NiDI during calcination resulted in a significant loss of surface area (*ca.* 30%). TEM measurements performed after calcination further confirmed that Ni primarily exists as a surface $NiAl_2O_4$ layer. ETEM measurements revealed the presence of few free nickel particles. However, the majority of TEM and ETEM images show weak contrast indicating nickel was primarily present as a thin, disperse layer of surface $NiAl_2O_4$ after calcination and prior to TPR measurements. Consequently, the mid-range peaks in the TPR profiles of 2NiDI, Ni^{1DI} and Ni^{2DI}, are assigned to the reduction of surface $NiAl_2O_4$ (small, fixed NiO) that interacts weakly and strongly with the support, respectively. The fourth peak in the TPR profile was attributed to reduction of the $NiAl_2O_4$ in the bulk. Quantification of H_2 consumed during TPR correlates to nearly 75% reduction of the nickel present in the sample. The high extent of reduction in TPR experiments as compared to H_2 chemisorption measurements is explained by considering the differences in the experimental techniques. During TPR

measurements and in the preparation of the sample for chemisorption measurements, surface $NiAl_2O_4$ phases present in different forms on the catalyst are reduced to non-stoichiometric oxides ($Ni+Al_2O_3$).[111] In dispersion measurements, after reduction, hydrogen was pulsed onto the sample, and nickel present as $Ni+Al_2O_3$ was not available for H_2 chemisorption. We speculate that the metallic particles formed during reduction are embedded in the aluminate structure and not available for hydrogen chemisorption.[49]

The relatively high dispersion obtained for 2NiCA shows that strong metal support interactions can suppress the diffusion of Ni^{2+} into the γ-Al_2O_3 lattice at mild conditions, which has also been observed in other studies on nickel-alumina catalysts.[12, 116] Under the experimental conditions utilized in chemisorption measurements it is likely that a significant fraction of nickel exists as small, free nickel particles as indicated by the ETEM measurements. When 2NiCA is heated in H_2 at 600 °C there is a high density of core-shell particles that suddenly appear suggesting that before exposure to reducing conditions, free NiO was dispersed in higher proportion than $NiO/NiAl_2O_4$ surface layer. Upon exposure to reducing conditions at 700 °C the majority of the nickel species become covered by nickel aluminate surface layer similar to the transformation observed by Lamber et al. [105] Therefore, Ni^{1CA} in the TPR profile is attributed to reduction of small (free) NiO as indicated by the high temperature of the peak, and dispersion and ETEM results. The high temperatures of Ni^{1CA} indicated, as expected for this preparation method, that 2NiCA has strong metal support interactions. The low extent of reduction during TPR for 2NiCA can be understood by considering N_2 physisorption and ETEM results. Surface area analysis of 2NiCA after TPR

measurements (up to 1000 °C) indicated a 35% loss in surface area, which could point to an increased formation of surface nickel aluminate. The ETEM results clearly showed that at 600 °C (in the presence of hydrogen) Ni crystallites become encapsulated in a $NiO/NiAl_2O_4$ shell. Interestingly, reduced samples from ETEM measurements were re-oxidized and formed hollow core-shell structures upon exposure to oxygen at 700 °C for 30 minutes and extended exposure to air at room temperature. Formation of these hollow shell structures is consistent with the Kirkendall effect where nickel is found to diffuse faster through than oxygen through the porous $NiO/NiAl_2O_4$ overlayer,[14] providing further confirmation of a metallic core under high temperature reduction conditions. A temperature of 600 °C appears to be an approximate threshold for the transformation of Ni species in the 2NiCA sample as this was the temperature utilized for reduction before performing H_2 chemisorption, which indicated a relatively high dispersion. Thus, the low total degree of reduction obtained during TPR can be attributed to transient aluminate shell formation. This transient behavior of 2NiCA is confirmed by the modified TPR experiment where 2NiCA was heated to 700 °C in helium prior to performing the TPR. Unfortunately, it was impossible to determine if the same aluminate overlayers were formed in helium as were observed in ETEM under hydrogen due to experimental constraints of the MEMS chip. However, it is clear that the low extent of reduction obtained in the conventional TPR is the result of transient formation of nickel species at high temperatures, which is prevented when the sample is aged under inert gas. Thus, the Ni^{2CA} peak is assigned to reduction of NiO or surface $NiAl_2O_4$ layers, which strongly interact with their environment. Due to the formation of overlayers the reduction of these species remains limited unless an aging step is implemented. The fourth peak at

approximately 760 °C was attributed to reduction of the $NiAl_2O_4$ surface layer (observed in TEM).[111]

3.4.2 Catalytic Performance and Deactivation

Methane dry reforming is described by,[74]

$$CH_4 + CO_2 \leftrightarrow 2CO + 2H_2 \quad \Delta H^0_{298K} = -247 \text{ kJ/mol} \quad (1)$$

Inverse water-gas shift (2), methane steam reforming (3), and deposition of carbonaceous deposits (4, 5) are also known to occur during methane dry reforming,

$$CO_2 + H_2 \leftrightarrow 2CO + H_2O \quad \Delta H^0_{298K} = 41 \text{ kJ/mol} \quad (2)$$

$$CH_4 + H_2O \leftrightarrow CO + 3H_2 \quad \Delta H^0_{298K} = 206 \text{ kJ/mol} \quad (3)$$

$$CH_4 \rightarrow C + 2H_2 \quad \Delta H^0_{298K} = 75 \text{ kJ/mol} \quad (4)$$

$$2CO \rightarrow C + CO_2 \quad \Delta H^0_{298K} = -171 \text{ kJ/mol} \quad (5)$$

Nickel alumina catalysts have been widely investigated for the dry reforming of methane.[11] Guo et al. studied a 10 wt% Ni/Al_2O_3 catalyst prepared by wet impregnation.[130] At 750 °C the conversion of methane was 61% CH_4 and the conversion of carbon dioxide was 63%. During the 12 h study, the conversion of methane decreased to 32% and the conversion of carbon dioxide decreased to 30%. San Jose et al. studied 9 wt% Ni/Al_2O_3 prepared by wet impregnation for methane dry reforming at 700 °C and atmospheric pressure.[3] The conversion of methane was found to be 63% and decreased to 55% during the 6 h reaction period. Wang et al. examined the effect of nickel precursor on activity of 8 wt% Ni/Al_2O_3 catalysts. At 700 °C between 70-80 % of methane and carbon dioxide were converted depending on the nickel precursor used to synthesize the catalyst.[131] The 2 wt% nickel catalysts examined in this study at a

reaction temperature of 700 °C provide higher activity and slower deactivation than catalysts with much higher weight loadings. The initial methane conversion was found to be 91% for 2NiCA and that increased to 98% over the 9 hours examined. In the case of 2NiDI, an initial methane conversion of 83% was found and that decreased to 80% over the 9 hours examined. Both samples initially converted 70% of the carbon dioxide. The 2NiDI catalyst deactivated to 60% carbon dioxide conversion and 2NiCA to 49%.

One would expect that, because of the low apparent dispersion obtained from H_2 chemisorption, 2NiDI would not have performed as well in the methane dry reforming studies as was observed. Based on assignments of the types of nickel species that exist on the catalyst surface, it seems reasonable that under reaction conditions surface $NiAl_2O_4$ identified in 2NiDI must be catalytically active.[117, 132, 133] In the beginning of the reaction, 2NiCA likely contained a mixture of small, free nickel particles as well as nickel particles encapsulated by porous $NiO/NiAl_2O_4$ overlayer. The types of active sites on 2NiCA could evolve dynamically as the reaction progresses. On a specific basis, both catalysts converted similar amounts of carbon dioxide, and 2NiCA had a higher H_2/CO ratio confirming that the types of sites affect activity and selectivity of the methane dry reforming reaction favoring different reaction pathways. It was shown that different surface nickel species exhibit different catalytic behavior, such as activity and mechanism for methanation of CO.[112] The higher H_2/CO ratio for 2NiCA and the increase in methane conversion indicated that this catalyst could promote steam reforming of methane (reaction 3) more effectively than 2NiDI (Figure 3.7c). The relative rate of carbon deposition is negligible compared to the change of methane concentration indicating coking is not the primary reason for the observed increase in methane

conversion. Further, if one analyzes the conversion relative to the moles of nickel present in the sample (specific activity), it can be seen that the 2NiCA sample uses the metal present more effectively than 2NiDI (Figure 3.7d). Deactivation of these catalysts over the time period examined was minimal relative to our previous study where cobalt on alumina catalysts were studied for the methane dry reforming reaction.[120]

The quantity and types of carbonaceous deposits are explained by considering nickel speciation. Spent samples differ primarily in the amount of carbidic carbon with 2NiDI having nearly twice the amount of carbidic carbon. Aluminate species have been said to propagate the formation of carbidic carbon, explaining why there was a larger amount of that type of carbonaceous deposit in 2NiDI.[120] Further, the total amount of carbon deposited on 2NiDI is four times less than that deposited on 2NiCA indicating gasification of carbonaceous deposits is more easily accomplished on dispersed surface $NiAl_2O_4$.

3.5 Conclusions

Preparation methods drastically affect the type of nickel species present on alumina supported nickel catalyst. In the case of samples prepared by controlled adsorption (2NiCA), where the preparation method induces strong metal support interactions, the formation of nickel aluminate is reduced at mild conditions. However, once the temperature is increased beyond 600 °C the thermal energy of the system is great enough to overcome the 5 – 15 kJ/mol energy of metal-support bond,[12] and the formation of aluminates cannot be entirely avoided as indicated by physiochemical characterization results. In the case of nickel samples prepared by dry impregnation (2NiDI), H_2 chemisorption results indicated low dispersion, and considering TPR,

ETEM, and reactivity measurements, it is concluded that surface $NiAl_2O_4$ is the primary type of nickel species. The sample prepared by controlled adsorption (2NiCA) is found to have a higher dispersion from H_2 chemisorption, and the free nickel oxide particles are found to be covered by nickel aluminate surface layers at temperatures in excess of 600 °C as indicated by the decline in H_2 consumption during TPR measurements. The formation of these core shell structures is confirmed by ETEM. Low weight loading nickel alumina catalysts were found to have excellent activity and stability for methane dry reforming. The types of active sites present affect the selectivity, activity, and carbonaceous deposits of the catalysts.

Further, there is a broader implication of this work. Through careful preparation of catalysts and characterization at each step in preparation/treatment a template has been outlined to tailor types of nickel sites on γ-Al_2O_3 surface to be used in a wide range of reactions.

CHAPTER 4

Pechini Synthesis of Nickel Aluminates for Methane Dry Reforming and Methane Steam Reforming

4.1 Background

Nickel catalysts supported on γ-Al_2O_3 have been extensively used for various high temperature applications, such as hydrogenation, hydrocarbon reforming, water gas shift promotion, ammonia decomposition.[4, 7, 18, 134] One of the major challenges is the potential deactivation of these catalysts during high temperature reactions by sintering,[135, 136] carbon deposition,[135-137] or loss of active sites due to formation of $NiAl_2O_4$.[114, 138] The formation of supposedly inactive $NiAl_2O_4$ has been cited as a major mode of deactivation for supported Ni/Al_2O_3 catalysts.[66, 114, 138] Recently, bulk materials of the formula AB_2O_4/ABO_3 have regained attention for reactions such as methane steam reforming,[48, 132, 133] partial oxidation of methane,[19, 39],[139] methane dry reforming,[39, 45, 95, 136, 140, 141] oxidative coupling of methane,[42] automotive emissions control,[46, 142] oxidative ethane dehydrogenation,[143] tetradecane reforming, [144] and tar reforming.[137] Spinels of the formula AB_2O_4 are widely accepted to have a structure similar to magnetoplumbites,[128, 145, 146] while materials of the formula ABO_3 are known as perovskites.[147] While it is generally accepted that nickel aluminates have an inverse spinel structure with nickel primarily occupying octahedral sites,[38, 44, 148, 149] some studies have reported that nickel primarily occupies tetrahedral sites.[45, 89] Further, it was reported that at high temperatures the distribution of ions in the octahedral and tetrahedral sites can change[45,

148, 150] indicating mobility of nickel within the host framework. These materials are of great interest for methane steam reforming and methane dry reforming reactions due to their resistance to sintering and the reduced formation of carbonaceous deposits.[39, 128, 144] The reactivity of AB_2O_4/ABO_3 materials have been ascribed to many mechanisms: ability of individual atoms within the bulk structure to move reversibly in and out lattice,[39, 46] nanospinodal decomposition, [142, 151] reactivity of oxygen contained within the material,[19, 42, 44, 140, 143, 144, 146] formation of nanoparticles within the bulk structure framework,[45, 49, 128, 137, 138, 152] or formation of nickel oxide particles supported by the nickel aluminate structure.[141]

Several methods are commonly used to prepare mixed oxide catalysts: solid state reaction,[148] co-precipitation,[121, 132, 135, 146, 153] sol-gel method,[48, 141, 154] combustion synthesis,[45] alkoxide method,[139, 140, 142] and Pechini synthesis.[39, 40, 152] In the Pechini synthesis, metal precursors are incorporated into a polymeric resin, which is calcined in a subsequent step (Figure 4.1).[40] The method is very effective for providing uniform multicomponent oxides because the resin reduces differences in chemical reactivity of the different metal ions during the formation of the oxide. Therefore, the uniform composition is maintained when the resin gradually decomposes during calcination, and segregation of the mixed oxide is minimized.[41, 47] Another advantage of using Pechini synthesis is a much lower firing temperature is required for synthesis than that required for a solid state reaction to form the same multicomponent oxide.[149]

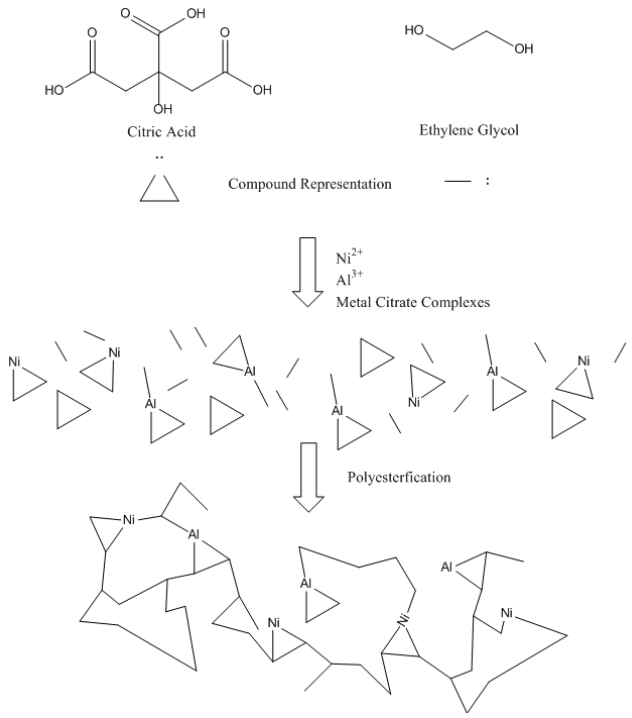

Figure 4.1 - Schematic representation of synthesis nickel aluminates by Pechini synthesis.

The present work investigates the activity and stability of nickel aluminates of three compositions prepared by Pechini synthesis. The materials, which are similar in structure to magnetoplumbites and perovskites, are thoroughly characterized using a suite of physicochemical techniques. The effect of the composition and structure of $NiAl_2O_4$, $Ni_2Al_2O_5$ and $NiAl_4O_7$ on the performance in two reactions, methane steam reforming and methane dry reforming, is examined.

4.2 Materials and Methods

4.2.1 Materials

Chemicals used in the synthesis, $Ni(NO_3)_2 \cdot 6H_2O$ (99.999% trace metals basis), ethylene glycol (spectrophotometric grade, > 99 %), citric acid (ACS reagent, 99.5% purity), were used as received from Sigma-Aldrich. $Al(NO_3)_3 \cdot 9H_2O$ (ACS grade, 98+%)

was used as received from Strem chemicals. Nickel aluminates were benchmarked against a commercial 50 wt% Ni/α-Al_2O_3 (High Fuel^{TM}) catalyst purchased from Alfa Aesar. De-ionized water was used throughout this study. Methane (UHP), Nitrogen (UHP), and CO_2 (Research Grade) were used during reactivity experiments without further purification.

4.2.2 Pechini Synthesis

Nickel aluminates were synthesized using the Pechini synthesis.[41] The metal ions were chelated with citric acid and polyesterfied with ethylene glycol forming a polymeric resin. The amount of nickel nitrate and aluminum nitrate used during synthesis was calculated from the desired final composition nickel and aluminum in the spinel structure. The metal nitrates and citric acid (citric acid: ($[Ni^{2+}] + [Al^{3+}]$)) ratio of 3:1 (molar basis) were added to 500 mL water and stirred until all components were visibly dissolved. The mixture was then heated to 70 °C and stirred for an additional 30 minutes to ensure complete mixing and dissolution of the metal citrate complexes. Ethylene glycol was then added at 60 wt% relative to the amount of citric acid used, and the mixture was slowly heated to 120 °C. All of the water was allowed to evaporate until the polymeric resin was formed. The produced resin was aged for two days prior to calcination to ensure homogeneity.

The resin was calcined using a GHSV of 33 mL air $min^{-1}g_{resin}^{-1}$. The resin was first heated to 400 °C at a ramp rate of 5 °C/min and held at 400 °C for 1 hour until all ethylene glycol was removed. The mixed metal oxide was then further heated to 1000 °C at 5 °C/min and held there for 1 h. The resulting mixed metal oxide was ground using a mortar and pestle and sieved to 75 – 90 μm for all subsequent experiments.

4.2.3 Reactivity Tests

Activity tests were carried out under atmospheric pressure in a laboratory scale vertical plug flow reactor which was operated isothermally (Lindberg Minimite furnace). Brooks mass flow controllers (model 4850) were used to supply gas feeds. Steam was generated in the setup using an ISCO syringe pump (model 500 D) which fed into a heated T-piece that utilized nitrogen as the sweep gas. Quartz beads were used in the T-piece to provide extra surface area to allow for complete volatization of the water feed. To further ensure steady flow of steam, 4 feet of heated line was installed after the T-piece to allow for additional residence time before reactants entered the reactor. An online GC (Bruker 450 RGA) was used to analyze reactor effluents. The GC was equipped with a dual TCD and an FID. One TCD was used for quantification of hydrogen while the other quantified carbon monoxide, methane, carbon dioxide, and nitrogen. The FID was used to confirm methane quantification from the TCD. Rector effluent samples were taken every 15 minutes. Thermal conversion was investigated by running reactions in an empty tube and was found to be negligible in all experiments. Rates obtained at different flow rate and particle sizes show no effect of these variables confirming mass transport effects were not present. A GHSV of 52,400 h^{-1} was employed in methane dry reforming experiments and 65,500 h^{-1} in methane steam reforming experiments (dry basis). When reduction was employed prior to reactivity tests, the samples were heated to 600 °C at 5 °C/min in 20 % H_2/ N_2 mixture and held for 2 hours before the temperature was increased to 700 °C. All reactivity tests were conducted at 700 °C for 12 h. In the case of methane dry reforming studies, the feed gas was stoichiometric carbon dioxide

and methane. For methane steam reforming studies, the feed was 20% methane with balance nitrogen, and the steam to carbon ratio was 2.4.

4.2.4 Physicochemical Characterization

4.2.4.1 Elemental Analysis

The metal content in each of the nickel aluminates was determined using inductively coupled plasma optical emission spectroscopy (ICP-OES). The ICP-OES measurements were carried out by Gailbraith laboratories.

4.2.4.2 N_2 Physisorption

N_2 physisorption measurements were carried out using a Micromeritics ASAP 2020. To minimize instrument error, approximately 1.0 g of sample was used in each measurement. Samples were outgassed at 10 Torr and 300 °C for 1 h prior to analysis. The surface area was calculated using the BET method and the pore size and volume using the BJH method applied to the desorption branch of the isotherm.[119]

4.2.4.6 TPR, TPO, and H_2 chemisorption

TPR, H_2 chemisorption experiments, and TPO experiments were carried out on a Micromeritics ASAP 2920 equipped with a cold trap and a TCD detector. Approximately 0.15 g of sample were used in each set of experiments. Three sets of experiments were performed on each sample: TPR-H_2 chemisorption, TPR- H_2 chemisorption-TPO, and TPR-H_2 chemisorption-TPO-TPR2. Further, a control experiment was conducted to determine if there was any effect on TPO measurements caused by running intermediate H_2 chemisorption experiment. The control experiment was conducted by running TPR followed directly by TPO. The intermediate H_2 chemisorption experiment was found to have no effect on TPO results. During the TPR segment of each of the experiments, the

sample was heated from 25 °C to 1000 °C (10 °C/min) in 10% H_2-Ar mixture, and hydrogen consumption was recorded. In certain experiments, H_2 chemisorption was performed after the TPR segment by cooling to 900 °C and holding it for 30 minutes in 10% H_2-Ar mixture to ensure complete reduction. The gas was then changed to pure Ar and the sample was cooled to 35 °C (10 °C/min). Pulses of hydrogen were injected using a sample loop of known volume until the sample was saturated and hydrogen peaks of equal volume were observed. In experiments where TPO was performed following H_2 chemisorption measurements, the sample was flushed under He for a minimum of 30 minutes, and the gas was subsequently changed to 10% O_2-He. The sample was ramped from 35 °C to 1000 °C (10 °C/min), held for 30 minutes, and oxygen consumption was recorded. In experiments where TPR2 was performed following TPO measurements, the sample was cooled in Ar from the final TPO temperature of 1000 °C to 35°C and held for 30 minutes. The gas was then changed to 10% H_2-Ar, and the TPR measurement as described before was repeated. In the control experiment, TPR followed directly by TPO was performed as described above.

4.2.4.6 X-ray Diffraction (XRD)

Powder XRD patterns were measured on a Philips X'pert diffractometer equipped with an X'celerator module. Cu Kα radiation was used as the source, and diffractograms were obtained from $2\theta = 10 - 90°$ with a step size of 0.0167.

In-situ XRD

In-situ XRD reduction was performed at X18a beamline at the National Synchrotron Light Source. XRD patterns were acquired with a Perkin-Elmer (PE) amorphous silicon area detector with 2048 × 2048 pixels and a 200 × 200 μm^2 pixel size.

The X-ray photon energy was set to 20 keV. Before collecting the diffractograms, the detector was calibrated using a LaB_6 standard. For each spectrum, 10 exposures of 4 s duration were recorded for both the diffraction pattern and the dark current, and the dark current was subtracted. A Clausen cell [155] which allows for the flow of hydrogen over the sample was used for acquisition of XRD data. The sample powder was loosely packed into a 1.0 mm o.d./0.9 mm i.d. quartz capillary. The capillary was connected to 1/16 inch Swagelok style fittings with Vespel ferrules. An Omega thermocouple was inserted into the capillary and placed adjacent to and contacting the catalyst bed. Plots of the 2θ data were created from the recorded XRD patterns using the Datasqueeze software developed by Paul Heiney. Collected data was converted to Cu Kα energy.

4.2.4.7 Transmission Electron Microscopy (TEM)

TEM, high angle annular dark field (HAADF) scanning transmission electron microscopy (STEM) images, and energy dispersive x-ray (EDX) spectrometry were collected using a FEI Tecnai F30 super twin field emission gun TEM. The TEM was operated at 300 kV and was equipped with a single tilt tomography holder from Fischione Instrument.[156] The samples for TEM observations were prepared by creating a powder-ethanol mixture which was added drop wise to 200 mesh copper grids with carbon film TEM grids.

4.2.4.8 X-ray Photoelectron Spectroscopy (XPS)

XPS measurements were performed on a Thermo K α XPS equipped with a monochromatic small-spot X-ray source using an aluminum anode Al Kα ($h\nu$ = 1486.6 eV). A background pressure was 4.9×10^{-8} bar and 4×10^{-7} bar argon was used during measurement to prevent sample charging. Binding energies were referenced

to the sample stage, which contains built in calibration standards of copper, silver, and gold.

4.2.4.9 X-ray Absorption Spectroscopy (XAS)

EXAFS and XANES Ni K-edge spectra were collected at beamline 9-BM-C at the Advanced Photon Source of Argonne National Laboratories in Chicago (Proposal GUP-38563). A Si(1 1 1) double monochromator was used to select the beam energy for all measurements. The beam size was 800 × 1000 μm. Samples were pressed into wafers of 3 mm diameter using a cylindrical wafer press that contains 6 slots that can accommodate samples. The beam was internally calibrated with a metallic Ni reference foil, and spectra were collected in transmission mode. A spectrum was first taken of each of the fresh samples. The samples were then reduced at 900 °C for 2 h in an external furnace. The samples were then flushed with nitrogen, cooled to room temperature, and the Ni-K edge spectra were obtained without exposing the sample to air. Reduced samples were then re-oxidized at 900 °C for 2 h in external furnace, flushed with nitrogen, cooled to room temperature, and the Ni-K edge spectra were obtained without exposing the sample to air. Next, fresh samples were heated to 700 °C in inert gas. The samples were then exposed to a stoichiometric mixture $CH_4 - CO_2$ for 1 h. The samples were then flushed with nitrogen, cooled to room temperature and the Ni-K edge spectra were obtained without exposing the sample to air.

Data was analyzed using WinXAS. A two polynomial fit was used for background correction. For the pre-edge region, a linear fit was used and for the post edge, a cubic spline. The edge energy, E_0 was identified from the inflection point in the edge, i.e., the first maximum in the first derivative of the XANES spectrum. EXAFS data

was then converted to k space using mue0fit function with 6 spinal nodes and k^2 weighting. The Fourier transform of the k^2 weighted EXAFS oscillation (Δ k = 2.7 – 10.9) converted the data from k space to r space to obtain a radial distribution function. The peak of interest was isolated using inverse Fourier transform. The data was curve fitted by standard methods using experimental phase shift and backscattering amplitudes derived from standard compounds of known structure, Ni foil (12 Ni–Ni at 2.49 Å) and NiO (6 Ni–O at 2.09 Å) or Ni foil (12 Ni-Ni at 2.49 Å). Difference spectra were created by subtracting reaction spectra from the as-is spectra.

4.3 Results

4.3.1 Physiochemical Properties of Prepared Catalysts

The nickel and aluminum concentrations in the nickel aluminate samples were determined by ICP-OES (Table 1). Stoichiometric nickel aluminate ($NiAl_2O_4$) has 33.2 wt% Ni. The elemental analysis results of prepared catalysts are listed in Table 1. To maintain charge neutrality, the sample with 20 wt % nickel will be designated $NiAl_4O_7$, the sample with 34 wt% nickel $NiAl_2O_4$, and the sample with 45 wt% nickel $Ni_2Al_2O_5$.

Table 4.1 - Characterization of nickel spinels by elemental analysis, ammonia TPD, N_2 physisorption, H_2 chemisorption, temperature programmed reduction, and temperature programmed oxidation.

Sample	**$NiAl_4O_7$**	**$NiAl_2O_4$**	**$Ni_2Al_2O_5$**
Ni content [a] (wt%)	20	34	45
Al content [a] (wt%)	36	31	20
Surface area [b] (m^2/g)	41	37	25
Pore volume [c] (cm^3/g)	0.08	0.1	0.06
Pore diameter [d] (nm)	8	14	9
TPR H_2 uptake [f] (mmol/g)	3.3	5.4	7.6
TPO O_2 uptake [g] (mmol/g)	1.5	2.1	3.0
TPR2 H_2 uptake [f] (mmol/g)	3.5	5.4	7.7
Dispersion [h] (%)	0.65	0.97	0.51

[a] Elemental analysis determined from ICP-OES at Galbraith laboratories
[b] Calculated from N_2 physisorption data using the BET equation
[c] Calculated from N_2 physisorption data using single point adsorption at $P/P_0 = 0.99$
[d] Calculated from N_2 physisorption data using 4V/A from BET
[e] Calculated from NH3 TPD data
[f] Total H_2 consumption from TPR data
[g] Total O_2 consumption from TPO data
[h] Calculated from pulse chemisorption using H/M = 1

4.3.1.1 Nitrogen Physisorption

N_2 physisorption adsorption/desorption isotherms are shown in Figure 4.2. The values of surface area, pore volume, and pore size are listed in Table 4.1. From the IUPAC classification all isotherms are type IV indicating a mesoporous solid.[119] Inspection of the isotherms revealed that $NiAl_4O_7$ showed a H2 hysteresis indicating complex pores with ill-defined shape and size. The isotherm for $NiAl_2O_4$ contained a H1 hysteresis, which is representative of a narrow distribution of uniform (cylindrical) pores.[119] The isotherm for $Ni_2Al_2O_5$ contained a H4 hysteresis, which is attributed to the presence of narrow slit like pores. The presence of less than stoichiometric amount of nickel ($NiAl_4O_7$) caused irregularities in the spinel structure. A stoichiometric amount of nickel ($NiAl_2O_4$) created an ordered, uniform spinel structure. When the nickel content was increased further ($Ni_2Al_2O_5$) the pores of the spinel structure became narrower. This might be caused by the accumulation of nickel or nickel oxide particles in void spaces of the slit like pores.

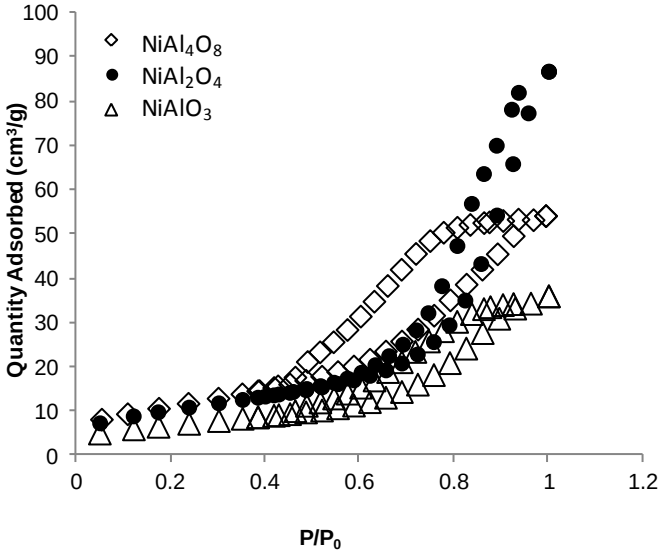

Figure 4.2 - N_2 physisorption adsorption/desorption isotherms for nickel aluminates. $Ni_2Al_2O_5$ and $NiAl_2O_4$ offset by 50 and 120 cm^3/g, respectively, for clarity.

4.3.1.2 Temperature Programmed Reduction (TPR), Hydrogen Chemisorption, and Temperature Programmed Oxidation (TPO)

$NiAl_4O_7$, $NiAl_2O_4$, and $Ni_2Al_2O_5$ exhibited high temperature reduction peaks corresponding to reduction of nickel aluminate species at 870 °C, 780 °C, and 800 °C, respectively (Figure 4.3). $NiAl_2O_4$ had a small peak at 360 °C corresponding to nickel oxide that exists on the surface of the bulk structure. $Ni_2Al_2O_5$ exhibited a large bimodal peak centered at 480 °C corresponding to the reduction of two different types of NiO that existed on the surface of bulk aluminate.[111] The area of the low temperature peak is approximately half of the total hydrogen consumed indicating a 1:1 ratio of NiO: $NiAl_2O_4$. All samples also exhibited a small shoulder at 960 °C. The values of hydrogen consumption (Table 4.1) correspond to almost complete reduction of all nickel present in

the samples. After TPR, $NiAl_4O_7$ contained 0.5% unreduced nickel, $NiAl_2O_4$ contained 2.5% unreduced nickel, and $Ni_2Al_2O_5$ contained 1.3% unreduced nickel.

Hydrogen chemisorption was performed after temperature programmed reduction experiments. $NiAl_4O_7$ was found to have a low dispersion of 0.65%, $NiAl_2O_4$ 0.97%, and $Ni_2Al_2O_5$ 0.51%. This indicated that the nickel reduced during the temperature programmed reduction experiment remains embedded in the aluminate and is not available for hydrogen uptake,[49] but is still likely available as a nucleation site for reactants.[5]

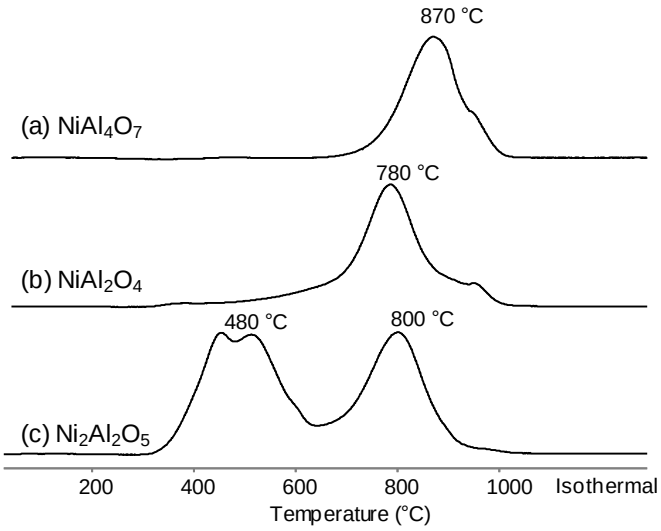

Figure 4.3 - Temperature programmed reduction of $NiAl_4O_7$, $NiAl_2O_4$, and $Ni_2Al_2O_5$.

Temperature programmed oxidation was performed on the samples after temperature programmed reduction and H_2 chemisorption measurements (Figure 4.4). The total quantities of oxygen consumption (Table 4.1) indicated that $NiAl_4O_7$ was 88% re-oxidized, $NiAl_2O_4$ was 77% re-oxidized, and $Ni_2Al_2O_5$ 80% re-oxidized assuming an H_2/O_2 stoichiometry of 2/1. The calculated extent of re-oxidation is lower than the extent

of reduction due to oxygen uptake at room temperature that is excluded in the integration of the TPO profile due to the starting TPO temperature being at approximately 35 °C. The presence of low and high temperature O_2 consumption peaks indicated that multiple types of nickel are present in the samples. Most notably, $Ni_2Al_2O_5$ showed a low temperature peak at 380 °C and two higher temperature peaks at 850 °C and 1000 °C. $NiAl_2O_4$ had a primary oxidation peak at 320 °C and two smaller peaks at 900 °C and 1000 °C. $NiAl_4O_7$ showed a broad low temperature oxidation peak at 440 °C and a small, high temperature oxidation peak at 970 °C.

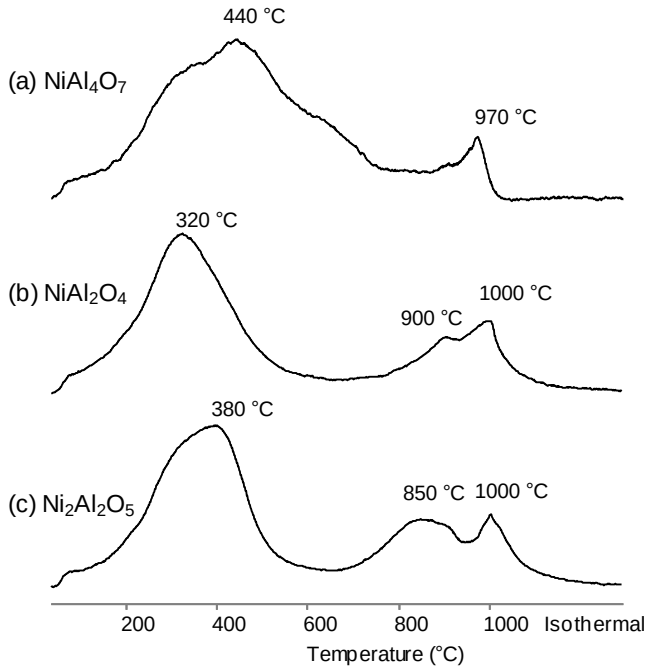

Figure 4.4 – Temperature programmed oxidation (TPO) of nickel aluminates.

The samples were exposed to a second TPR treatment (TPR2) after TPO (Figure 4.5). The values of H_2 uptake (Table 4.1) were less than 5% different of those found in

the initial TPR. The reduction temperature for bulk aluminate species increased by 40 °C for $NiAl_4O_7$, 70 °C for $NiAl_2O_4$, and 20 °C for $Ni_2Al_2O_5$. A single monomodal peak at 340 °C was observed in the trace for $Ni_2Al_2O_5$ and is attributed to agglomeration of nickel species in this sample during the preceding treatment steps.

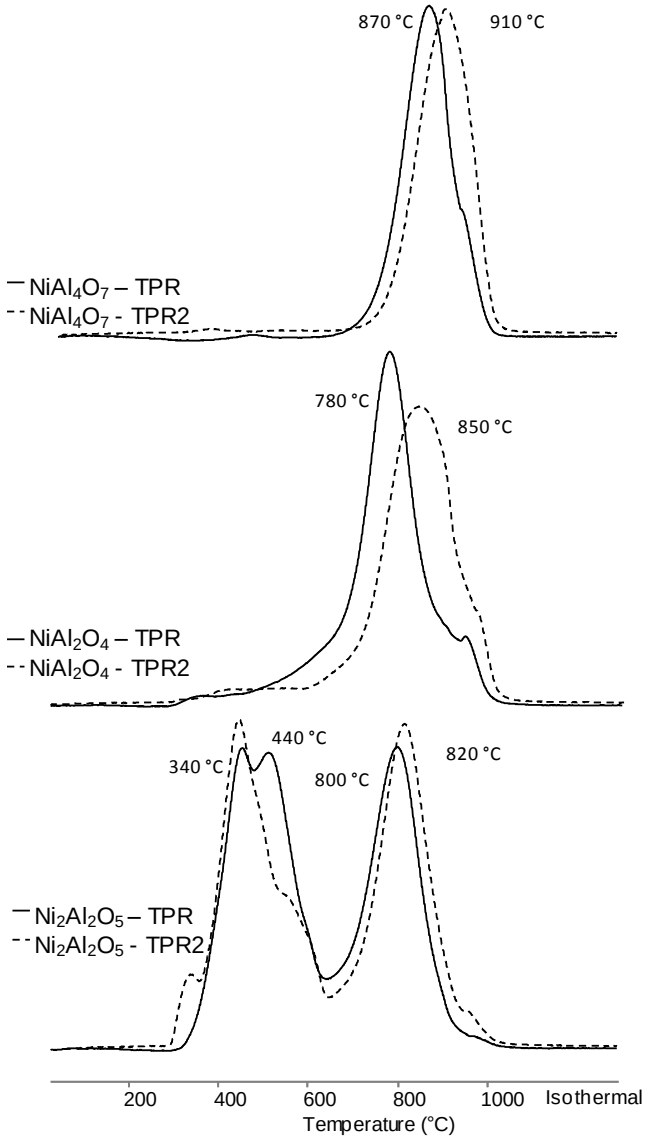

Figure 4.5 – Temperature programmed reduction after TPR and TPO.

4.3.1.3 X-ray Diffraction (XRD)

XRD measurements were performed on fresh samples and after TPR, TPO, and TPR2 experiments. The diffractograms of fresh $NiAl_4O_7$ (Figure 4.6), $NiAl_2O_4$ (Figure 4.7) and $Ni_2Al_2O_5$ (Figure 4.8) were dominated by peaks matching the $NiAl_2O_4$ phase using HighScore Plus and the International Centre for Diffraction Data (ICDD) database. The diffractogram of $Ni_2Al_2O_5$ also exhibited additional peaks corresponding to NiO. After the TPR experiment, only metallic nickel was observed in the diffractograms. A minor phase was detected for $NiAl_2O_4$ and $NiAl_4O_7$ after reduction. Based on previous reports it might have the composition $NiAl_{32}O_{49}$.[157] This phase may also be present but undetectable in fresh and oxidized samples due to the overlap of the XRD peaks of bulk $NiAl_2O_4$. XRD of samples after TPR, TPO, and TPR2 demonstrate the mobility of nickel in the nickel aluminate structure by the ability of the material to return to a state similar to the fresh sample after high temperature treatments.

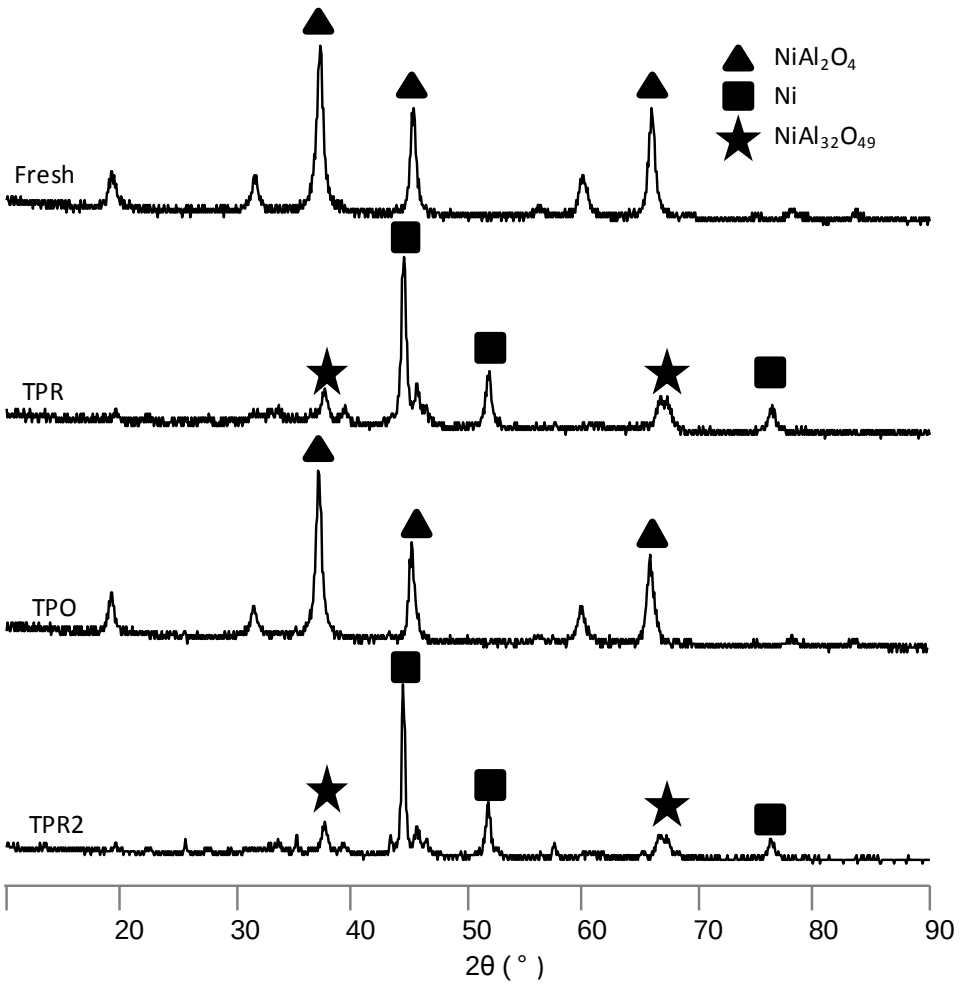

Figure 4.6 - XRD $NiAl_4O_7$ after various treatments.

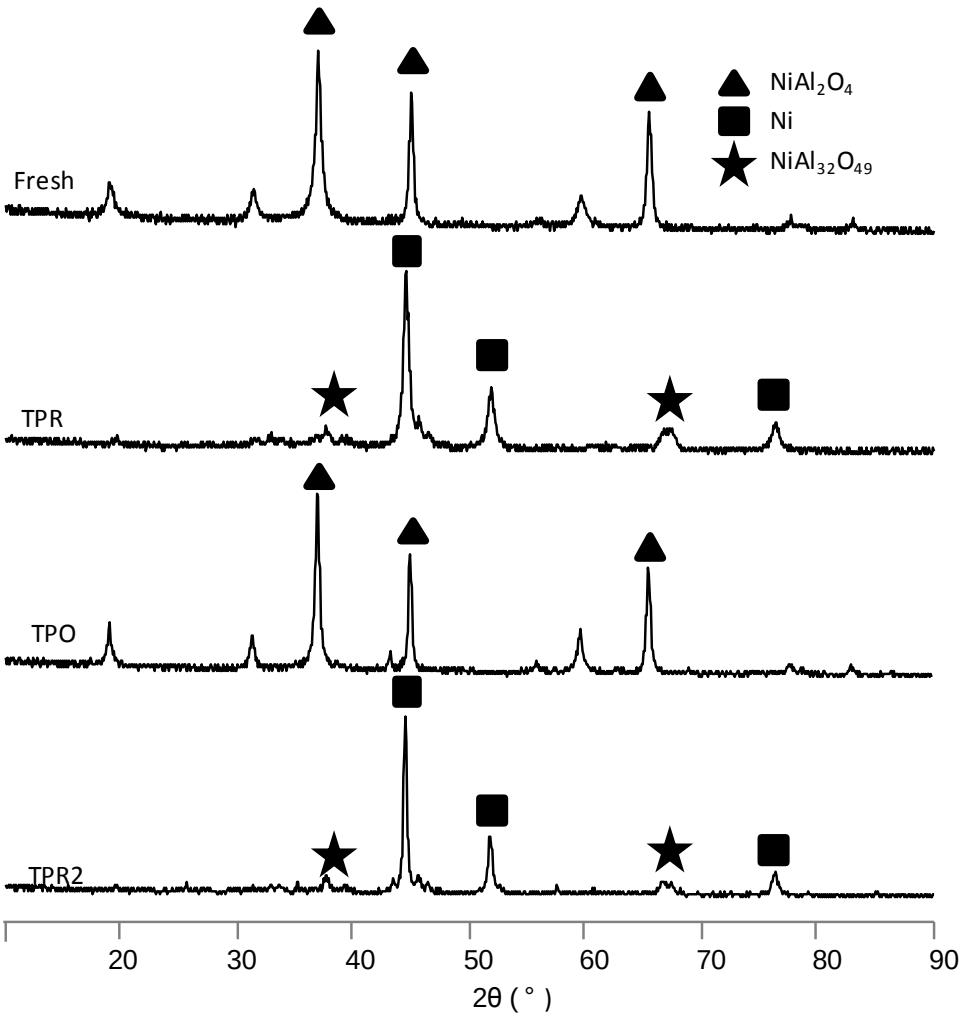

Figure 4.7 - XRD $NiAl_2O_4$ after various treatments.

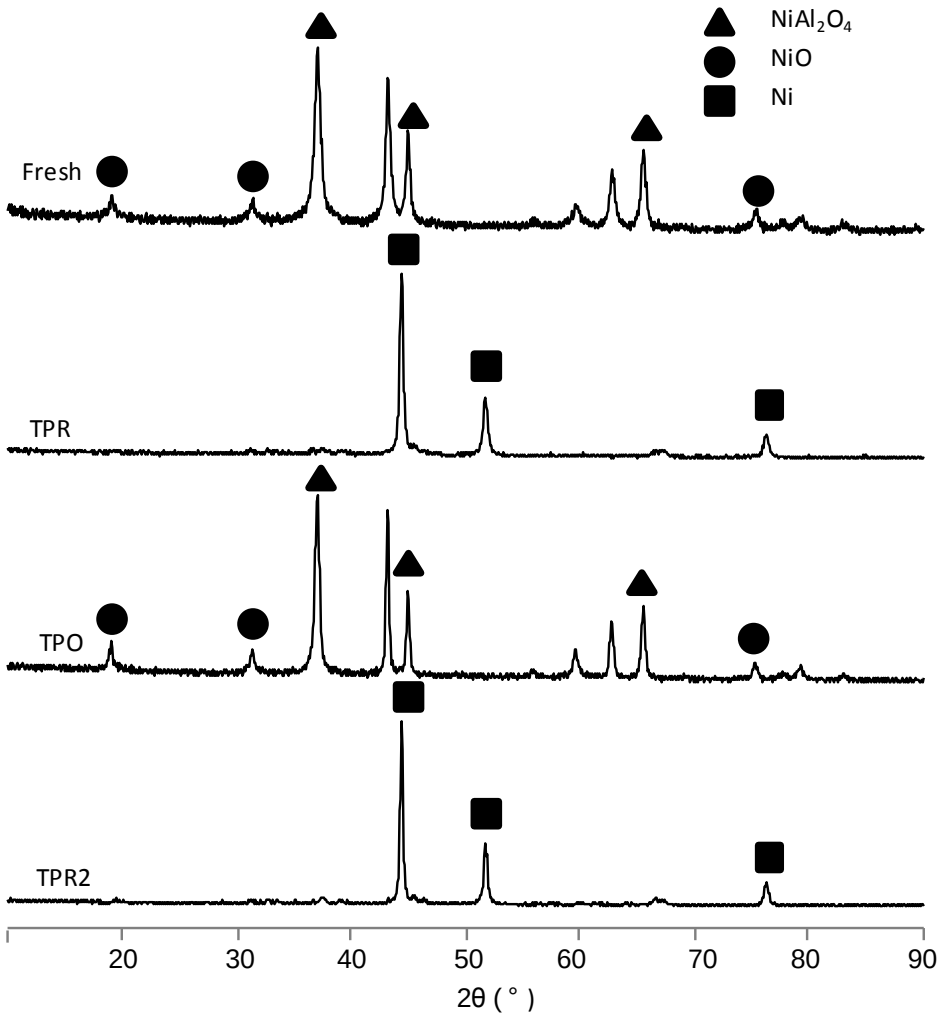

Figure 4.8 - XRD $Ni_2Al_2O_5$ after various treatments.

4.3.1.4 In-situ XRD

Materials were exposed to a hydrogen atmosphere, and the temperature of the XRD cell was incrementally increased to the experimental apparatus' maximum temperature (T = 700 °C). No change in crystallite structure was observed for $NiAl_4O_7$ or $NiAl_2O_4$ (Figures A.1 and A.2, respectively) as expected based on high temperature reduction peaks indicated by TPR. For $Ni_2Al_2O_5$, a shift to lower 2θ of the most intense Bragg peaks (2θ = 37° and 43°) was observed in the presence of hydrogen as low as 600

°C (Figure 4.9). The decrease in 2θ suggested a decrease in the crystallite size which implied the reduction of Ni^{2+} atoms inside the host material.[39] This observation is supported by the formation of metallic nickel at 650 °C, which was accompanied by a decrease in intensity of the $NiAl_2O_4$ peaks.

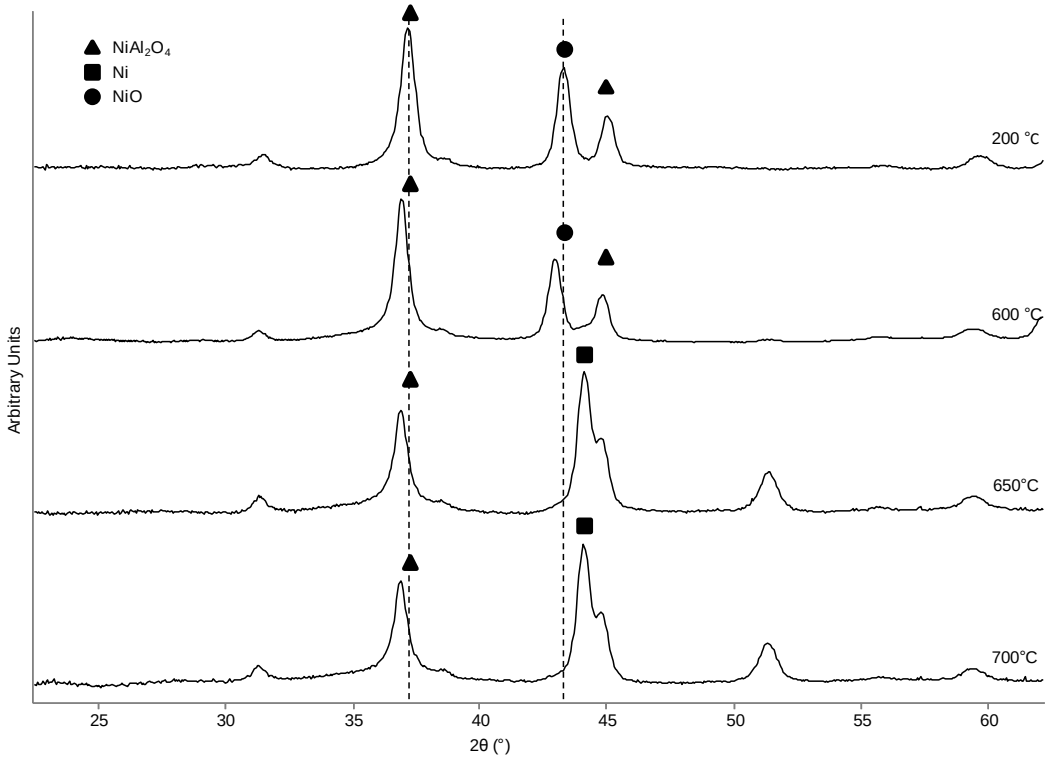

Figure 4.9 - $Ni_2Al_2O_5$ exposed to hydrogen as a function of increasing temperature.

4.3.1.5 Transmission Electron Microscopy

Bright field TEM images were collected for $Ni_2Al_2O_5$ (Figure 4.10a), $NiAl_4O_7$ (Figure 4.10b) and $NiAl_2O_4$ (Figure 4.10c,d). Pores and voids can be easily identified in the TEM images of $NiAl_2O_4$ and $NiAl_4O_7$. In agreement with N_2 physisorption results, the pores of $NiAl_2O_4$ can be described as uniform cylindrical pores and that of $NiAl_4O_7$ as complex pores with ill-defined shapes and sizes. The narrow slit like pores described by the hysteresis loop of $Ni_2Al_2O_5$ were not easily observed. Diffraction patterns were obtained and indicated mixed oxide phases (Figure A.3). Crystallite sizes were calculated using dark field TEM images (Figure A.4), which allowed ease of identification of individual crystallites due to the increased contrast. High angle annular dark field (HAADF) scanning transmission electron microscopy (STEM) were acquired, and energy dispersive X-ray spectrometry (EDX) was performed (Table 4.2, Figures A.5-A.7). The atomic composition was found to be similar to that obtained using ICP-OES (Table 4.1).

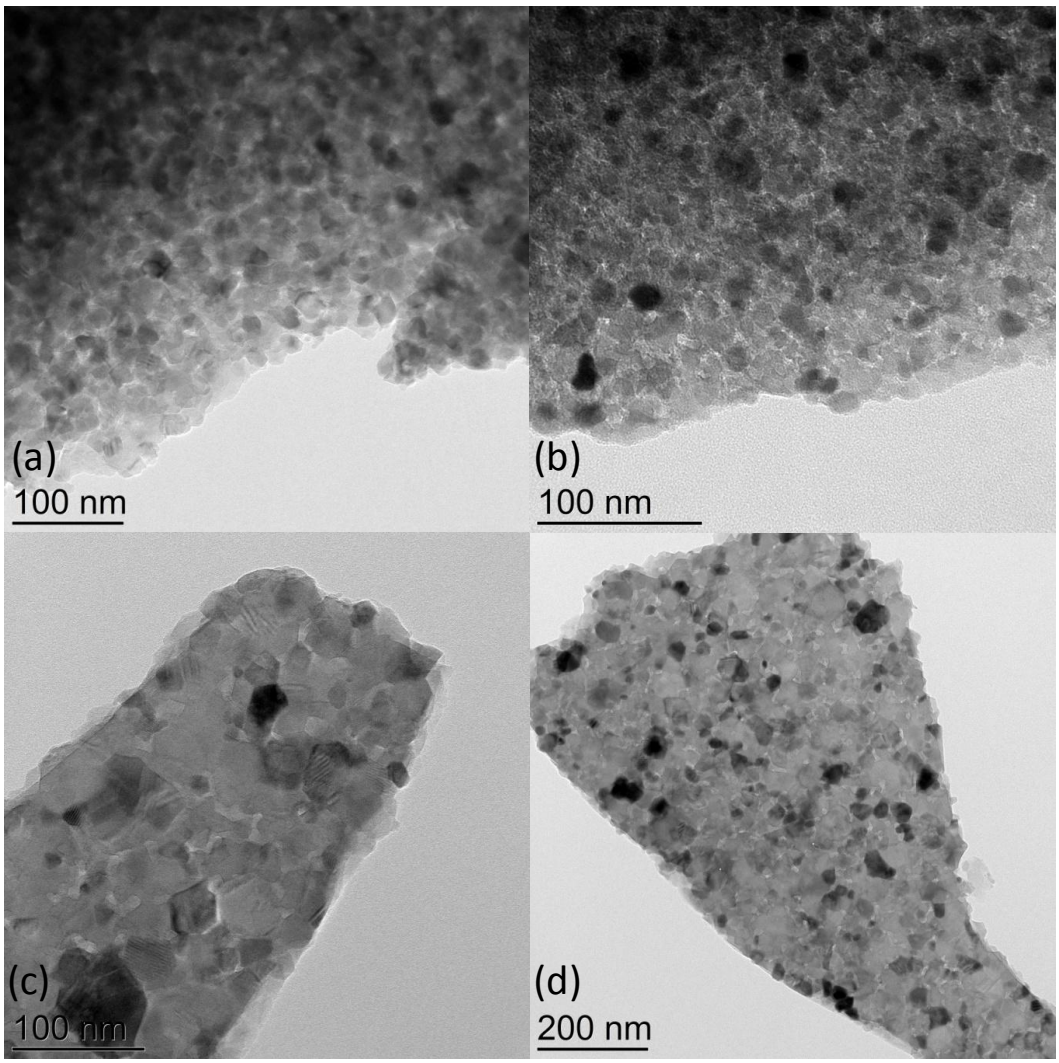

Figure 4.10 – Transmission electron micrographs of fresh $Ni_2Al_2O_5$ (a) $NiAl_4O_7$ (b) $NiAl_2O_4$ (c,d).

Table 4.2 – Average crystallite size calculated from dark field TEM image and sample composition from STEM-EDX mapping.

	Average crystallite size (nm)	**Average Ni (mol %)**	**Average Al (mol %)**	**Average O (mol %)**	**Empirical formula from STEM-EDX**
$NiAl_4O_7$	14	9.3	37.8	52.9	$NiAl_4O_6$
$NiAl_2O_4$	23	12.4	26.7	60.9	$NiAl_2O_5$
$Ni_2Al_2O_5$	14	22.5	24.6	52.9	$NiAlO_2$

4.3.1.6 X-ray Photoelectron Spectroscopy

X-ray photoelectron (XPS) spectra were obtained for fresh aluminate samples (Figure A.8). The Ni 2p scan revealed two main peaks, $Ni2p_{3/2}$ and $Ni2p_{1/}2$, and their respective satellite peaks. The splitting of the main peak is due to "spin-orbit coupling" between the electron spin and the angular momentum vector.[158] The satellite peaks next to the main peaks occur because there are two final states with different occupation of 3d orbitals due to 4s – 3d interactions.[18] Gardner et al. studied Ni substituted aluminates by XPS and found that separation between the satellite peak and the main peak of 6.3 ± 0.3eV is due to Ni bound in the aluminate structure and separation of 7.1 ± 0.1 eV is due to Ni in NiO. The main peaks in our samples had a separation from the satellite peak of 6.3 ± 0.1 eV, which indicated that surface nickel was primarily in the form of the aluminate structure. A BE of 531.3 eV was found for oxygen in $NiAl_2O_4$, and the O1s binding energy (BE) increased with increasing oxygen content. In all samples, the Ni/Al ratio was found to be about 5 times lower than the theoretical ratio (Table 4.3), which may indicate that a certain fraction exists in a nickel deficient aluminum-oxygen

rich phase deposited on the surface of the $NiAl_2O_4$ spinel.[138] This phase could be $NiAl_{32}O_{49}$ that was detected in XRD.

Table 4.3 – Surface compositions of fresh catalysts by XPS.

	Ni $2p_{3/2}$ BE (eV)	**O1s BE (eV)**	**Al 2p BE (eV)**	**Ni/Al Experimental**	**Ni/Al Theoretical**
$NiAl_4O_7$	856.3	531.5	74.8	0.04	0.25
$NiAl_2O_4$	856.3	531.3	74.6	0.11	0.5
$Ni_2Al_2O_5$	856.2	531.1	74.6	0.21	1.0

4.3.2 Methane Dry Reforming and Methane Steam Reforming Reactivity

$NiAl_4O_7$, $NiAl_2O_4$, $Ni_2Al_2O_5$, and a commercial 50 wt% Ni/α-Al_2O_3 catalyst from Alfa Aesar were tested for methane dry reforming reforming activity at 700 °C. The activity of the samples was tested when the samples were reduced and unreduced prior to reaction. Methane conversions (t = 6h) for active samples are reported in Table 4.4. $NiAl_4O_7$ was found to be active for methane dry reforming when reduced prior to reaction (Figure 4.11a) and had stable conversion of both methane and carbon dioxide over the time period examined. Unreduced $NiAl_4O_7$ had low but increasing conversion. $NiAl_2O_4$ was active for methane dry reforming in the reduced and unreduced state (Figure 4.11b). Reduced $NiAl_2O_4$ exhibited a decrease in conversion relative to the initial conversion of 6% for carbon dioxide and 8% of methane. Unreduced $NiAl_2O_4$ had stable carbon dioxide conversion and a decrease in methane conversion of 8%. The H_2/CO ratio obtained during methane dry reforming over $NiAl_2O_4$ in the reduced and unreduced state was found to 0.8. For reduced $NiAl_4O_7$ the ratio was 0.9. $Ni_2Al_2O_5$ and commercial 50

wt% Ni/α-Al_2O_3 were very active for methane conversion under dry reforming conditions, but rapid coking required a reactor shut down.

The catalysts were also evaluated for steam reforming at 700 °C in unreduced and reduced states. $Ni_2Al_2O_5$ was active for methane steam reforming with or without reduction prior to reaction (Figure 4.12). The conversion of methane decreased relative to the initial conversion by only 7% for reduced $Ni_2Al_2O_5$ and 2% for unreduced $Ni_2Al_2O_5$ over 12 h on stream. $NiAl_2O_4$ was active for methane steam reforming when reduced prior to reaction (Figure 4.12), and methane conversion decreased by 2% over 12 h. The commercial 50 wt% Ni/α-Al_2O_3 also showed sustained activity for methane steam reforming when unreduced prior to reaction, and the conversion of methane decreased by 1% over 12 h on stream. The conversion (t = 6h) over commercial 50 wt% Ni/αAl_2O_3 (XCH_4 = 85%) was slightly greater than that of the nickel aluminates (XCH_4 = 78-83%). However, the hydrogen concentration was higher than the detection limit of the online GC indicating the H_2/CO ratio was extremely high. The H_2/CO ratio obtained for methane steam reforming over nickel aluminates was approximately 5 for unreduced $Ni_2Al_2O_5$ and reduced $NiAl_2O_4$. For $Ni_2Al_2O_5$ reduced prior to reaction, the H_2/CO ratio was approximately 4.

Table 4.4 – Methane conversion (t = 6h) at 700 °C for $NiAl_4O_7$, $NiAl_2O_4$, $Ni_2Al_2O_5$, and commercial 50 wt% Ni/α-Al_2O_3 under methane steam reforming and methane dry reforming conditions.

	XCH_4[a] (%)			
	Reduced CH_4 Dry Reforming	Unreduced CH_4 Dry Reforming	Reduced CH_4 Steam Reforming	Unreduced CH_4 Steam Reforming
$NiAl_4O_7$	68	12	Not active	Not active
$NiAl_2O_4$	58	58	78	Not active
$Ni_2Al_2O_5$	Rapidly coked[b]	Rapidly coked[b]	82	78
50 wt% Ni/αAl_2O_3	Coked[c]	Rapidly coked[b]	Rapidly coked[b]	85

[a] **Methane conversions are assessed at t = 6h**
[b] **Coked requiring reactor shutdown at t < 1h**
[c] **Coked requiring reactor shutdown at t = 3h**

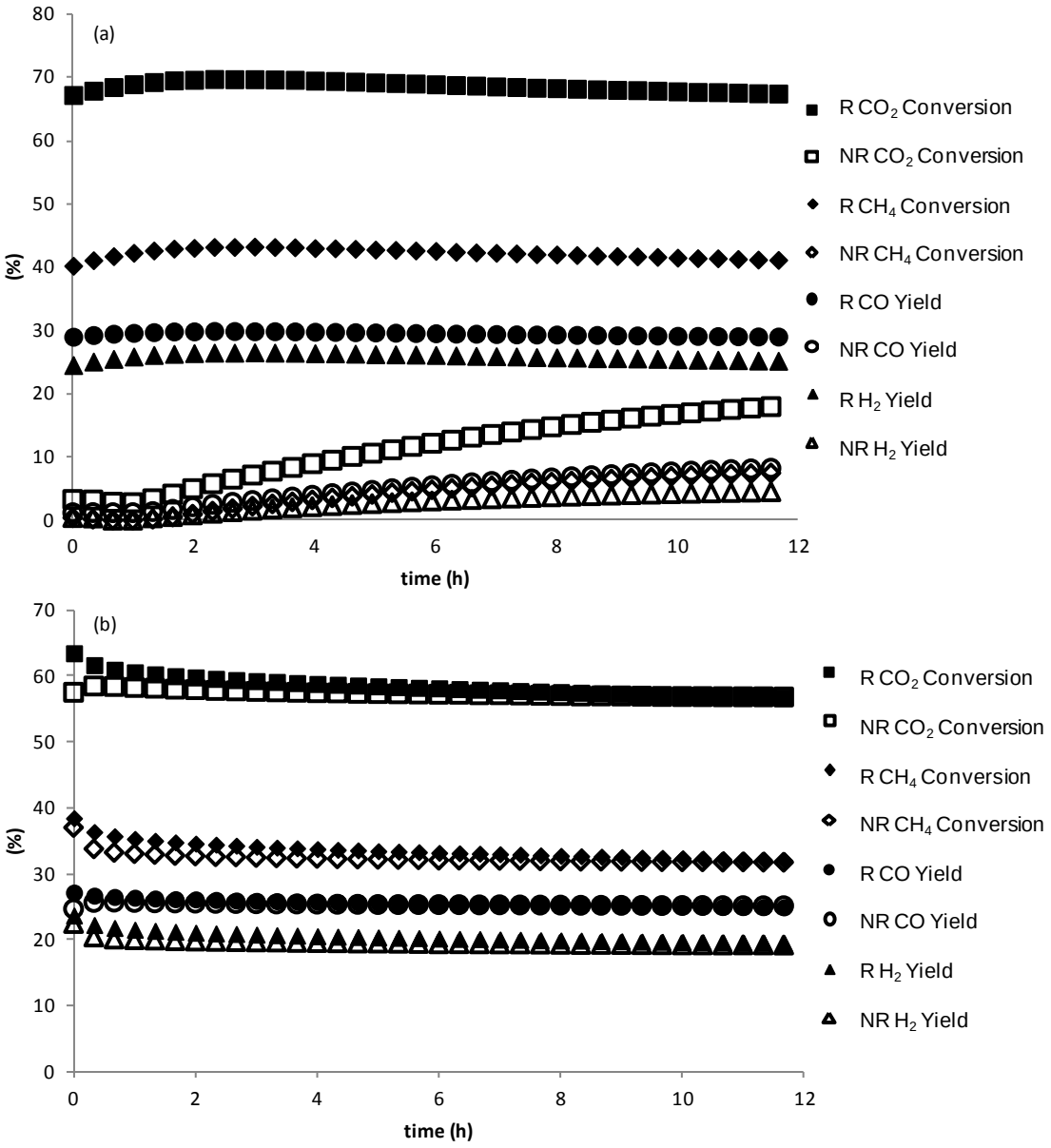

Figure 4.11 – CO_2/ CH_4 conversion and H_2/CO yield for methane dry reforming reaction at 700 °C, 1:1 CH_4:CO_2, reduced at 600 °C (2h) prior to reaction (R), unreduced prior to reaction (NR) for (a) $NiAl_4O_7$ and (b) $NiAl_2O_4$.

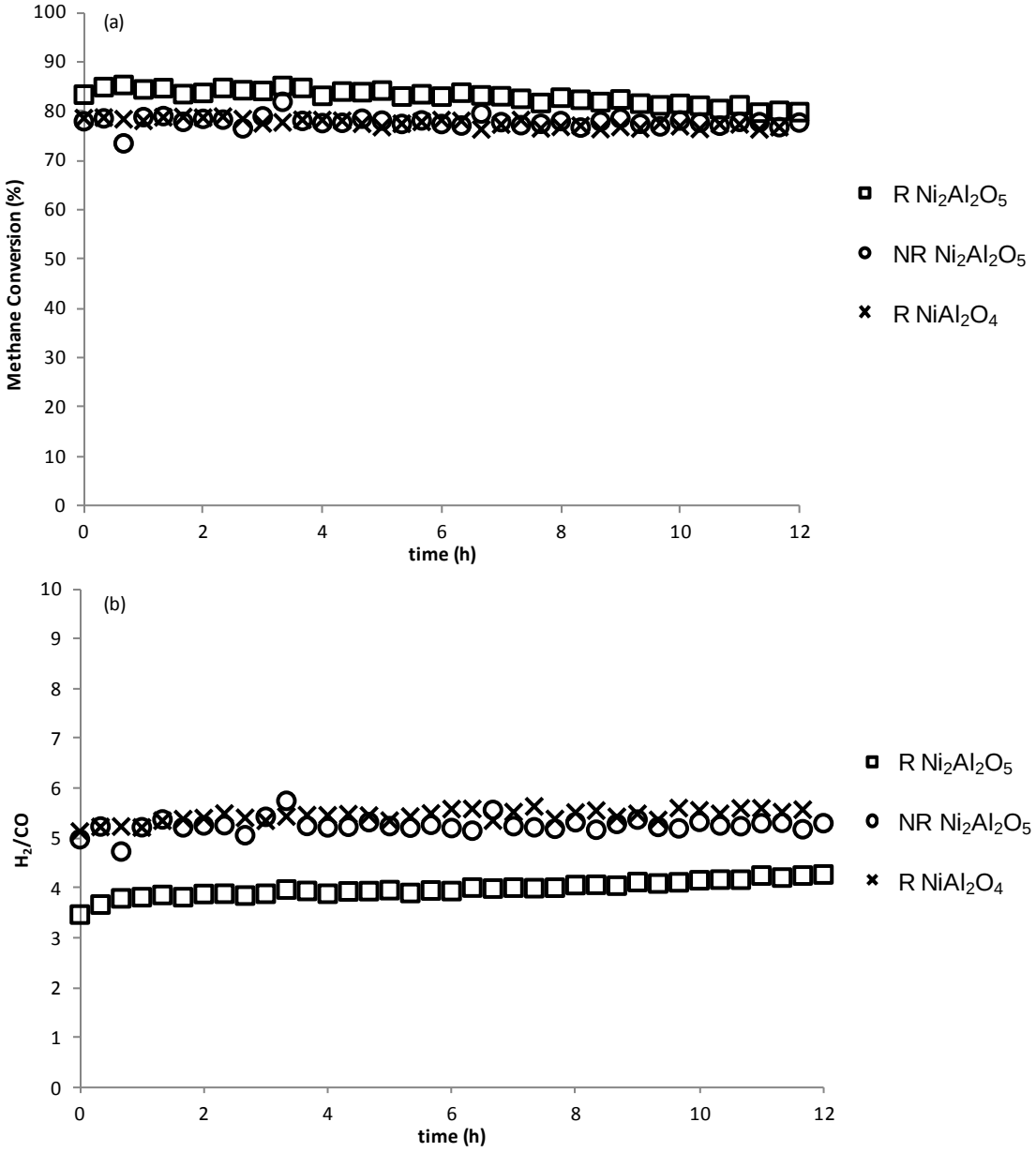

Figure 4.12 – (a) Methane conversion and (b) H_2/CO ratio methane steam reforming at 700 °C, S/C = 2.4, for $Ni_2Al_2O_5$ and $NiAl_2O_4$ reduced at 600 °C (2h) prior to reaction (R), unreduced prior to reaction (NR).

4.3.3 Carbonaceous Deposits

The carbon content for spent samples that were active and sufficiently stable for methane steam reforming and methane dry reforming was determined (Table 4.5). For methane dry reforming, nickel aluminates had carbon contents between 2.8 - 12.6 wt%. The commercial 50 wt% Ni/α-Al_2O_3 had a carbon content of 79% when reduced prior to reaction after just 3 h on stream. For methane steam reforming, nickel aluminates had carbon contents of less than 1.0 wt%, and the commercial 50 wt% Ni/αAl_2O_3 had a carbon content of 10.9 wt%.

Table 4.5 – Carbon analysis of spent samples utilized in 12 h reactor experiments.

Carbonaceous Deposits on Spent Samples (wt% C)

	Reduced CH_4 Dry Reforming	Unreduced CH_4 Dry Reforming	Reduced CH_4 Steam Reforming	Unreduced CH_4 Steam Reforming
$NiAl_4O_7$	5.0	2.8	ND[a]	ND[a]
$NiAl_2O_4$	12.6	7.5	1.1	ND[a]
$Ni_2Al_2O_5$	ND[b]	ND[b]	<0.5	<0.5
50 wt% Ni/αAl_2O_3	79.0[c]	ND[b]	ND[b]	10.9

[a] **Not determined (ND) because samples were not active.**
[b] **Not determined (ND) because samples coked causing reactor shutdown at t < 1h.**
[c] **Reactor was shut down at t = 3h due to coking. The carbon content was determined for comparative purposes.**

4.3.4 X-ray Absorption Spectroscopy (XAS)

XANES spectra of $NiAl_4O_7$, $NiAl_2O_4$, and $Ni_2Al_2O_5$ after reduction at 900 °C are presented in Figure 4.13. The white line intensity of the Ni K edge, which is indicative of the coordinative environment of Ni species, increased in the following order: $Ni_2Al_2O_5$ < $NiAl_2O_4$ < $NiAl_4O_7$. Further, the Ni^{2+} pre-edge is not easily observed in any of the samples indicating reduction to metallic nickel. It was found from linear combination fitting of the XANES region that $Ni_2Al_2O_5$ was completely reduced, $NiAl_2O_4$ was 85% reduced, and $NiAl_4O_7$ was 65% reduced which correlated well with integration of TPR profiles up to 900 °C (Table 4.9). The EXAFS curve fitting results for $NiAl_4O_7$ (Table 4.6), $NiAl_2O_4$ (Table 4.7), and $Ni_2Al_2O_5$ (Table 4.8) confirmed that after exposure to H_2 at 900 °C metallic nickel species were present. The true Ni-Ni coordination number of $NiAl_4O_7$, $NiAl_2O_4$, and $Ni_2Al_2O_5$ was found by normalizing the coordination number of Ni-Ni found in the EXAFS fitting by the fraction of metallic Ni found from the linear combination fitting of the XANES (Table 4.9). Upon determination of the true Ni-Ni coordination number, the nickel nanoparticle size present in reduced samples can be estimated. $Ni_2Al_2O_5$ was estimated to have nickel nanoparticles of approximately 3 - 4 nm, $NiAl_2O_4$ 6 - 7 nm, and $NiAl_4O_7$ 8 - 10 nm. After reduction, the samples were oxidized at 900 °C without exposure to air. After oxidation, the Ni-O coordination number was found to return to the value found in the fresh samples. The coordination numbers for fresh and re-oxidized samples were approximately 6, 5, and 4 for $NiAl_4O_7$, $NiAl_2O_4$, and $Ni_2Al_2O_5$, respectively.

The oxidation state of unreduced nickel aluminates after exposure to methane dry reforming reaction conditions was also investigated (Figure 4.14). Linear combination

fitting of the XANES region using NiO and Ni foil as references indicated during dry reforming that 10% of $Ni_2Al_2O_5$ was composed of Ni^0 and 90% Ni^{2+}. In contrast, no Ni^0 or Ni^{2+}could be fit using linear combination fitting in the case of $NiAl_4O_7$ and $NiAl_2O_4$ despite the clear decrease in white line intensity. The white line intensities of the samples after exposure to methane dry reforming were lower relative the freshly prepared samples, which can be attributed to a change in the coordination sphere of Ni. To investigate the change in coordination chemistry of the samples after exposure to reaction conditions, the EXAFS region was fit. It was found that the coordination number of Ni-O species in $NiAl_4O_7$ decreased from approximately 6 to 5, while $NiAl_2O_4$ and $Ni_2Al_2O_5$ decreased to about 4 suggesting that fourfold coordinated Ni^{2+} is the active site for dry reforming (Tables 4.6-4.8). To gain further insight into the changes in structure of nickel aluminates during methane dry reforming, difference spectra were created. This was achieved by subtracting the EXAFS region of the spectrum the fresh sample from the spectrum after methane dry reforming (Figure A.9). EXAFS fitting of the difference spectrum using a Ni foil standard indicated a Ni-Ni coordination number of 0.6 in $Ni_2Al_2O_5$, a trace of metallic Ni in $NiAl_2O_4$, and no metallic Ni was observed in $NiAl_4O_7$ (Figure 4.15). The true coordination is determined by dividing the experimental coordination number by the fraction of metallic Ni determined from the XANES. Thus, the true coordination number of metallic Ni in of $Ni_2Al_2O_5$ after exposure to reaction conditions is approximately 6 since only 10% of the nickel was present as nickel nanoparticles. From the true coordination number, the nickel nanoparticles sizes are estimated to be 1-2 nm. Since $NiAl_4O_7$ and $NiAl_2O_4$ contained little or no Ni-Ni coordination after exposure to reaction conditions, the difference spectra were fit using a

Ni-O scattering path (Figures A.10 – A.12). It was found that $NiAl_4O_7$ and $NiAl_2O_4$ contained Ni-O scattering in a different coordination than that of the fresh samples, which accounted for the observed decrease in oxygen coordination under reaction conditions (Tables 4.7 and 4.8, respectively) and a change in the shape of the XANES (Figure 4.14).

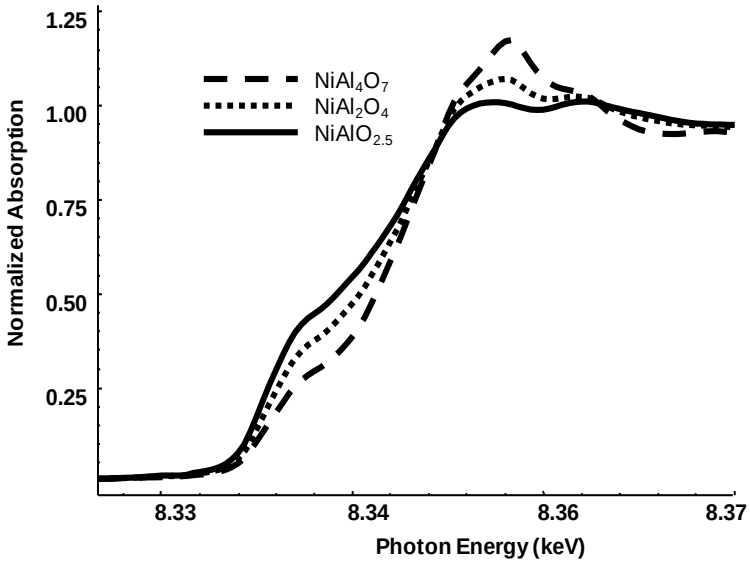

Figure 4.13 – Ni K-edge XANES from 8.32 to 8.37 keV of $NiAl_4O_7$, $NiAl_2O_4$, $Ni_2Al_2O_5$ after reduction at 900°C.

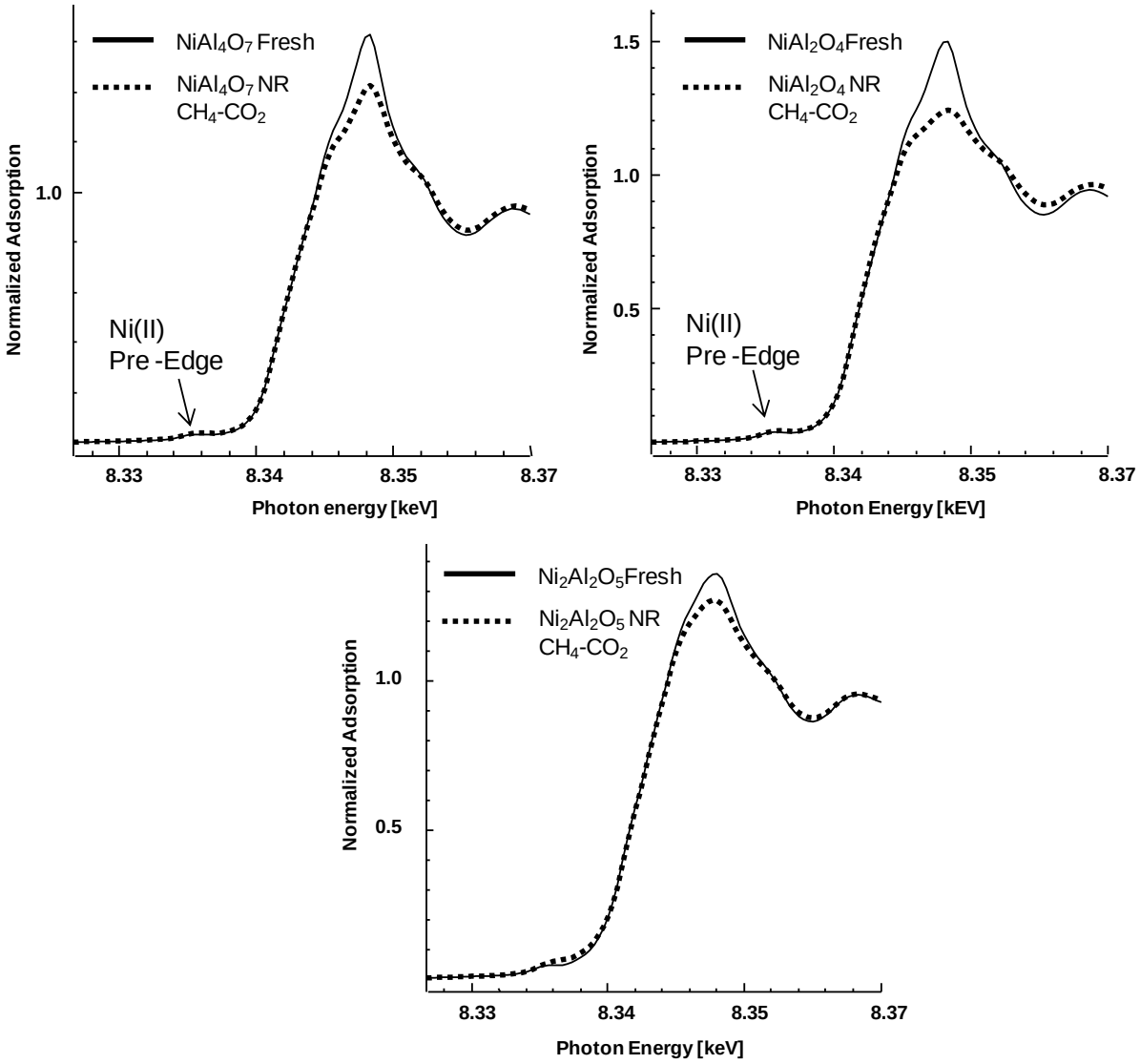

Figure 4.14 – XANES of fresh samples and after exposure to methane dry reforming (CH_4-CO_2) reaction conditions at 700 °C. Samples unreduced (NR) prior to exposure to reaction gas.

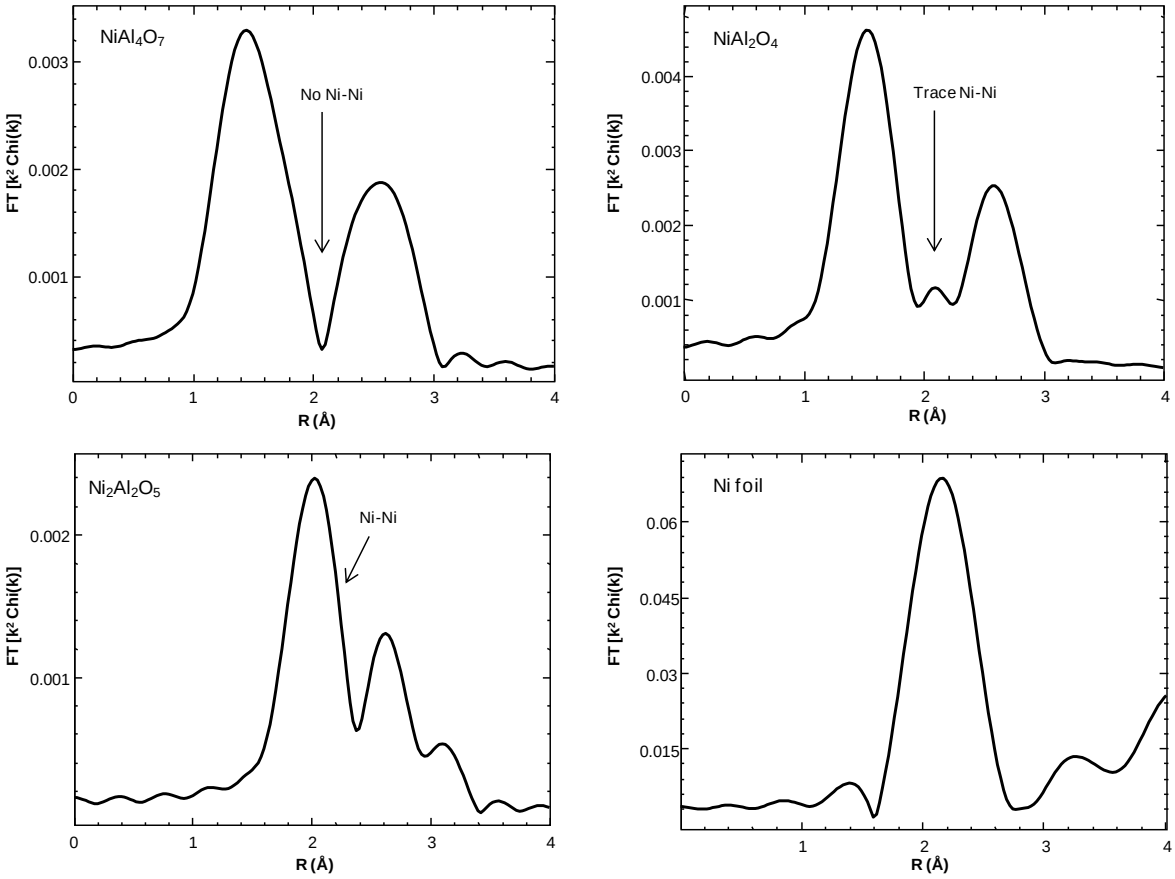

Figure **4.**15 - Ni K-edge FT of the difference EXAFS of nickel aluminates as synthesized minus catalyst after exposure to methane dry reforming ($CH_4 + CO_2$) reaction conditions.

Table 4. 6 - Curve fitting results for the Ni-K edge EXAFS of the $NiAl_4O_7$.

Treatment	Scatter	N	R, Å	$\Delta\sigma^2$ (x10^3)	Eo, eV
Fresh	Ni-O	6.1	2.06	1.0	-0.7
900 °C H_2	Ni-Ni	7.5	2.50	0.0	0.9
	Ni-O	2.0	2.05	0.0	4.4
900 °C O_2	Ni-O	6.1	2.07	3.0	-0.5
700 °C	Ni-O	5.3	2.06	1.0	-0.8
$CH_4 - CO_2$ Reforming	Ni-O	0.8	2.04	1.0	-2.7

[a]Difference spectrum created by subtracting the spectrum of the fresh sample from the spectrum of the sample after exposure to methane dry reforming.

Table 4.7 - Curve fitting results for the Ni-K edge EXAFS of the $NiAl_2O_4$.

Treatment	Scatter	N	R, Å	$\Delta\sigma^2$ (x10^3)	Eo, eV
Fresh	Ni-O	5.0	2.07	1.0	-2.0
900 °C H_2	Ni-Ni	8.9	2.50	1.0	0.3
900 °C O_2	Ni-O	5.0	2.07	3.0	-1.2
700 °C $CH_4 - CO_2$ Reforming	Ni-O	4.1	2.07	1.0	-0.1
	Ni-O Difference[a]	1.0	2.08	0.0	-1.1
	(Ni-Ni)	0.2	2.52	5.0	-11.7

[a]Difference spectrum created by subtracting the spectrum of the fresh sample from the spectrum of the sample after exposure to methane dry reforming.

Table 4.8 - Curve fitting results for the Ni-K edge EXAFS of the $Ni_2Al_2O_5$.

Treatment	Scatter	CN	R, Å	$\Delta\sigma^2$ (x10^3)	Eo, eV
Fresh	Ni-O	4.2	2.09	1.0	0.2
900 °C H_2	Ni-Ni	8.5	2.49	1.0	0.7
900 °C O_2	Ni-O	4.2	2.09	1.0	0.7
700 °C $CH_4 - CO_2$ Reforming	Ni-O	4.0	2.09	1.0	0.4
	Ni-Ni	0.6	2.45	5.0	-12.7

[a]Difference spectrum created by subtracting the spectrum of the fresh sample from the spectrum of the sample after exposure to methane dry reforming.

Table 4.9 – Linear combination fitting results for XANES spectra, true coordination number, and approximate Ni nanoparticle size for samples reduced at 900 °C in H_2.

Sample	Edge Energy (keV)	Fraction of Ni^0 and Ni^{2+} from XANES		References Used for LC Fit		Fraction Ni^0 from TPR[a]	True Coordination Number of Ni-Ni[b]	d (Ni) (nm)[c]
		Ni^{2+}	Ni^0	Ni^{2+}	Ni^0			
$NiAl_4O_7$	8.35	0.35	0.65	Fresh $NiAl_2O_4$	Ni Foil	0.69	11.5	8 – 10
$NiAl_2O_4$	8.35	0.15	0.85	NiO	Ni Foil	0.82	10.5	6 – 7
$Ni_2Al_2O_5$	8.33	-	1.0	-	Ni Foil	0.95	8.5	3 - 4
$Ni_2Al_2O_5$ CH_4-CO_2[d]	8.34	0.9	0.1	Fresh $Ni_2Al_2O_5$	Ni Foil		6	1 - 2

[a] TPR profile integrated to T = 900 °C
[b] True coordination number = CN/(XANES fraction Ni^0)
[c] Calculated using empirical correlation of H_2 chemisorption and EXAFS CN for Platinum [159]
[d] $Ni_2Al_2O_5$ unreduced under methane dry reforming (CH_4-CO_2)

4.4 Discussion

4.4.1 Formation of Nickel Aluminates

The formation of a rigid polymeric resin during Pechini synthesis allows for formation of nickel aluminates with unique and highly uniform unit cell properties.[47] During the calcination of the resins, the metal ions are thought to exhibit low diffusivity, which results in the synthesis of mostly uniform multicomponent oxides.[47] Liu et al. studied the magnetic properties of $NiFe_2O_4$ prepared by modified Pechini synthesis and found that the Pechini method resulted in spinels with good crystallinity and dispersion.[160] The chemical homogeneity of materials resulting from use of Pechini synthesis was also demonstrated by Ferri et al.[161] They investigated $BiFeO_3$ and found highly crystalline, homogeneously distributed perovskite, with small crystallite sizes.

The nickel aluminates prepared in the present study had moderate surface areas (25 – 40 m^2/g) and were mesoporous at room temperature allowing reactants to access a significant part of the material. The crystallite size of fresh samples found from TEM ranges from 14 – 23 nm. STEM-EDX analysis indicated nanoscale stoichiometry similar to bulk stoichiometry determined by ICP. However, XPS showed that these materials have an aluminum and oxygen rich surface at room temperature that might consist of a $NiAl_{32}O_{49}$ phase which was indicated by XRD. In agreement with previous studies,[47, 160, 161] our results indicate that the Pechini synthesis provides materials that have uniform compositions, high degree of crystallinity, and small crystallite sizes. In contrast, synthesis of stoichiometric $NiAl_2O_4$ by solid state reaction was found to produce a material with several types of NiO in addition to bulk $NiAl_2O_4$.[138] The non-uniform catalysts severely sintered and formed large quantities of carbonaceous deposits during catalytic methane decomposition.

4.4.2 Mobility of Nickel Species in Nickel Aluminates

Materials that are similar to nickel aluminates have shown very unique regenerative capabilities. Nishihata et al. studied Pd perovskites prepared by the alkoxide method for automotive emissions control.[46] It was found that Pd was able to move out of the perovskite lattice under reducing conditions and back in its original position in an oxidizing atmosphere giving it high catalytic activity and a long lifetime. In a separate study by Kizaki et al., $La(Fe_{1-x}Pd_x)O_3$ perovskites prepared by the alkoxide method were found to have excellent stability and activity for automotive emissions control due to nanospinodal decomposition.[142] In nanospinodal decomposition, the perovskite microscopically decomposes into $LaFeO_3$ and $PdFeO_3$ at high temperatures, but the

crystal structure itself is maintained. Li et al. examined Ni-Fe-Mg-Al-O catalysts prepared by coprecipitation for tar reforming of biomass derived syngas.[137] Under reducing conditions, uniform Ni-Fe nanoparticles were formed from the bulk mixed oxide, and under oxidizing conditions, the Ni-Fe nanoparticles were reincorporated into the bulk structure.

In the present study, TPR/TPO, XRD, H_2 chemisorption, and XAS demonstrated the regeneration potential of nickel aluminates at high temperatures in terms of reversible changes of their oxidation state. All samples were almost fully reduced (TPR), re-oxidized (TPO), and then re-reduced (TPR2). The TPR profiles showed $NiAl_4O_7$ and $NiAl_2O_4$ had only high temperature reduction peaks associated with reduction of bulk nickel aluminate. NiO, as well as bulk nickel aluminates, were reduced in $Ni_2Al_2O_5$. The combination of H_2 chemisorption and TPR indicates that nickel nanoparticles formed under reducing conditions remain at least partially embedded in the bulk structure. The broad TPO patterns indicated there were several types of oxygen acceptor sites present within the samples. TPR 2 showed that the reduction peak temperatures were only slightly increased, which indicated that the mobility of nickel was only slightly reduced after repeated exposure to high temperatures. For $Ni_2Al_2O_5$, TPR 2 showed the convergence of the multiple types of NiO species to one type of NiO species as the bimodal peak was narrowed, which is likely due to agglomeration of nickel nanoparticles on the aluminate surface creating somewhat larger nickel nanoparticles. XRD was performed on samples after each TPR/TPO treatment and demonstrated the mobility of nickel particles out of the host framework by the ability of the materials to return to a structure similar to their initial structure under conditions more severe than those used

during reactivity studies. XAS analysis complemented TPR/TPO and XRD results. Specifically, XANES indicated that after reduction at 900 °C, $NiAl_4O_7$ can be 65% reduced, $NiAl_2O_4$ can be 85% reduced, and $Ni_2Al_2O_5$ can be 100% reduced. After oxidation at 900 °C, the Ni-O coordination number of nickel aluminates was the same as in the fresh samples. We conclude that the ability of these materials to return to their initial state after exposure to oxidizing and reducing conditions at high temperature indicates their potential application for many high temperature reactions such as methane steam reforming and methane dry reforming.

4.4.3 Active Site for Methane Steam and Dry Reforming and their Role in Carbon Formation

Methane dry reforming occurs according to the stoichiometric equation[74, 162]

$$CH_4 + CO_2 \leftrightarrow 2CO + 2H_2 \quad \Delta H^0_{298K} = 247 \text{ kJ/mol (1)}$$

Methane steam reforming (Equation 2) follows the equation

$$CH_4 + H_2O \leftrightarrow CO + 3H_2 \quad \Delta H^0_{298K} = 206 \text{ kJ/mol (2)}$$

The water gas shift (Equation 3) reaction and formation of carbonaceous species (Equation 4,5,6) can also occur under the experimental conditions and can have significant impact on the target reactions (Equations 1,2).

$$2CO + H_2O \leftrightarrow CO_2 + H_2 \quad \Delta H^0_{298K} = 41 \text{ kJ/mol (3)}$$

$$CH_4 \leftrightarrow C + 2H_2 \quad \Delta H^0_{298K} = 75 \text{ kJ/mol (4)}$$

$$2CO \leftrightarrow C + CO_2 \quad \Delta H^0_{298K} = -171 \text{ kJ/mol (5)}$$

$$CO + H_2 \leftrightarrow C + H_2O \; \Delta H^0_{298K} = -131 \text{ kJ/mol (5)}$$

H_2/CO ratios of less than unity during methane dry reforming are commonly attributed to the inverse water gas shift reaction.[11] H_2/CO ratios from 3 to 16 have been observed during methane steam reforming and can be attributed to the forward water gas shift reaction.[48] The different direction of the water gas shift (Equation 3) during methane steam reforming or methane dry reforming, respectively, results from the different composition of the feed for these reactions.

Methane steam reforming has been proposed to proceed via dehydrogenation of methane to form surface carbon, which is oxidized by adsorbed oxygen from water dissociation.[132] Methane dry reforming is thought to proceed via decomposition of methane to form surface carbon and hydrogen, and reaction of surface carbon with carbon dioxide.[141] Fundamentally, the mechanism of methane steam reforming and methane dry reforming may not be significantly different.[11] However, the thermodynamics of methane dry reforming favor formation of nickel carbide or carbon, while methane steam reforming favors the formation of nickel or nickel oxide.[11] Deng et al. studied $LaPrFeNiO_3$ catalysts prepared by a modified Pechini synthesis for methane dry reforming and oxidative methane reforming.[39] During dry reforming, the catalysts deactivated due to the formation of stable, filamentous carbon, while during oxidative methane reforming (CH_4:CO_2:O_2 = 1:0.7:0.3) no carbonaceous deposits were observed. Salhi et al. studied Ni deficient nickel aluminates prepared by the sol-gel method for methane steam reforming.[48] Under reducing conditions dispersed nickel nanoparticles formed and were able to catalyze methane steam reforming. Due to the small size of these particles, carbon formation was very low. Sahli et al. studied $NiAl_2O_4$ prepared by a sol-gel like method for dry reforming of methane.[95] It was found that high activity with

limited coke formation required small metal particles that formed from the aluminate structure at the same temperature of the catalytic reaction.

Numerous studies using nickel catalysts have reported that the active species in reforming reactions are the reduced nickel metal particles.[45, 49, 95, 137, 138] Rivas et al. found that $LaNiO_3$ perovskites prepared by Pechini synthesis exhibited the highest stability for methane steam reforming.[138] The stability was said to result from the formation of highly dispersed reduced nickel crystallites after reduction that remained in close contact with the La_2O_3 substrate. Enger et al. studied nickel aluminates prepared by wet impregnation for methane steam reforming.[49] They found that after reduction in hydrogen, nickel particles were formed and were able to activate methane at temperatures greater than 627 °C. Riberio et. al studied $NiAl_2O_4$ prepared by combustion synthesis for methane dry reforming.[45] They concluded the reactivity of the nickel aluminate was due to the migration of nickel to the surface forming reduced nickel nanoparticles that co-existed with bulk $NiAl_2O_4$.

Our study found that $NiAl_2O_4$ was active for methane dry reforming in the unreduced state as well as the reduced state. Reduced $NiAl_4O_7$ was immediately active for methane dry reforming, and the conversion of methane and carbon dioxide was higher than that of $NiAl_2O_4$ in either the reduced or unreduced state. $Ni_2Al_2O_5$ was the only sample that contained metallic nickel and formed large amounts of carbonaceous deposits that required reactor shut down. Thus, the active phase during methane dry reforming of the materials used in this study, which limits the formation of carbonaceous deposits, appears to be highly dispersed fourfold coordinated Ni^{2+}. Square planar geometry can

occur for fourfold coordinated nickel species and would allow for nickel in such coordination to be accessible to reactants.[70]

XAS analysis of unreduced samples after exposure to methane dry reforming reaction conditions indicated that the oxygen coordination number of nickel decreased to about 4 suggesting that fourfold Ni^{2+} oxide is the active site. $NiAl_4O_7$ had no metallic Ni, $NiAl_2O_4$ had only trace amounts of metallic Ni, while 10% of the Ni in $Ni_2Al_2O_5$ was reduced to 1 – 2 nm (Table 4.9) nickel nanoparticles. Unreduced $Ni_2Al_2O_5$ was too active for methane dry reforming as rapid coking deactivated the catalyst. This indicated that even a moderate amount of metallic nickel is detrimental due to coke formation. An increased amount of carbonaceous deposit over metallic nickel is also predicted by thermodynamics of the methane dry reforming reaction due to the formation of nickel carbide/carbon. As indicated by *in-situ* XRD, the amount of metallic nickel in $Ni_2Al_2O_5$ increases when the sample is reduced prior to reaction. Thus, it is not surprising that pre-reduced $Ni_2Al_2O_5$ also formed coke rapidly and required a shutdown of the reactor. The absence of metallic Ni in $NiAl_4O_7$ and $NiAl_2O_4$ during methane dry reforming provided further evidence that the active site responsible for stable activity is likely highly dispersed fourfold coordinated Ni^{2+}. The activity of unreduced $NiAl_4O_7$ was low and slowly increased during the reaction time because Ni was originally encased as indicated by the higher oxygen coordination (CN ~ 5) in the fresh sample. Only when the sample is exposed to reaction conditions can Ni atoms migrate to an environment with a Ni-O coordination number around 4 where they are accessible and catalytically active. Tetrahedrally coordinated nickel has been cited as an active site for low weight loading nickel alumina catalysts in the highly selective reaction of oxidative dehydrogenation of

ethane to ethylene.[163] The amount of carbonaceous deposits during methane dry reforming increased in the following order: unreduced $NiAl_4O_7$ < reduced $NiAl_4O_7$ < unreduced $NiAl_2O_4$ < reduced $NiAl_2O_4$. The amount of carbon deposited appears to correlate with the amount of reduced nickel in the samples. Overall, the aluminates exhibited low deactivation and carbon formation during 12 h of reaction (less than 13 wt% carbon) relative to commercial 50 wt% Ni/α-Al_2O_3, which accumulated 78 wt% carbon in only 3 h on stream. The higher amount of coke formation observed in reduced $NiAl_2O_4$ is attributed to an increase in metallic Ni from the reduction process. Deactivation of stable nickel aluminates was less than 6% of carbon dioxide and 8% of methane during the 12 h reaction time and the H_2/CO ratio was very close to unity. These results indicate reduced $NiAl_4O_7$ provides optimal performance for methane dry reforming while limiting carbon formation.

In the case of methane steam reforming, nickel nanoparticles are the active phase.[132] Reduced and unreduced $Ni_2Al_2O_5$ as well as reduced $NiAl_2O_4$ were active for methane steam reforming and had H_2/CO ratios between 4 and 5. The slightly lower methane conversion of the unreduced $Ni_2Al_2O_5$ and reduced $NiAl_2O_4$ is attributed to lower amounts of nickel nanoparticles relative to reduced $Ni_2Al_2O_5$. This is in agreement with *in-situ* XRD measurement, which indicated the formation of metallic nickel in $Ni_2Al_2O_5$ as low as 650 °C. Reduced $NiAl_2O_4$ is believed to exhibit activity for methane steam reforming because of an increase in metallic nickel. An increase in metallic nickel was also inferred for reduced $NiAl_2O_4$ during methane dry reforming due to the observed increase in carbonaceous deposits. It is speculated that unreduced $NiAl_2O_4$ was not active for methane steam reforming because it only had a trace amount of nickel nanoparticles

as indicated by the XAS results of this sample under methane dry reforming conditions. XAS measurements after methane dry reforming indicated that 10% of the Ni in unreduced $Ni_2Al_2O_5$ was present as nanoparticles estimated to be 1-2 nm. We speculate that a similar amount of nickel nanoparticles exists in unreduced $Ni_2Al_2O_5$ during methane steam reforming. Carbon formation was very low on active aluminate samples, which could indicate the nickel nanoparticles remained small throughout the reaction as carbon nucleation requires nickel particles of a certain size.[95] Unreduced commercial 50 wt% Ni/α-Al_2O_3 was found to be slightly more active than the nickel aluminates. However, the H_2/CO ratio was extremely high which is an undesirable property if the resultant syngas is to be used for anything other than hydrogen production. The conversion of methane decreased during the 12 h study by less than 7% for all samples. The commercially available 50 wt% Ni/α-Al_2O_3 catalyst formed 10 times the amount of carbonaceous deposits of the active nickel aluminates. These results indicate that reduced $Ni_2Al_2O_5$ provides optimal methane steam reforming activity while limiting the formation of carbon.

4.5 Conclusions

Nickel aluminates prepared by Pechini synthesis are excellent candidates for high temperature reforming reaction catalysts. Physicochemical characterization revealed unique structural properties, indicated a high degree of mobility of nickel in the aluminate structure, and demonstrated the regeneration properties of nickel aluminates under harsh reaction conditions. At extended reaction times, when catalyst regeneration becomes necessary, introduction of an oxidative atmosphere should allow for the catalyst to return to its initial state (and activity). Fourfold coordinated nickel species are believed to be

responsible for high, stable methane dry reforming activity of $NiAl_4O_7$ and $NiAl_2O_4$. These sites form less coke under dry reforming conditions than the metallic nickel present in reduced $NiAl_2O_4$ and unreduced/reduced $Ni_2Al_2O_5$. The larger metallic nickel nanoparticles that cause coking in methane dry reforming are believed to be the active site during methane steam reforming. Reduced $NiAl_2O_4$ and unreduced/reduced $Ni_2Al_2O_5$ had high, stable activity and very low carbonaceous deposits during methane steam reforming studies, which indicates that the reduced metal particles in these materials are stabilized against sintering.

Chapter 5

General Conclusions and Outlook

The goal of this work was to advance the art of catalyst synthesis to science and show successful application of such rationally prepared catalysts to model reactions that would occur in catalytic upgrading of biomass derived syngas. It can often be found in the literature that very similar catalysts prepared by different groups exhibit different activity and stability, presumably due to differences in preparation. Typically, studies focused on rational synthesis procedures will omit catalytic testing, while studies that examine catalytic activity spend minimal amounts of time preparing catalysts. Combining rational catalyst preparation with reactivity studies is a powerful way to demonstrate that careful catalyst preparation and characterization is a worthwhile effort.

It is shown in Chapter 2 that Co/Al_2O_3 catalysts have moderate activity for methane dry reforming and suffer from severe deactivation during moderate times on stream (8 h). Cobalt catalysts have not been widely investigated for methane dry reforming, and this work demonstrates their activity could be improved using controlled synthesis methods. By controlling the adsorption of cobalt during preparation, a catalyst with higher activity and lower deactivation was prepared relative to a catalyst prepared by a more common albeit less controlled synthesis method, dry impregnation. If the controlled adsorption synthesis of 2 wt% Co/Al_2O_3 was further refined to eliminate surface precipitation due to preparation at alkaline pH, the activity and stability of these catalysts for methane dry

reforming could be further increased. One potential method to eliminate surface precipitation would be to investigate cobalt adsorption at longer contact times and a lower pH than used in this study, such as pH = 8. Further, this study demonstrates the danger of eliminating a catalyst candidate when it is prepared by uncontrolled methods. In an ideal situation, detailed reactor studies should be conducted with catalysts that have undergone extensive development in the catalysis synthesis literature.

In Chapter 3, 2 wt% Ni/Al_2O_3 catalysts prepared by controlled adsorption and dry impregnation were examined for methane dry reforming. Here, it is clearly demonstrated that the type of preparation affects the active site. Nickel catalysts have excellent activity for methane dry reforming, and the results indicate that catalysts with high metal loadings are not required to obtain desired activity. The active sites in nickel catalysts prepared using controlled adsorption, underwent dynamic evolution during reduction and methane dry reforming. Significant insight was gained regarding the formation of nickel aluminate, which is a highly discussed and disputed topic in the nickel alumina catalyst literature.[103],[117] Surface $NiAl_2O_4$ forms during calcination when dry impregnation preparation is used and NiO/ $NiAl_2O_4$ over layers form only during high temperature reduction for catalysts prepared by controlled adsorption. During oxidation studies, previously reduced catalysts prepared by controlled adsorption formed hollow core shell structures which may indicate that it is not a suitable catalyst for extended on stream studies where regeneration is required. This is a potential mode of deactivation for reforming catalysts that has not been

identified in the literature. Also of extreme interest is that a supposedly inactive phase, $NiAl_2O_4$, is found to be active and stable for methane dry reforming.

In Chapter 4, bulk nickel aluminates ($NiAl_2O_4$) were found to be active and stable for methane dry reforming and methane steam reforming. Redox studies indicate the potential for these materials to be utilized during high temperature reactions and during studies with long times on stream where regeneration will become necessary. The data indicate that different active sites in nickel aluminates are responsible for the stable conversion of CO_2-CH_4 and CH_4-H_2O reaction systems. Both methane steam reforming and methane dry reforming would occur to some extent during catalytic biogas conditioning and optimization of the ratio of these types of sites in nickel aluminates could drastically enhance biogas upgrading efficiency. Further, nickel aluminates offer the potential to overcome major modes of deactivation during biogas upgrading: coking, sintering, and attrition.

The investigations in this thesis clearly demonstrate the impact of preparation methods on the formation of catalytically active sites, and important insight for the fields of catalyst preparation and reforming reactions have been gained. Bulk nickel aluminates prepared by Pechini synthesis were identified as promising candidates for catalytic conditioning of biomass derived syngas. Potential future research pathways are:

The XAS of Ni K edge of nickel aluminates after exposure to methane steam reforming conditions (when samples are reduced and unreduced prior to the reaction) and methane dry reforming conditions (when samples are reduced prior

to the reaction) should be examined. Current data strongly suggests that methane steam reforming is catalyzed by small nickel nanoparticles, while stable activity for methane dry reforming can be catalyzed by fourfold coordinated nickel cations. These hypotheses could be confirmed by performing XAS studies after exposure to reaction conditions similar to the studies that were conducted in this dissertation with unreduced nickel aluminates for methane dry reforming.

Extended time on stream studies should be conducted using either methane steam reforming or methane dry reforming to confirm the regeneration potential of nickel aluminates indicated by the redox studies conducted in Chapter 4. While all collected data indicates this is true, this warrants further investigation and confirmation.

The effect of the preparation method of nickel aluminates on activity should be investigated. In the few cases in the literature where bulk nickel aluminates are studied for reforming reactions, it is found that $NiAl_2O_4$ is not active for the respective reactions if they are not first reduced.[49, 93, 132] It is interesting that nickel aluminates prepared by Pechini synthesis are active for methane dry reforming and methane steam reforming in the reduced and unreduced state and this unique feature may be due to preparation method. Suggested alternative preparations are solid state reaction and alkoxide method. Comparison of reactivity of the materials prepared by different methods is the first step in confirming Pechini synthesis results in unique reactivity. Analysis of carbonaceous deposits on spent samples by combustion analysis, XPS, and TEM

can provide significant insight into the different catalytic sites responsible for activity between the samples prepared by different methods.

The applicability of nickel aluminates as catalysts for catalytic upgrading of biomass derived syngas can be enhanced by examining their activity for tar reforming. Reforming of tars is a major problem associated with utilization of syngas from biomass gasification. Steam reforming of tar (toluene as the model tar compound) can be described by Equations 1 and 2,

$$C_7H_8 + 7H_2O \leftrightarrow 7CO + 11H_2 \qquad \Delta H^0_{298K} = 876 \text{ kJ/mol} \quad (1)$$

$$C_7H_8 + 14H_2O \leftrightarrow 7CO_2 + 18H_2 \qquad \Delta H^0_{298K} = 647 \text{ kJ/mol} \quad (2)$$

Preliminary investigation of the activity of nickel aluminates for tar steam reforming indicate that at 800 °C and a steam to carbon ratio of 3.3, $NiAl_2O_4$ and a commercially purchased 50 wt%/α-Al_2O_3 catalyst can convert 100% of the toluene fed. The product gas composition at 100% toluene conversion is shown in Figure 5.1.

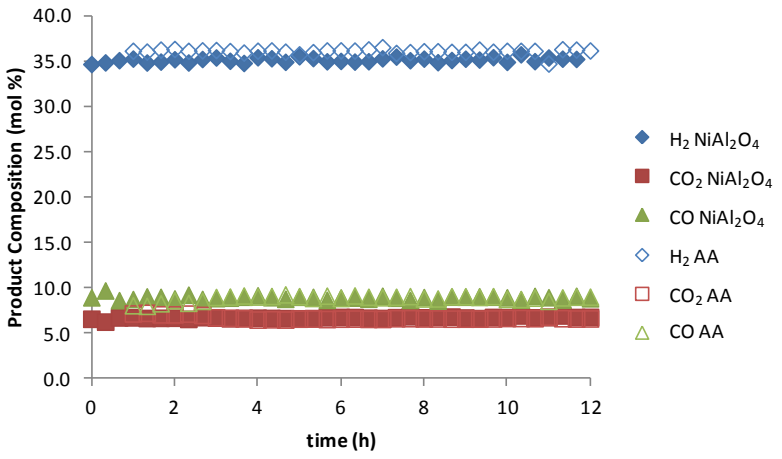

Figure 5.2 – Product composition at 100% toluene conversion. T = 800 °C, S/C = 3.3.

Steam to carbon ratios of less than 3.3 and greater than 1.5 should be investigated to find a ratio that allows for stable thermal conversion while allowing for differentiation in catalytic conversion of studied materials. Significant effort will need to be devoted to quantification of any higher molecular weight or polyaromatic compounds formed during toluene steam reforming to elucidate reaction pathways involved in the reforming of toluene. While these compounds can potentially be identified using the online GC, this would be very laborious approach. It is recommended that condensable compounds be collected from the reactor effluent and analyzed using GC-MS.

The next step in evaluating nickel aluminate activity for catalytic conditioning of biomass derived syngas would be to investigate the activity of nickel aluminates using realistic biogas environments *e.g.* a representative mixture of hydrogen, carbon monoxide, carbon dioxide, methane, tar, and steam. It is essential for a commercially viable biogas upgrading catalyst to reform both tar and methane[7] and previous studies have demonstrated the inhibiting effects of trying to simultaneously convert these two biogas contaminants.[4] The synergistic effects of biogas upgrading due to the presence of all biogas components can be partially decoupled by comparison of the independently studied reactions presented herein. A very versatile set-up has been constructed and tested during this thesis work to study complex reactions such as those involved in catalytic conditioning of biomass derived syngas. By incrementally increasing the complexity of the reactions studied using the novel reactor set-up, confidence in data quality can be ensured. Further, this thesis work has laid the

foundation to understand the different types of active sites that successfully and stably convert components of biogas such as methane, carbon dioxide, and steam.

In addition to the components mentioned above biomass derived syngas is also expected to contain hydrogen sulfide, inorganics, ammonia, and large polyaromatic compounds, such as naphthalene. The effect of these contaminants on nickel aluminate activity for upgrading of biomass derived syngas would be best investigated using a slipstream from a biomass gasification reactor.

Next generation materials for catalytic conditioning of biomass derived syngas should consider the addition of a third metal. For example, great success has been shown for various reforming reactions utilizing nickel aluminates that contain strontium, barium, or praseodymium. In addition to increasing overall activity, these elements have also been shown to enhance carbon gasification. From our studies in Chapter 4, the coordinative environment of nickel appears to play a crucial role in high, stable conversion during methane dry reforming. Extending this, the formation of carbonaceous deposits is one of the major modes of deactivation of nickel catalysts used for catalytic upgrading of biomass derived syngas. Ions such as strontium, barium, or praseodymium have been shown to influence the coordination of nickel in nickel aluminates,[144] thus, the addition of such a metal to the pure nickel aluminate would allow for a deeper understanding of the effect of coordinative environment of nickel on stable reforming activity.

APPENDIX A

SUPPLEMENTARY INFORMATION FOR CHAPTER 4

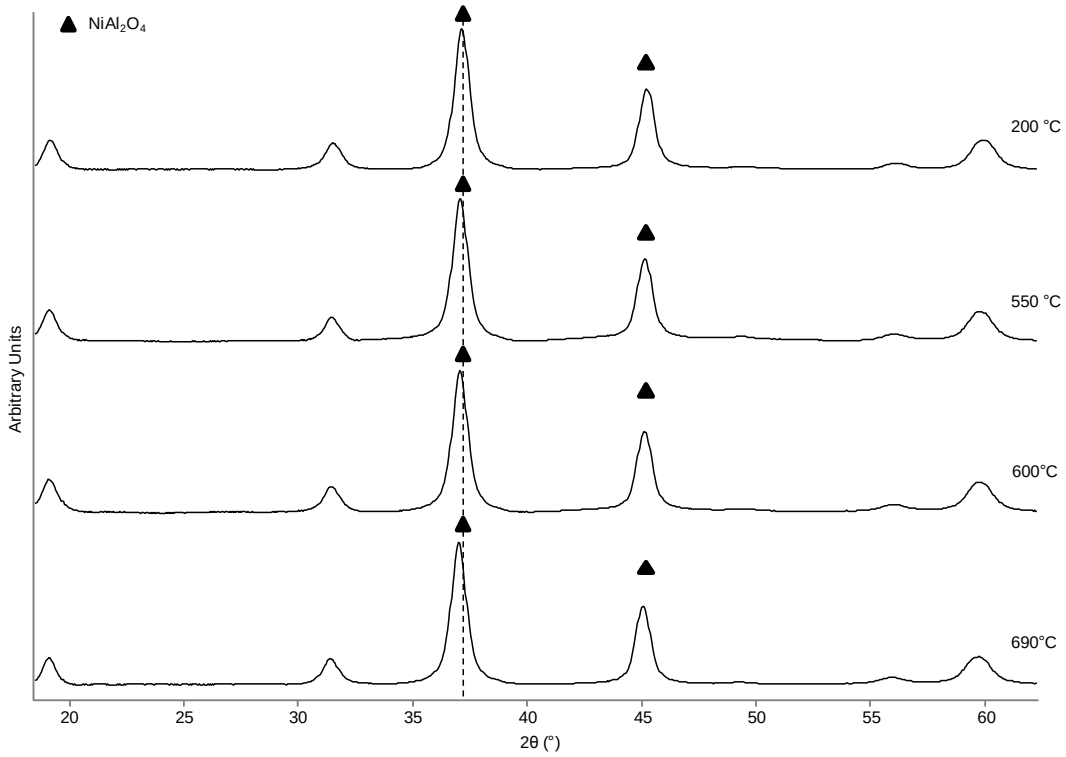

Figure A.1 – $NiAl_4O_7$ exposed to hydrogen as a function of increasing temperature.

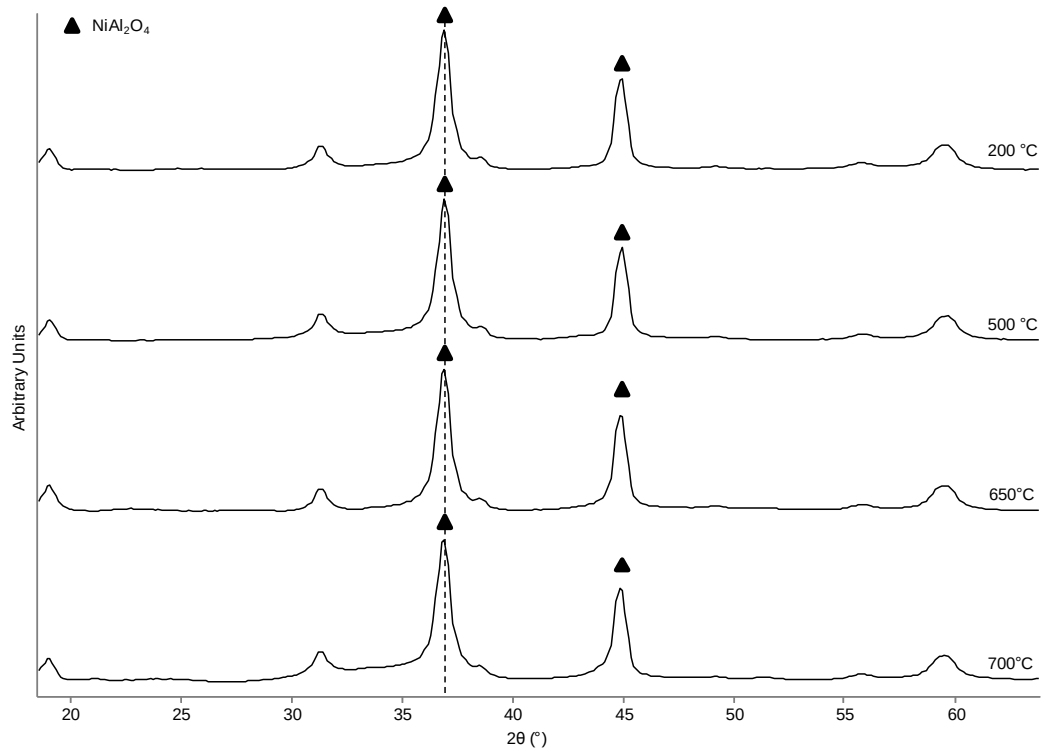

Figure A.2 – $NiAl_2O_4$ exposed to hydrogen as a function of increasing temperature.

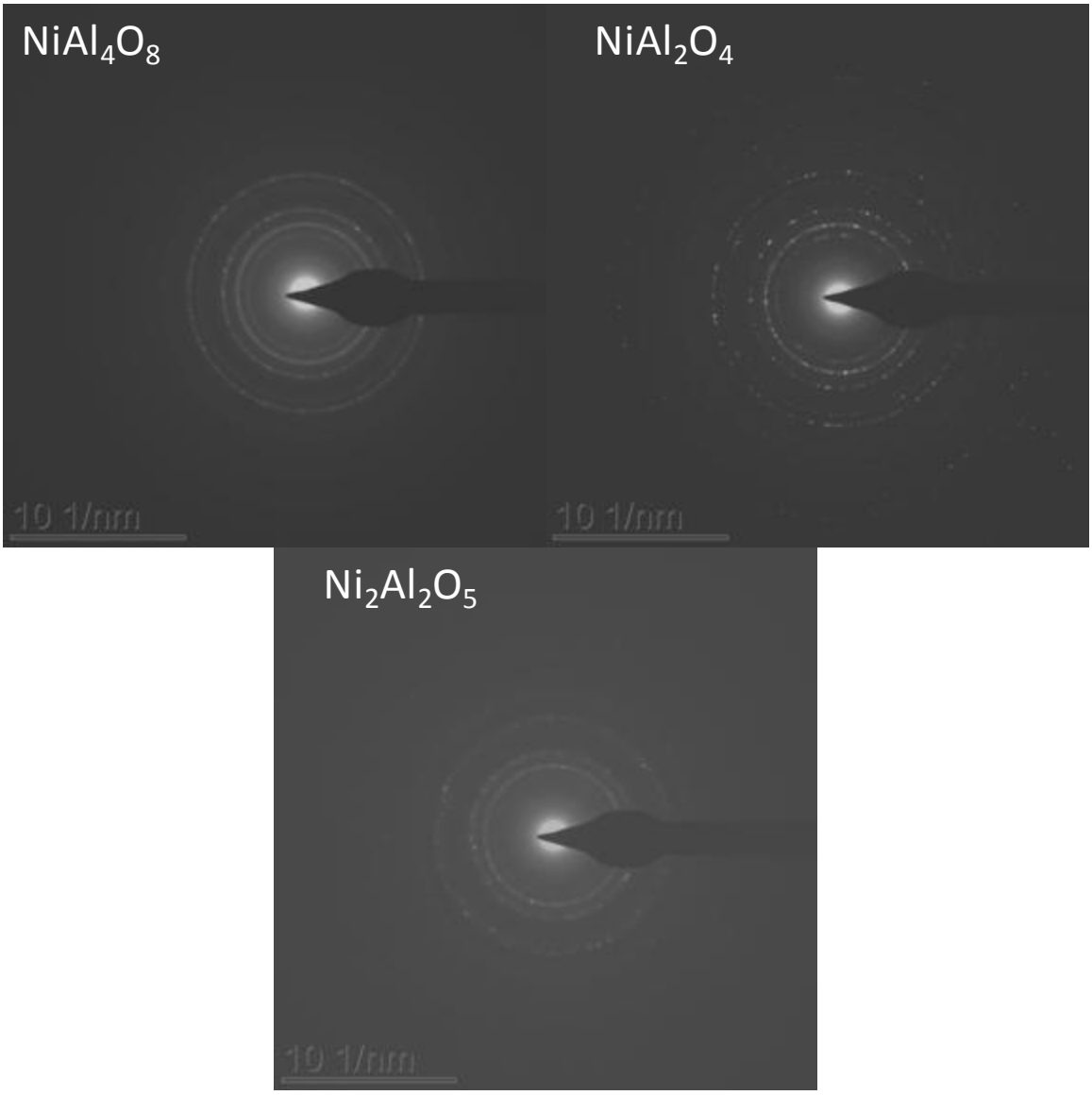

Figure A.3 – TEM diffraction patterns of nickel aluminates.

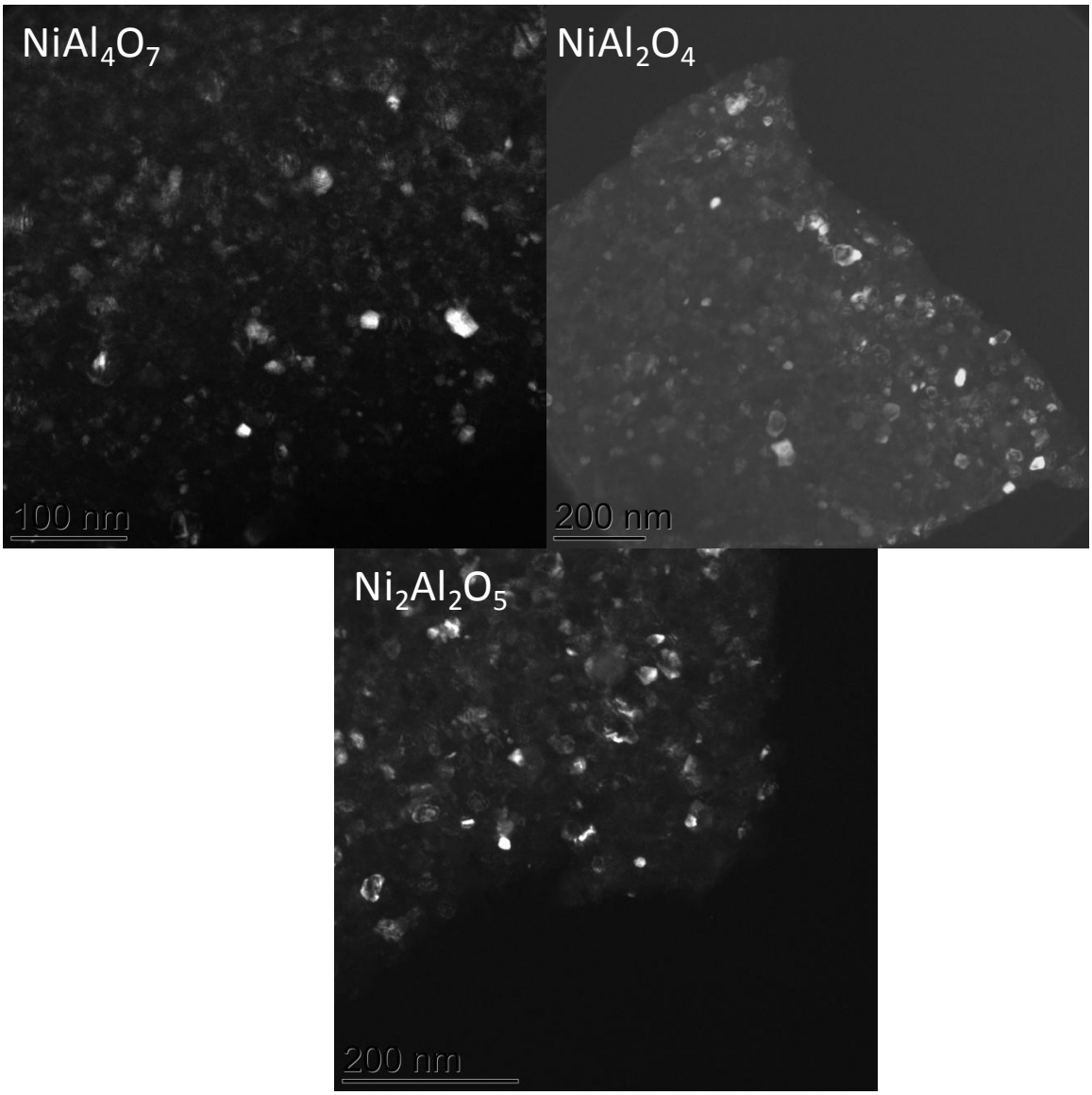

Figure A.4 – Dark Field TEM images used to calculate crystallite sizes of nickel aluminates.

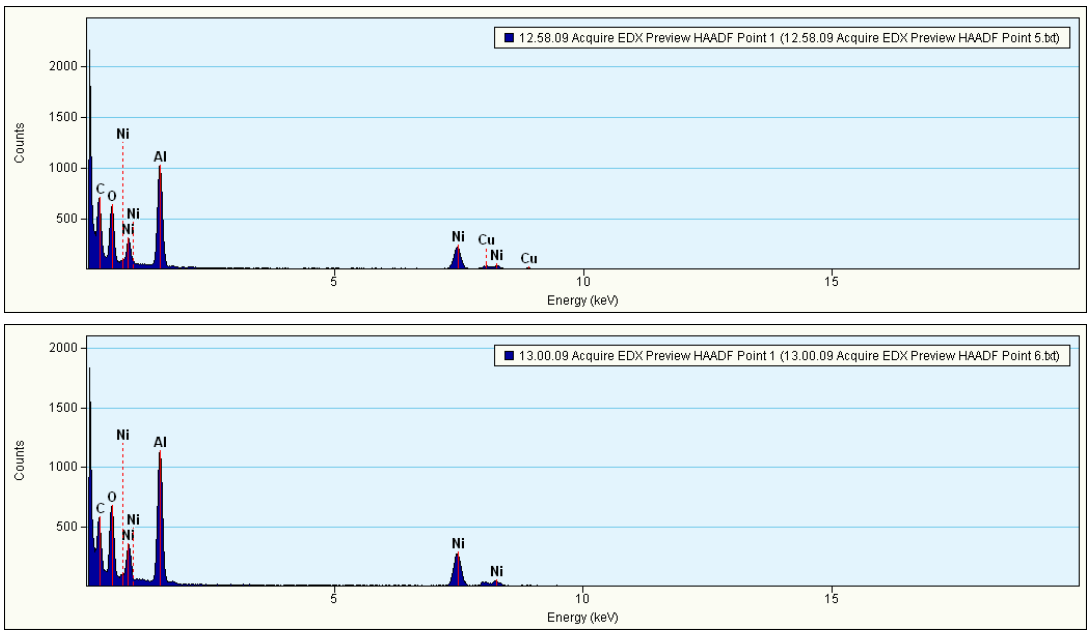

Figure A.5 – HAADF-STEM-EDX of $NiAl_4O_7$.

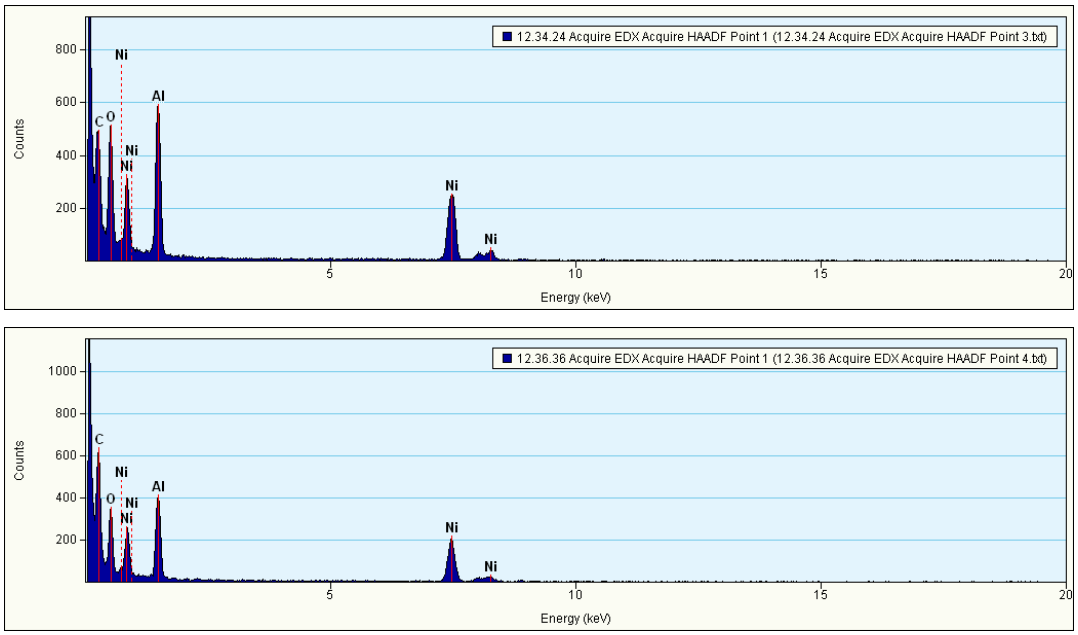

Figure A.6 – HAADF-STEM-EDX of $NiAl_2O_4$.

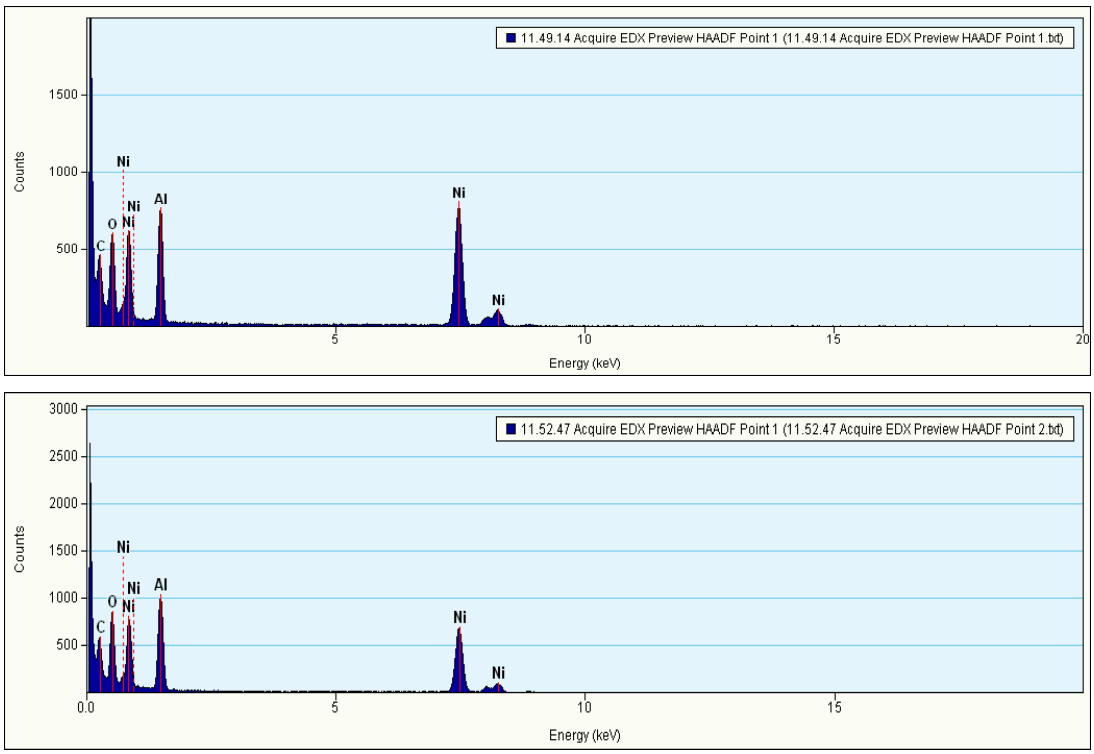

Figure A.7 – HAADF-STEM-EDX of $Ni_2Al_2O_5$.

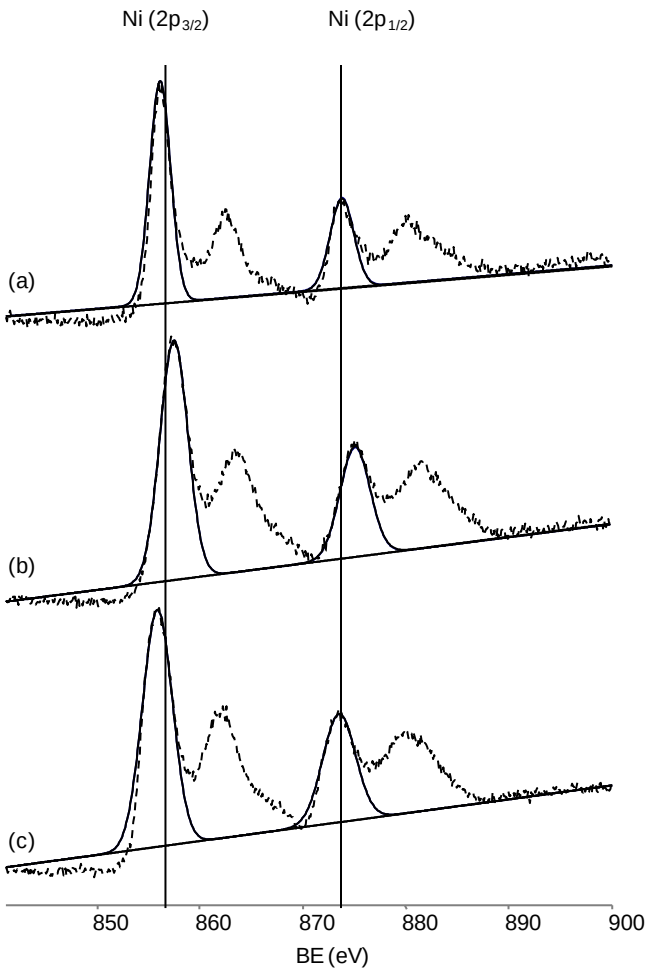

Figure A.8 – Ni 2p XPS of (a) $NiAl_4O_7$ (b) $NiAl_2O_4$ (c) $Ni_2Al_2O_5$.

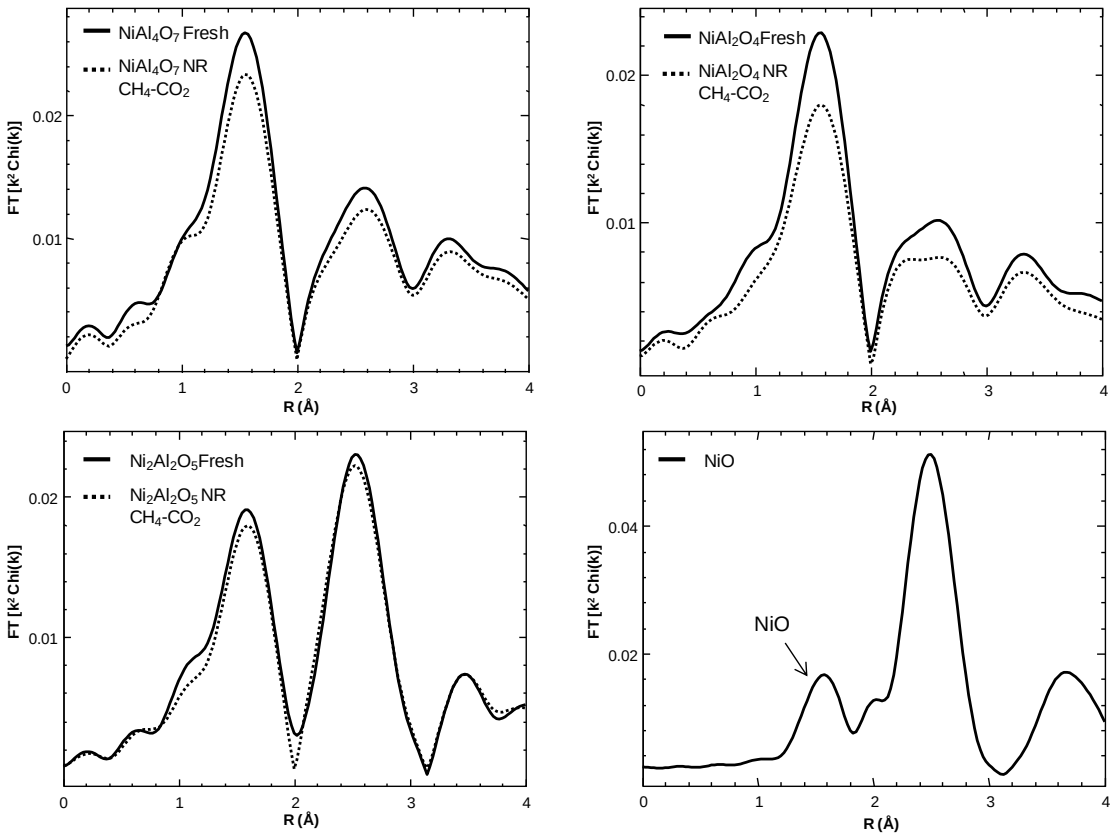

Figure A.9 - Ni K-edge Fourier transform of the k^2 weighted EXAFS of Fresh samples compared to samples under reaction conditions with the Ni K-edge Fourier transform of the k^2 weighted EXAFS of NiO reference.

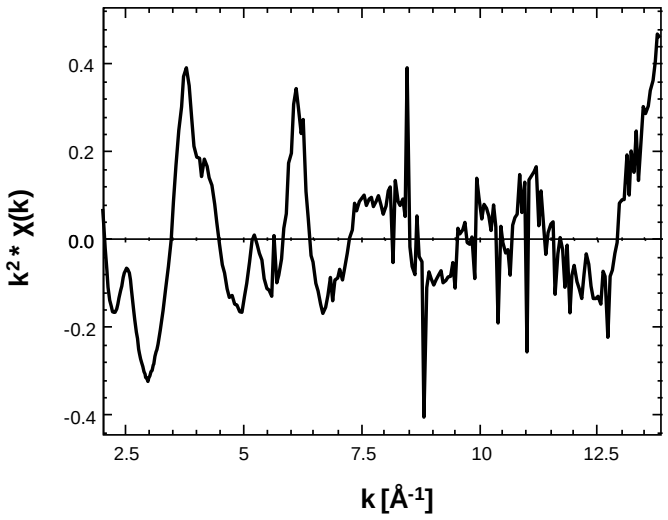

Figure A.10 - K^2 weight of the difference spectra of $NiAl_2O_4$ fresh and after exposure to methane dry reforming.

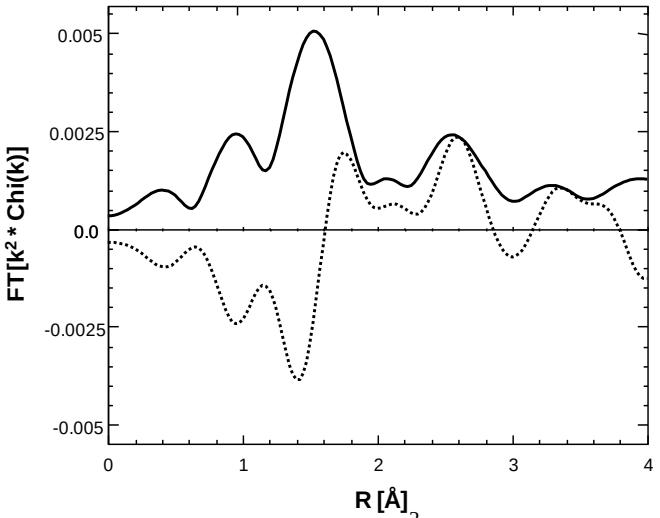

Figure A.11 - Ni K-edge Fourier transform of the k^2 weighted EXAFS of difference spectrum (Δk = 2.5 – 10.5 $Å^{-1}$; solid-magnitude FT and dotted-imaginary part FT).

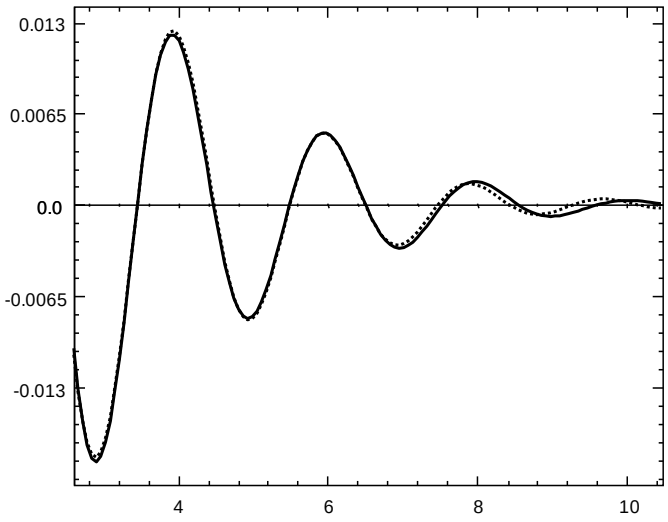

Figure A.12 - Solid-reverse FT of EXAFS data over $\Delta k = 1.17 – 1.97$ $Å^{-1}$ and dotted-EXAFS fit. Fit results: N = 1.0, R = 2.08 Å, DWF = 0, E_0 = -1.1.

REFERENCES

[1] E. Ruckenstein, Y.H. Hu, J. Catal. 162 (1996) 230-238.

[2] S.Y. Foo, C.K. Cheng, T.H. Nguyen, A.A. Adesina, J. Mol. Catal. A: Chem. 344 (2011) 28-36.

[3] D. San-Jose-Alonso, J. Juan-Juan, M.J. Illan-Gomez, M.C. Roman-Martinez, Appl. Catal. A: Gen. 371 (2009) 54-59.

[4] M.M. Yung, W.S. Jablonski, K.A. Magrini-Bair, Energy Fuels. 23 (2009) 1874-1887.

[5] T.L. Roussière, Chemistry and Biochemistry, Karlsruhe Institute of Technology, 2013, p. 238.

[6] W. Torres, S.S. Pansare, J.G. Goodwin, Catalysis Reviews-Science and Engineering. 49 (2007) 407-456.

[7] D. Sutton, B. Kelleher, J.R.H. Ross, Fuel Process. Technol. 73 (2001) 155-173.

[8] Z. Abu El-Rub, E.A. Bramer, G. Brem, Industrial & Engineering Chemistry Research. 43 (2004) 6911-6919.

[9] D. Dayton, in: NREL (Ed.), NREL, Golden, 2002, p. 33.

[10] R.Q. Zhang, R.C. Brown, A. Suby, K. Cummer, Energy Conversion and Management. 45 (2004) 995-1014.

[11] S.B. Wang, G.Q.M. Lu, G.J. Millar, Energy & Fuels. 10 (1996) 896-904.

[12] J. Lif, M. Skoglundh, L. Lowendahl, Appl. Catal. A: Gen. 228 (2002) 145-154.

[13] E. Gulbransen, S. Jansson, Oxid Met. 4 (1972) 181-201.

[14] S. Chenna, P.A. Crozier, Micron. 43 (2012) 1188-1194.

[15] T. Miyazawa, T. Kimura, J. Nishikawa, S. Kado, K. Kunimori, K. Tomishige, Catalysis Today. 115 (2006) 254-262.

[16] A.W. Budiman, S.-H. Song, T.-S. Chang, C.-H. Shin, M.-J. Choi, Catal. Surv. Asia. 16 (2012) 183-197.

[17] S.H. Seok, S.H. Choi, E.D. Park, S.H. Han, J.S. Lee, J. Catal. 209 (2002) 6-15.

[18] A. Winkler, H. Borchert, K. Al-Shamery, Surf. Sci. 600 (2006) 3036-3044.

[19] W.L. Chu, W.S. Yang, L.W. Lin, Catal. Lett. 74 (2001) 139-144.

[20] S.L. Soled, E. Iglesia, R.A. Fiato, J.E. Baumgartner, H. Vroman, S. Miseo, Topics in Catalysis. 26 (2003) 101-109.

[21] T. Furusawa, A. Tsutsumi, Applied Catalysis a-General. 278 (2005) 195-205.

[22] T. Furusawa, A. Tsutsumi, Applied Catalysis a-General. 278 (2005) 207-212.

[23] L.P.R. Profeti, E.A. Ticianelli, E.M. Assaf, Fuel. 87 (2008) 2076-2081.

[24] M. Neurock, J. Catal. 216 (2003) 73-88.

[25] J.F. Li, R. Yan, B. Xiao, D.T. Liang, L.J. Du, Environmental Science & Technology. 42 (2008) 6224-6229.

[26] K.P.d. Jong, Synthesis of Solid Catalysts, Wiley, Utrecht, 2009.

[27] J. Haber, J.H. Block, B. Delmon, Pure Appl. Chem. 67 (1995) 1257-1306.

[28] J.R. Regalbuto, A. Navada, S. Shadid, M.L. Bricker, Q. Chen, J. Catal. 184 (1999) 335-348.

[29] M. Schreier, J.R. Regalbuto, J. Catal. 225 (2004) 190-202.

[30] J.T. Miller, M. Schreier, A.J. Kropf, J.R. Regalbuto, J. Catal. 225 (2004) 203-212.

[31] L. Jiao, J.R. Regalbuto, J. Catal. 260 (2008) 329-341.

[32] L. Jiao, J.R. Regalbuto, J. Catal. 260 (2008) 342-350.

[33] L. D'Souza, L. Jiao, J.R. Regalbuto, J.T. Miller, A.J. Kropf, J. Catal. 248 (2007) 165-174.

[34] X. Hao, L. Quach, J. Korah, W.A. Spieker, J.R. Regalbuto, J. Mol. Catal. A: Chem. 219 (2004) 97-107.

[35] J. Korah, W.A. Spieker, J.R. Regalbuto, Catal. Lett. 85 (2003) 123-127.

[36] L. Jiao, Y. Zha, X. Hao, J.R. Regalbuto, in: E.M. Gaigneaux, M. Devillers, D.E. De Vos, S. Hermans, P.A. Jacobs, J.A. Martens, P. Ruiz (Eds.), Scientific Bases for the

Preparation of Heterogeneous Catalysts, Proceedings of the 9th International Symposium, 2006, pp. 211-218.

[37] J. R. Regalbuto, Catalyst Preparation, CRC Press, 2006, pp. 297-318.

[38] M. Gaudon, L.C. Robertson, E. Lataste, M. Duttine, M. Menetrier, A. Demourgues, Ceramics International. 40 (2014) 5201-5207.

[39] J. Deng, M. Cai, W. Sun, X. Liao, W. Chu, X.S. Zhao, Chemsuschem. 6 (2013) 2061-2065.

[40] M. Pechini, in: U.S.P. Office (Ed.), 1969.

[41] L. Gama, M.A. Ribeiro, B.S. Barros, R.H.A. Kiminami, I.T. Weber, A. Costa, Journal of Alloys and Compounds. 483 (2009) 453-455.

[42] R.D. Golpasha, D. Karami, R. Ahmadi, E. Bagherzadeh, Reaction Kinetics and Catalysis Letters. 51 (1993) 393-400.

[43] C.O. Arean, M.P. Mentruit, A.J.L. Lopez, J.B. Parra, Colloids and Surfaces a-Physicochemical and Engineering Aspects. 180 (2001) 253-258.

[44] I. Murthy, C.S. Swamy, Journal of Materials Science. 28 (1993) 1194-1198.

[45] N.F.P. Ribeiro, R.C.R. Neto, S.F. Moya, M.M.V.M. Souza, M. Schmal, Int. J. Hydrog. Energy. 35 (2010) 11725-11732.

[46] Y. Nishihata, J. Mizuki, T. Akao, H. Tanaka, M. Uenishi, M. Kimura, T. Okamoto, N. Hamada, Nature. 418 (2002) 164-167.

[47] M. Kakihana, M. Yoshimura, Bulletin of the Chemical Society of Japan. 72 (1999) 1427-1443.

[48] N. Salhi, C. Petit, A. Kiennemann, in: A. Gedeon, P. Massiani, F. Babonneau (Eds.), Zeolites and Related Materials: Trends, Targets and Challenges, Proceedings of the 4th International Feza Conference, 2008, pp. 1335-1338.

[49] B.C. Enger, R. Lodeng, J. Walmsley, A. Holmen, Appl. Catal. A: Gen. 383 (2010) 119-127.

[50] S.S. Pansare, J.D. Allison, Appl. Catal. A: Gen. 387 (2010) 224-230.

[51] I. Chorkendorff, J. Niemantsverdriet, Concepts of Modern Catalysis and Kinetics, 2 ed., Wiely-VCH, 2011.

[52] T. Ataloglou, J. Vakros, K. Bourikas, C. Fountzoula, C. Kordulis, A. Lycourghiotis, Appl. Catal. B: Environ. 57 (2005) 299-312.

[53] L. Vordonis, N. Spanos, P.G. Koutsoukos, A. Lycourghiotis, Langmuir. 8 (1992) 1736-1743.

[54] N. Spanos, A. Lycourghiotis, J. Chem. Soc. Faraday Trans. 89 (1993) 4101-4107.

[55] J. Vakros, K. Bourikas, S. Perlepes, C. Kordulis, A. Lycourghiotis, Langmuir. 20 (2004) 10542-10550.

[56] K. Bourikas, C. Kordulis, J. Vakros, A. Lycourghiotis, Adv. Colloid Interface Sci. 110 (2004) 97-120.

[57] T. Ataloglou, K. Bourikas, J. Vakros, C. Kordulis, A. Lycourghiotis, J. Phys. Chem. B. 109 (2005) 4599-4607.

[58] K. Bourikas, C. Kordulis, A. Lycourghiotis, Catal. Rev.: Sci. Eng. 48 (2006) 363-444.

[59] K. Bourikas, J. Vakros, C. Fountzoula, C. Kordulis, A. Lycourghiotis, Catal. Today. 128 (2007) 138-144.

[60] X. Hao, W.A. Spieker, J.R. Regalbuto, J. Colloid Interface Sci. 267 (2003) 259-264.

[61] D.W. Fuerstenau, K. Osseoasare, J. Colloid Interface Sci. 118 (1987) 524-542.

[62] P.H. Tewari, W. Lee, J. Colloid Interface Sci. 52 (1975) 77-88.

[63] R.O. James, T.W. Healy, J. Colloid Interface Sci. 40 (1972) 65-81.

[64] P.K. Debokx, W.B.A. Wassenberg, J.W. Geus, J. Catal. 104 (1987) 86-98.

[65] A. Haworth, Adv. Colloid Interface Sci. 32 (1990) 43-78.

[66] C.H. Bartholomew, R.J. Farrauto, J. Catal. 45 (1976) 41-53.

[67] K.B. Agashe, J.R. Regalbuto, J. Colloid Interface Sci. 185 (1997) 174-189.

[68] J.A. Schwarz, Contescu, C., Surfaces of Nanoparticles And Porous Materials, Ipswich, MA, 1999.

[69] W.G. Schlaffer, C.Z. Morgan, J.N. Wilson, J. Phys. Chem. 61 (1957) 714-722.

[70] Holleman-Wiberg, Inorganic Chemistry, Academic Press, 2001.

[71] W. Stumm, H. Hohl, F. Dalang, Croat. Chem. Acta. 48 (1976) 491-504.

[72] E. Ruckenstein, H.Y. Wang, J. Catal. 205 (2002) 289-293.

[73] S.A. Hosseini, A. Taeb, F. Feyzi, Catal. Commun. 6 (2005) 233-240.

[74] J.G. Zhang, H. Wang, A.K. Dalai, J. Catal. 249 (2007) 300-310.

[75] B. Jongsomjit, J. Panpranot, J.G. Goodwin, J. Catal. 204 (2001) 98-109.

[76] N. Job, S. Lambert, M. Chatenet, C.J. Gommes, F. Maillard, S. Berthon-Fabry, J.R. Regalbuto, J.-P. Pirard, Catal. Today. 150 (2010) 119-127.

[77] B. Scheffer, P. Molhoek, J.A. Moulijn, Appl. Catal. 46 (1989) 11-30.

[78] J.M. Rynkowski, T. Paryjczak, M. Lenik, Appl. Catal. A: Gen. 106 (1993) 73-82.

[79] Y.-W.C. Hsin-Yu Lin, Mater. Chem. Phys. (2003) 171-175.

[80] R. Bechara, D. Balloy, J.Y. Dauphin, J. Grimblot, Chem. Mater. 11 (1999) 1703-1711.

[81] L. Guczi, T. Hoffer, Z. Zsoldos, S. Zyade, G. Maire, F. Garin, J. Phys. Chem. 95 (1991) 802-808.

[82] Z. Zsoldos, L. Guczi, J. Phys. Chem. 96 (1992) 9393-9400.

[83] W.J. Wang, Y.W. Chen, Appl. Catal. 77 (1991) 223-233.

[84] P. Arnoldy, J.A. Moulijn, J. Catal. 93 (1985) 38-54.

[85] J.Y. Yan, M.C. Kung, W.M.H. Sachtler, H.H. Kung, J. Catal. 172 (1997) 178-186.

[86] Y.J. Lee, J.Y. Park, K.W. Jun, J.W. Bae, P.S.S. Prasad, Catal. Lett. 130 (2009) 198-203.

[87] P.H. Bolt, F. Habraken, J.W. Geus, J. Solid State Chem. 135 (1998) 59-69.

[88] R. Bouarab, O. Cherifi, A. Auroux, Green Chem. 5 (2003) 209-212.

[89] D.S. Jose-Alonso, M.J. Illan-Gomez, M.C. Roman-Martinez, Int. J. Hydrog. Energy. 38 (2013) 2230-2239.

[90] P. Ferreira-Aparicio, A. Guerrero-Ruiz, I. Rodriguez-Ramos, Appl. Catal. A: Gen. 170 (1998) 177-187.

[91] K. Takanabe, K. Nagaoka, K. Nariai, K. Aika, J. Catal. 230 (2005) 75-85.

[92] J. van de Loosdrecht, B. Bazhinimaev, J.A. Dalmon, J.W. Niemantsverdriet, S.V. Tsybulya, A.M. Saib, P.J. van Berge, J.L. Visagie, Catal. Today. 123 (2007) 293-302.

[93] O.S. Joo, K.D. Jung, Bull. Korean Chem. Soc. 23 (2002) 1149-1153.

[94] J.R. Rostrup-Nielsen, J. Catal. 27 (1972) 343-356.

[95] N. Sahli, C. Petit, A.C. Roger, A. Kiennemann, S. Libs, M.M. Bettahar, Catal. Today. 113 (2006) 187-193.

[96] R.T.K. Baker, Carbon. 27 (1989) 315-323.

[97] R.T.K. Baker, P.S. Harris, R.B. Thomas, R.J. Waite, J. Catal. 30 (1973) 86-95.

[98] J.R. Rostrup-Nielsen, J. Catal. 85 (1984) 31-43.

[99] J.W. Long, M. Laskoski, G.W. Peterson, T.M. Keller, K.A. Pettigrew, B.J. Schindler, J. Mater. Chem. 21 (2011) 3477-3484.

[100] J. Nakamura, I. Toyoshima, K. Tanaka, Surf. Sci. 201 (1988) 185-194.

[101] Y.J. Huang, J.A. Schwarz, Appl. Catal. 30 (1987) 239-253.

[102] J.M. Rynkowski, T. Paryjczak, M. Lenik, Appl. Catal. A: Gen. 126 (1995) 257-271.

[103] Y.J. Huang, J.A. Schwarz, J.R. Diehl, J.P. Baltrus, Appl. Catal. 36 (1988) 163-175.

[104] Q. Zhong, F.S. Ohuchi, J. Vac. Sci. & Tech a - Vac. Surf. Film. 8 (1990) 2107-2112.

[105] R. Lamber, G. Schulzekloff, Surf. Sci. 258 (1991) 107-118.

[106] J. Hu, J.A. Schwarz, Y.J. Huang, Appl. Catal. 51 (1989) 223-233.

[107] K.V.R. Chary, P.V.R. Rao, V.V. Rao, Catal. Commun. 9 (2008) 886-893.

[108] C.P. Li, Y.W. Chen, Thermochimica Acta. 256 (1995) 457-465.

[109] P. Salagre, J.L.G. Fierro, F. Medina, J.E. Sueiras, J. Mol. Catal. A: Chem. 106 (1996) 125-134.

[110] B.W. Hoffer, A.D. van Langeveld, J.P. Janssens, R.L.C. Bonne, C.M. Lok, J.A. Moulijn, J. Catal. 192 (2000) 432-440.

[111] J. Zielinski, J. Catal. 76 (1982) 157-163.

[112] Y.J. Huang, J.A. Schwarz, Appl. Catal. 36 (1988) 177-188.

[113] Y.J. Huang, J.A. Schwarz, J.R. Diehl, J.P. Baltrus, Appl. Catal. 37 (1988) 229-245.

[114] M. Lojacono, Schiavel.M, A. Cimino, J. Phys. Chem. 75 (1971) 1044-&.

[115] L.F. Zhang, J.F. Lin, C. Yi, J. Chem. Soc. Faraday Trans. 88 (1992) 497-502.

[116] A. Gil, A. Diaz, L.M. Gandia, M. Montes, Appl. Catal. A: Gen. 109 (1994) 167-179.

[117] R. Lamber, G. Schulzekloff, J. Catal. 146 (1994) 601-607.

[118] R.R. John, Catalyst Preparation, CRC Press, 2006, pp. 297-318.

[119] K.S.W. Sing, D.H. Everett, R.A.W. Haul, L. Moscou, R.A. Pierotti, J. Rouquerol, T. Siemieniewska, Pure Appl. Chem. 57 (1985) 603-619.

[120] J.L. Ewbank, L. Kovarik, C.C. Kenvin, C. Sievers, Green Chem. 16 (2014) 885-896.

[121] M. Santiago, J. Perez-Ramirez, Environmental Science & Technology. 41 (2007) 1704-1709.

[122] A.J. van Dillen, R. Terorde, D.J. Lensveld, J.W. Geus, K.P. de Jong, J. Catal. 216 (2003) 257-264.

[123] S.L. Chen, H.L. Zhang, J. Hu, C. Contescu, J.A. Schwarz, Appl. Catal. 73 (1991) 289-312.

[124] M.A.A. Elmasry, A. Gaber, E.M.H. Khater, J. Therm. Thermal Analysis and Calorim. 52 (1998) 489-495.

[125] M.K. Nikoo, N.A.S. Amin, Fuel Process. Technol. 92 (2011) 678-691.

[126] J.G. Seo, M.H. Youn, J.C. Jung, I.K. Song, Int. J. Hydrog. Energy. 34 (2009) 5409-5416.

[127] X. Krokidis, P. Raybaud, A.E. Gobichon, B. Rebours, P. Euzen, H. Toulhoat, J. Phys. Chem. B. 105 (2001) 5121-5130.

[128] W.L. Chu, W.S. Yang, L.W. Lin, Appl. Catal. A: Gen. 235 (2002) 39-45.

[129] P. Burtin, J.P. Brunelle, M. Pijolat, M. Soustelle, Appl. Catal. 34 (1987) 225-238.

[130] J.J. Guo, H. Lou, H. Zhao, D.F. Chai, X.M. Zheng, Appl. Catal. A: Gen. 273 (2004) 75-82.

[131] S.B. Wang, G.Q. Lu, Appl. Catal. A: Gen. 169 (1998) 271-280.

[132] A. Alubaid, E.E. Wolf, Appl. Catal. 40 (1988) 73-85.

[133] J.R.H. Ross, M.C.F. Steel, A. Zeiniisfahani, J. Catal. 52 (1978) 280-290.

[134] Muirhead.Js, K.J. Laidler, Transactions of the Faraday Society. 63 (1967) 944-&.

[135] A. Bhattacharyya, V.W. Chang, CO2 REFORMING OF METHANE TO SYNGAS - DEACTIVATION BEHAVIOR OF NICKEL ALUMINATE SPINEL CATALYSTS, 1994.

[136] Z.L. Xu, M. Zhen, Y.L. Bi, K.J. Zhen, Appl. Catal. A: Gen. 198 (2000) 267-273.

[137] D. Li, M. Koike, L. Wang, Y. Nakagawa, Y. Xu, K. Tomishige, Chemsuschem. 7 (2014) 510-522.

[138] M.E. Rivas, J.L.G. Fierro, R. Guil-Lopez, M.A. Pena, V. La Parola, M.R. Goldwasser, Catal. Today. 133 (2008) 367-373.

[139] M. Machida, K. Eguchi, H. Arai, J. Catal. 120 (1989) 377-386.

[140] K. Zhang, G.D. Zhou, J. Li, T.X. Cheng, Catal. Commun. 10 (2009) 1816-1820.

[141] A.R. Gonzalez, Y.J.O. Asencios, E.M. Assaf, J.M. Assaf, Applied Surface Science. 280 (2013) 876-887.

[142] H. Kizaki, K. Kusakabe, S. Nogami, H. Katayama-Yoshida, Applied Physics Express. 1 (2008).

[143] Z. Skoufa, G. Xantri, E. Heracleous, A.A. Lemonidou, Appl. Catal. A: Gen. 471 (2014) 107-117.

[144] T.H. Gardner, D. Shekhawat, D.A. Berry, M.W. Smith, M. Salazar, E.L. Kugler, Appl. Catal. A: Gen. 323 (2007) 1-8.

[145] R. Collongues, D. Gourier, A. Kahnharari, A.M. Lejus, J. Thery, D. Vivien, Annual Review of Materials Science. 20 (1990) 51-82.

[146] T.H. Gardner, J.J. Spivey, E.L. Kugler, A. Campos, J.C. Hissam, A.D. Roy, Journal of Physical Chemistry C. 114 (2010) 7888-7894.

[147] L.G. Tejuca, J.L.G. Fierro, Properties and applications of perovskite-type oxides / edited by L.G. Tejuca, J.L.G. Fierro, New York : Marcel Dekker, 1993., 1993.

[148] Y.S. Han, J.B. Li, X.S. Ning, B. Chi, Journal of the American Ceramic Society. 87 (2004) 1347-1349.

[149] Y.S. Han, J.B. Li, X.S. Ning, X.Z. Yang, B. Chi, Materials Science and Engineering a-Structural Materials Properties Microstructure and Processing. 369 (2004) 241-244.

[150] Z.J. Zhang, Z.L. Wang, B.C. Chakoumakos, J.S. Yin, Journal of the American Chemical Society. 120 (1998) 1800-1804.

[151] I. Hamada, A. Uozumi, Y. Morikawa, A. Yanase, H. Katayama-Yoshida, Journal of the American Chemical Society. 133 (2011) 18506-18509.

[152] M.B. Katz, S. Zhang, Y. Duan, H. Wang, M. Fang, K. Zhang, B. Li, G.W. Graham, X. Pan, J. Catal. 293 (2012) 145-148.

[153] P. Jeevanandam, Y. Koltypin, A. Gedanken, Nano Letters. 1 (2001) 263-266.

[154] H.T. Cui, M. Zayat, D. Levy, Journal of Sol-Gel Science and Technology. 35 (2005) 175-181.

[155] C. Stampfl, Catal. Today. 105 (2005) 17-35.

[156] Y. Ding, Y. Liu, S. Niu, W. Wu, Z.L. Wang, Journal of Applied Physics. 116 (2014) -.

[157] I.E. Achouri, N. Abatzoglou, C. Fauteux-Lefebvre, N. Braidy, Catal. Today. 207 (2013) 13-20.

[158] D. Briggs, E. Heyden, S. London, Hanbook of X-ray and Ultraviolet Photoelctron Spectroscopy, 1977.

[159] J.T. Miller, A.J. Kropf, Y. Zha, J.R. Regalbuto, L. Delannoy, C. Louis, E. Bus, J.A. van Bokhoven, J. Catal. 240 (2006) 222-234.

[160] X.-m. Liu, W.-L. Gao, Materials and Manufacturing Processes. 27 (2012) 905-909.

[161] E.A.V. Ferri, I. Santos, E. Radovanovic, R. Bonzanini, E.M. Girotto, Journal of the Brazilian Chemical Society. 19 (2008) 1153-1157.

[162] J. Xu, G.F. Froment, AIChE Journal. 35 (1989) 88-96.

[163] E. Heracleous, A.F. Lee, K. Wilson, A.A. Lemonidou, J. Catal. 231 (2005) 159-171.

VITA

JESSICA L. EWBANK

Jessica was born in Tampa, Florida. While living in Tampa, she received a G.E.D. in October 2003, an A.A. in Pre-Engineering from the Hillsborough Community College in 2008, and a B.S. in Chemical Engineering from University of South Florida in 2010. Jessica moved to Atlanta, Georgia to attend Georgia Tech in 2010 to pursue an M.S. and Ph.D. in Chemical Engineering. When not conducting research, Jessica enjoys exercising, traveling, horseback riding, outdoor activities, and spending time with her husband, dog, and friends.